

WETLAND SPECTRO-TEMPORAL UNMIXING USING MULTITEMPORAL  
MULTISPECTRAL SATELLITE IMAGES

A THESIS SUBMITTED TO  
THE GRADUATE SCHOOL OF NATURAL AND APPLIED SCIENCES  
OF  
MIDDLE EAST TECHNICAL UNIVERSITY

BY  
ERDEM ÖZER

IN PARTIAL FULFILLMENT OF THE REQUIREMENTS  
FOR  
THE DEGREE OF DOCTOR OF PHILOSOPHY  
IN  
GEODETIC AND GEOGRAPHIC INFORMATION TECHNOLOGIES

FEBRUARY 2022



Approval of the thesis:

**WETLAND SPECTRO-TEMPORAL UNMIXING USING  
MULTITEMPORAL MULTISPECTRAL SATELLITE IMAGES**

submitted by **ERDEM ÖZER** in partial fulfillment of the requirements for the degree of **Doctor of Philosophy in Geodetic and Geographic Information Technologies, Middle East Technical University** by,

Prof. Dr. Halil Kalıpçılar  
Dean, Graduate School of **Natural and Applied Sciences** \_\_\_\_\_

Prof. Dr. Zuhâl Akyürek  
Head of the Department, **Geodetic and Geographic Information Technologies, METU** \_\_\_\_\_

Assoc. Prof. Dr. Uğur Murat Lelođlu  
Supervisor, **Geodetic and Geographic Information Technologies, METU** \_\_\_\_\_

**Examining Committee Members:**

Prof. Dr. Mehmet Lütfi Süzen  
Geological Engineering, METU \_\_\_\_\_

Assoc. Prof. Dr. Uğur Murat Lelođlu  
Geodetic and Geographic Information Technologies, METU \_\_\_\_\_

Prof. Dr. Ali Özgün Ok  
Geomatics Engineering, Hacettepe University \_\_\_\_\_

Assoc. Prof. Dr. Uğur Avdan  
Geodetic and Geographic Information Technologies, Eskişehir Technical University \_\_\_\_\_

Assoc. Prof. Dr. Gordana Kaplan  
Geodetic and Geographic Information Technologies, Eskişehir Technical University \_\_\_\_\_

Date: 03.02.2022

**I hereby declare that all information in this document has been obtained and presented in accordance with academic rules and ethical conduct. I also declare that, as required by these rules and conduct, I have fully cited and referenced all material and results that are not original to this work.**

Name Last name : Erdem Özer

Signature :

## **ABSTRACT**

### **WETLAND SPECTRO-TEMPORAL UNMIXING USING MULTITEMPORAL MULTISPECTRAL SATELLITE IMAGES**

Özer, Erdem

Doctor of Philosophy, Geodetic and Geographic Information Technologies

Supervisor: Assoc. Prof. Dr. Uğur Murat Leloğlu

February 2022, 157 pages

Wetlands constitute one of the wealthiest and most productive ecosystems on earth. These areas are sophisticated aquatic habitats serving not only the locals but also the whole Earth system on a broad range. Following tropical forests, they have the highest biological diversity. These ecosystems are viable nourishment, reproduction, and sheltering environments for a whole range of living beings and are therefore accepted as natural wealth museums of the world. Monitoring such valuable areas and obtaining crucial information from them, in this regard, has been the primary motivation of the studies performed during the preparation of this thesis. When the sizes, geographic distribution, and total coverage of wetlands across the earth are taken into account, remote sensing shines out as the most economically and technically feasible method to realize the goals related to the mentioned motivation. Concerning the utilization of medium resolution satellite images as the input, the pixel-level approach falls short of understanding the wetland dynamics since vast amounts of pixels in such areas have mixed content.

In this study, the soft classification of wetlands is aimed in order to determine all ground characteristics and their exact proportions. The path to achieving this goal passes through conducting an investigation within correct boundaries. Hence,

detection of the wetland extent prior to sub-pixel analysis is addressed as a critical pre-processing step for realizing the subject motivation. The extent determination part includes calculating Tasseled Cap Water Index (TCWI) values on time series and modeling variations throughout the year by fitting a double-sided sigmoid function. This information is coupled with Digital Terrain Model (DTM) thresholding to extract the final extent. The sub-pixel analysis covers adopting a systematic approach using a three-element (soil, vegetation, water) scheme for establishing wetland ontology and implementing supervised spectral unmixing enhanced by the band and endmember optimizations. Balıkdamı, one of the most impressive wetlands of Turkey, is chosen as the test area. Open access optical satellite data, acquired by Sentinel-2 Multispectral Instrument (MSI), are utilized as the primary input. Since the abundance values of land cover classes in each Sentinel-2 pixel are estimated, reference abundance data with a 10 m grid interval are generated using four-band aerial images having a 30 cm ground sampling distance (GSD) for the verification stage. A new metric entitled "Abundance Confusion Matrix (ACOMA)" is introduced for the comparison and detailed assessment of reference and estimated fractional land cover.

Experimental results demonstrate that the extent determination is addressed with a sensitivity of 93.55% and a precision of 99.21%. Moreover, abundance values of land cover classes are determined with overall accuracies of 66.17% and 66.27% for the monotemporal and multitemporal cases, respectively. In addition to a 2% overall accuracy increase compared to the hard classification, the detectability of sparse land cover classes is demonstrated that are vanished while using pixel-based approaches. Furthermore, gradients are able to be observed, particularly at watersides. As a result, the proposed method proves to be a valuable tool for the detailed monitoring of wetlands.

Keywords: Wetlands, Spectral Unmixing, Sentinel-2, Abundance Confusion Matrix, Fractional Land Cover

## ÖZ

### ÇOK ZAMANLI ÇOK BANTLI UYDU GÖRÜNTÜLERİ KULLANILARAK SULAK ALANDA SPEKTRO-ZAMANSAL AYRIŞTIRMA

Özer, Erdem  
Doktora, Jeodezi ve Coğrafi Bilgi Teknolojileri  
Tez Yöneticisi: Doç. Dr. Uğur Murat Leloğlu

Şubat 2022, 157 sayfa

Sulak alanlar, yeryüzünün en zengin ve üretken ekosistemleri arasında yer alırlar. Bu alanlar, sadece yöre halkına değil yeryüzü sistemine de geniş yelpazede hizmet eden sofistike sucul habitatlardır. Tropikal ormanların ardından en yüksek biyolojik çeşitliliğe sahiptirler. Bu ekosistemler, birçok canlı için uygun beslenme, üreme ve barınma olanağı sağlar ve bu nedenle dünyanın doğal zenginlik müzeleri olarak kabul edilirler. Böylesi değerli alanların izlenmesi ve bu alanlara ait önemli bilgilerin çıkarılması, bu tezin hazırlanmasında gerçekleştirilen çalışmaların ana motivasyon kaynağı olmuştur. Sulak alanların büyüklükleri, coğrafi dağılımları ve dünya genelindeki toplam kapsamları dikkate alındığında, uzaktan algılama, bahsedilen motivasyona ilişkin amaçların gerçekleştirilmesinde ekonomik ve teknik anlamda en makul yöntem olarak öne çıkmaktadır. Orta çözünürlüklü uydu görüntülerinin kullanımına ilişkin olarak, piksel tabanlı sınıflama, sulak alana ait birçok pikselin karışık içerikli olması nedeniyle, sulak alan dinamiklerini anlama hususunda yetersiz kalmaktadır.

Bu çalışmada, tüm zemin karakteristiklerini ve bunların oranlarını tam olarak belirlemek için sulak alanların yumuşak sınıflandırılması amaçlanmıştır. Bu amaca

ulaşmanın yolu ise, doğru sınırlar içinde bir araştırma yapmaktan geçmektedir. Bu nedenle, alt piksel analizinden önce sulak alan kapsamının tespiti, söz konusu motivasyonunun gerçekleştirilebilmesi için kritik bir ön işleme adımı olarak ele alınmıştır. Kapsam belirleme kısmı için zaman serilerinde, Püsküllü Kep Su İndeksi değerleri hesaplanmış ve yıllık değişimler çift taraflı sigmoid fonksiyonu kullanılarak modellenmiştir. Elde edilen bilgiler Sayısal Arazi Modeli eşikleme ile birleştirilerek nihai kapsam elde edilmiştir. Alt piksel analizi, sulak alan ontolojisinin oluşturulması için üç unsurlu (toprak, bitki, su) şema kullanımına dayanan sistematik bir yaklaşımın benimsenmesi ile bant ve son üye optimizasyonları aracılığıyla iyileştirilen kontrollü spektral ayırma işleminin gerçekleştirilmesini içermektedir. Test alanı olarak Türkiye'nin en etkileyici sulak alanlarından birisi olan Balıkdamı seçilmiştir. Temel veri girdisi olarak açık erişim sağlanabilen Sentinel-2 çok bantlı optik uydu görüntüleri kullanılmıştır. Her bir Sentinel-2 pikselindeki arazi örtüsü sınıflarının bolluk değerleri tahmin edildiğinden, doğrulama aşaması için 30 cm yer örnekleme aralığına sahip dört bantlı hava görüntüleri kullanılarak, 10 m grid aralığında referans bolluk verisi üretilmiştir. Referans ve kestirilmiş üleşke arazi örtüsünün karşılaştırılması ve detaylı şekilde değerlendirilmesi için "Bolluk Karışıklık Matrisi" isimli yeni bir metrik önerilmiştir.

Deneysel sonuçlar, kapsam belirlemenin %93,55 duyarlılık ve %99,21 hassasiyet ile elde edildiğini göstermektedir. Ayrıca arazi örtüsü sınıflarının bolluk değerleri, tek zamanlı ve çok zamanlı durumlar için sırasıyla %66,17 ve %66,27 genel doğrulukla belirlenmiştir. Sert sınıflandırmaya kıyasla %2'lik bir genel doğruluk artışına ek olarak, piksel tabanlı yaklaşımlar kullanılırken kaybolan seyrek arazi örtüsü sınıflarının tespit edilebildiği kanıtlanmıştır. Ayrıca, özellikle su kenarlarındaki gradyanların gözlemlenebildiği gösterilmiştir. Sonuç olarak, önerilen yöntemin sulak alanların detaylı izlenmesi için değerli bir araç olduğu ortaya konmuştur.

Anahtar Kelimeler: Sulak Alanlar, Sentinel-2, Ayırıştırma, Bolluk Karışıklık Matrisi, Üleşke Arazi Örtüsü



To my late bosom friend “The Hodja” İskender Tekin

OMNES VULNERANT, ULTIMA NECAT...

## ACKNOWLEDGMENTS

First and foremost, I would like to take this opportunity to express my deepest gratitude to my supervisor, Assoc. Prof. Dr. Uğur Murat Leloğlu, for his guidance, contributions, support, and encouragement throughout my studies. He literally assisted me in all aspects of my research, including site visits, coding, writing, and proofreading. He motivated me whenever I got stuck and desperate. He made me realize that the issues that seem to be very complicated are not necessarily that complicated. I will always be grateful for all. Apart from these, I have to highlight my musical intellectual gains thanks to him during our out-of-town road trips over three successive years.

I would like to thank my thesis monitoring committee and defense examination jury members, Prof. Dr. Mehmet Lütfi Süzen and Prof. Dr. Ali Özgün Ok, for their valuable comments and suggestions from the very beginning to the final submission. I have to thank Prof. Dr. Ali Özgün Ok for redacting my thesis as well. Their contributions are greatly appreciated.

I would like to express my sincere gratitude to Assoc. Prof. Dr. Uğur Avdan and Assoc. Prof. Dr. Gordana Kaplan, for taking time out of their busy schedules and being my defense examination jury members. Their criticism enriched my thesis and made it more comprehensible.

I would like to thank Prof. Dr. Mahmut Onur Karşlıoğlu for his guidance and sincerity. I am genuinely grateful for his constant support throughout my doctoral studies. I have learned a lot from him, and I wish him all the very best in his life abroad.

I would like to express my sincere gratitude to Assoc. Prof. Dr. Kamil Teke for his clarifications, support, and friendship. He always made time for me, even in his busiest periods. Our discussions gave me new insights and helped me reinforce my knowledge.

I am deeply indebted to Dr. Naim Cem Güllüoğlu for his mentorship and friendship. He is a fantastic person and a great consultant about everything. He responded to all my inquiries straight away perfectly. I am so lucky to get to know him and work next to him.

I would like to express my sincere gratitude to Ahmet Rasim Kabukcuoğlu for his ultra-detailed proofreading, constructive suggestions, and friendship. His contributions made my manuscript clearer and notably error-free.

I would like to thank Ayhan Kavşut and Dr. Akın Kısa for their support, understanding, and help with auxiliary data collection. They continuously encouraged me not to get hung up on details and to finish off my research.

I would like to express my sincere gratitude to my ex-workmates Hülya Tuna, Ekrem Ayyıldız, Vejdi Subari, and Adil Araz for their continuous support and friendship. I am truly delighted to know them.

I would like to send special thanks to the General Directorate of Mapping for providing the ground truth of this research and to online Q&A communities, Stack Exchange, STEP Forum, MATLAB Answers, Esri Community, and GitHub for helping me find elegant solutions to my problems within a short amount of time.

I would like to express my sincere gratitude to Dr. Tunca Kaya for his lifelong friendship. He is a very loyal and solid friend. I am much obliged to him for standing by me and always supporting me to get through the hard times.

I would like to thank Buket Gülşen for her moral support, encouragement, and appeasement efforts towards additional obstacles. She introduced me to new concepts such as the law of secret, self-affirmation, and meditative processes. Although the impacts on me are debatable, she managed to maintain her faith after all. She is a wonderful person, and I am genuinely grateful to her.

Special thanks go to Aşil and Müjgan, who brought joy and hope to my life. They always showed up at unexpected moments during my long working nights and did not leave me alone. They are simply amazing.

I would like to express my sincere gratitude to my parents, Neyire Özer and Ahmet Sencer Özer, for their love and encouragement throughout my life. I have to thank my sister-in-law Tuğba Özer, my niece Nehir Özer, and my nephew Çağan Özer for joining the family and bringing huge happiness.

I would like to take this opportunity to offer special thanks to my big brother, Mehmet Nadir Özer. Besides being one of the most intelligent people, I have ever known, he is a real role model and a great person with a big heart. I know that he is always there for me just because he loves me endlessly and unconditionally. I do not have to be a successful, wealthy, or eminent person. He accepts me the way I am and always backs me up on every occasion. I consider myself exceptionally lucky to have him in my life.

Lastly, I would like to express my sincere gratitude to my late bosom friend and guide, İskender Tekin, for everything he had done for me. I experienced priceless moments with him and learned many things both professionally and intellectually. I will always remember him with respect and love. Rest in peace, master...

## TABLE OF CONTENTS

ABSTRACT .....	v
ÖZ.....	vii
ACKNOWLEDGMENTS .....	xi
TABLE OF CONTENTS .....	xiv
LIST OF TABLES .....	xvii
LIST OF FIGURES.....	xviii
LIST OF ABBREVIATIONS .....	xxiii
LIST OF SYMBOLS.....	xxvi
1 INTRODUCTION.....	1
1.1 Problem Definition .....	1
1.2 Research Objectives.....	8
1.3 Overview of Proposed Approach.....	9
1.4 Contributions of Thesis.....	11
1.5 Outline of Thesis.....	12
2 LITERATURE REVIEW .....	15
2.1 Wetland Detection .....	15
2.2 Temporal Dynamics of Wetlands .....	16
2.3 Wetland Parameters .....	16
2.4 Wetland Classification.....	17
2.5 Bathymetry.....	18
2.6 Data Fusion .....	19
3 STUDY AREA AND DATA USED.....	21

3.1	Study Area.....	21
3.2	Data Used .....	28
3.2.1	Ground Truth .....	29
3.2.2	Fieldwork .....	31
3.2.3	Test Data .....	33
4	METHODOLOGY .....	37
4.1	Downloading and Pre-processing of Sentinel-2 Satellite Imagery .....	38
4.2	Co-registration of Satellite Imagery .....	40
4.3	Determination of Wetland Extent.....	41
4.4	Classification Ontology.....	45
4.5	Spectral Library Generation from Pure Pixels .....	50
4.6	Generation of Ground Truth for Abundances .....	51
4.7	Spectral Unmixing of Multispectral Images .....	54
4.8	Performance Assessment.....	60
4.9	Visualization of Gathered and Generated Data.....	69
5	RESULTS AND DISCUSSION .....	71
5.1	Results .....	71
5.1.1	Co-registration of Satellite Imagery.....	71
5.1.2	Wetland Mask .....	73
5.1.3	Spectral Signatures of Classes .....	80
5.1.4	Classification of Reference Orthophoto.....	81
5.1.5	Soft Classification of Sentinel-2 L2A Data .....	83
5.1.5.1	Spectral Unmixing .....	83
5.1.5.2	Spectro-Temporal Unmixing .....	91

5.1.6	Data Visualization .....	95
5.2	Discussion.....	96
6	CONCLUSIONS AND RECOMMENDATIONS.....	111
6.1	Conclusions.....	111
6.2	Recommendations.....	114
	REFERENCES .....	119
	APPENDICES .....	135
A.	Site Visit Observations .....	135
B.	Analysis Results for Samples Taken from Balıkdamı Wetland .....	152
C.	Stream Gauge Observations for 2015 Water Year .....	155
	CURRICULUM VITAE .....	157



## LIST OF TABLES

### TABLES

Table 1.1	Ramsar Sites in Turkey .....	5
Table 3.1	Wetlands in Turkey .....	21
Table 3.2	Dominant vegetation families in Balıkdamı.....	24
Table 3.3	Balıkdamı bird species on red list .....	26
Table 3.4	Details of data used .....	28
Table 3.5	Spectral bands for Sentinel-2 sensors.....	34
Table 4.1	Three-element ontology .....	47
Table 4.2	Performance metrics for evaluating wetland extent determination.....	60
Table 5.1	Correlation of coefficient values for each algorithm.....	71
Table 5.2	Standard deviations of fitting results.....	77
Table 5.3	Extent determination metric results for double-sigmoid fitting ...	79
Table 5.4	Acquisition dates of Sentinel-2 July imagery.....	84
Table 5.5	Optimized band weights .....	84
Table 5.6	Comparison of spectral unmixing accuracy metrics for unoptimized and optimized band weight cases .....	85
Table 5.7	Comparison of spectral unmixing accuracy metrics for different configurations .....	92
Table 5.8	Delta matrix between monotemporal and multitemporal ACOMA .....	95
Table B.1	Evaluation of soil sample-1 .....	152
Table B.2	Evaluation of soil sample-2.....	153
Table B.3	Evaluation of soil sample-3 .....	154

## LIST OF FIGURES

### FIGURES

Figure 1.1	Benefits of wetlands.....	3
Figure 1.2	Global distribution of Ramsar Sites .....	4
Figure 1.3	Geolocation of Ramsar Sites in Turkey .....	5
Figure 1.4	Wetland Extent Index for period between 1970 and 2010.....	6
Figure 1.5	Earth observation from space.....	8
Figure 1.6	Flowchart of research methodology.....	10
Figure 1.7	Outline of thesis .....	13
Figure 3.1	Wetlands in Turkey .....	22
Figure 3.2	Location and topography of Balıkdamı .....	23
Figure 3.3	Footprints of 2019 aerial imagery .....	30
Figure 3.4	Passing through Sakarya River (19.08.2020).....	31
Figure 3.5	Ranunculus sample collection (19.08.2020) .....	32
Figure 3.6	Single image frame exported from UAV video record (19.08.2020).....	32
Figure 3.7	Orbital configuration of Sentinel-2 satellites .....	33
Figure 4.1	Flowchart of Sections 4.1, 4.2, and 4.3.....	37
Figure 4.2	Index time series from 7 years data ③ Averaged NDVI of sample vegetation polygon ⑥ Averaged NDWI of sample soil polygon.	39
Figure 4.3	Dynamic map showing number of days of 2018 for max index values .....	40
Figure 4.4	Curve fitting on each pixel of image stack .....	42
Figure 4.5	Flowchart of Sections 4.4, 4.5, and 4.6.....	45
Figure 4.6	Clustering trials .....	46
Figure 4.7	Illustrations for given classification ontology ① Gypsum ② Juncus ③ Pasture ④ Phragmites ⑤ Ranunculus ⑥ Shallow Water ⑦ Steppe ⑧ Typha ⑨ Water .....	49

Figure 4.8	Spectral library generation from pure pixels ① Training polygon ② Step-1 ③ Step-2 ④ Step-3 ⑤ Step-4 ⑥ Steps-5&6 .....	51
Figure 4.9	Illustrations of outputs after each step ① Orthophoto ② Step-1 ③ Step-2 ④ Step-3 ⑤ Step-4 ⑥ Step-5 ⑦ Steps-6&7 ⑧ Step-8..	53
Figure 4.10	Flowchart of Sections 4.7, 4.8, and 4.9 .....	54
Figure 4.11	Illustrations for mixture models ① Linear Mixture Model ② Bilinear Mixture Model ③ Intimate Mixture Model.....	56
Figure 4.12	Flowchart of band optimization process.....	59
Figure 4.13	Example of original (left) vs. reconstructed (right) RGB images	60
Figure 5.1	Absolute shift values of tie points for image dated 23.03.201972	
Figure 5.2	Comparison of different elevation models - Red polygon represents ground truth extent digitized manually from high resolution orthophoto ① Aerial DTM ② ALOS ③ Copernicus ④ SRTM.....	73
Figure 5.3	Example of fourth-order polynomial fitting on 106-band image stack.....	74
Figure 5.4	Total number of days having TCWI over -0.1 in a calendar year .....	74
Figure 5.5	Locations having TCWI over -0.1 more than 120 days in a calendar year.....	75
Figure 5.6	Example of double-sigmoid curve fitting on 106-band image stack.....	75
Figure 5.7	Total number of days having TCWI over -0.1 in a calendar year .....	76
Figure 5.8	Locations having TCWI over -0.1 more than 120 days in a calendar year.....	76
Figure 5.9	Evolution of wetland mask ① DTM thresholding ② Double- sigmoid fitting on TCWI stack ③ Intersection of a and b ④ Small object removal ⑤ Region/hole filling ⑥ Morphological opening .....	78

Figure 5.10	Manually marked vs. predicted wetland boundaries.....	79
Figure 5.11	Spectral signatures of classes of 2019 mean monthly imagery for period between February and August .....	80
Figure 5.12	Spectrum comparison between mean and individual pixels .....	81
Figure 5.13	Confusion matrix for RF classification of orthophoto .....	82
Figure 5.14	Parameter importance (left) and OOB error (right) .....	82
Figure 5.15	Classified orthophoto .....	83
Figure 5.16	ACOMA for unmixed test data.....	85
Figure 5.17	Abundance distribution for each endmember .....	86
Figure 5.18	Standard deviations for monotemporal unmixing.....	86
Figure 5.19	Scatter plot for randomly selected 10% of reference and unmixed pixels (colorbar shows consistency whereas black line denotes least squares line).....	87
Figure 5.20	Transition route along which plant zonation is observed .....	88
Figure 5.21	Plant zonation along transition route .....	88
Figure 5.22	Confusion matrix for RF classification of Sentinel-2 data .....	89
Figure 5.23	Example of land cover determination ㉑ RGB Orthophoto ㉒ Orthophoto RF classification ㉓ Sentinel-2 RF classification ㉔ Reference abundance data for water class only ㉕ Unmixing result for water class only .....	90
Figure 5.24	Unoptimized (solid) vs. optimized (dashed) endmember spectra for April and July image stack .....	91
Figure 5.25	ACOMA for stacked data .....	92
Figure 5.26	Abundance distribution for each multitemporal endmember .....	93
Figure 5.27	Standard deviations for multitemporal unmixing .....	93
Figure 5.28	Scatter plot for randomly selected 10% of reference and unmixed multitemporal pixels (colorbar shows consistency whereas black line denotes least squares line).....	94
Figure 5.29	Visualization of inputs and outputs via the interactive map .....	96

Figure 5.30	RF classification results for 3-band (Blue/NIR/DSM) composite.....	100
Figure 5.31	Location of Sakarya N. Aktaş stream gauge and region topography.....	104
Figure 5.32	Monthly average flow rate (m <sup>3</sup> /sec) at Sakarya N. Aktaş stream gauge for 2015 water year.....	105
Figure 5.33	Eskişehir City 2019 monthly precipitation totals (mm).....	106
Figure 5.34	Comparison of orthophoto (above) vs. GE image (below).....	107
Figure 5.35	Calculated <i>apm</i> for optimized monotemporal data.....	108
Figure 5.36	Calculated <i>apm</i> for optimized multitemporal data.....	109
Figure 6.1	Vegetation gradient as a function of distance to lake: Typha, Phragmites, Juncus, Pasture, Steppe.....	113
Figure 6.2	Preliminary outcomes of pseudo-bathymetric information extraction.....	116
Figure 6.3	Images showing degradation of Balıkdamı at two-year intervals	118
Figure A.1	Location of the photos taken on 19.12.2019 (date of base map is 03.12.2019).....	135
Figure A.2	① Dry Salicornia on wet Gypsum ② General view of Gypsum area ③ Pasture ④ Juncus.....	136
Figure A.3	⑤ Tuft of Juncus ⑥, ⑦ Flood area ⑧ Submerged plants.....	137
Figure A.4	⑨ Dense Typha ⑩ Trees ⑪ Limestone ⑫ East side of bridge located at easternmost boundary.....	138
Figure A.5	⑬ West side of bridge located at easternmost boundary ⑭ Tufts of Juncus ⑮, ⑯ Burned Typha.....	139
Figure A.6	Location of the photos taken on 19.08.2020 (date of base map is 19.08.2020).....	140
Figure A.7	① Partial Salicornia on Gypsum ② Vegetated Gypsum ③ Juncus ④ North side of wetland.....	141

Figure A.8	⑤ Juncus dominated mixed vegetation ⑥ Adjacent Pasture, Juncus and Phragmites clusters ⑦ Cracked Gypsum ⑧ Distichlis spicata on Gypsum.....	142
Figure A.9	⑨ Cracked Gypsum ⑩, ⑪ Distichlis spicata ⑫ Dry Salicornia on Gypsum.....	143
Figure A.10	⑬ Juncus ⑭ Steppe ⑮ Vegetated Gypsum ⑯ Gauge plate on center bridge pillar .....	144
Figure A.11	⑰ Dense Typha next to river ⑱ Pond inside dense Typha ⑲, ⑳ Pasture to Phragmites and Typha Transition.....	145
Figure A.12	㉑, ㉒, ㉓ Typha and Phragmites dominated mixed vegetation ㉔ Tufts of Juncus .....	146
Figure A.13	㉕ Tufts of Ranunculus on river basin ㉖ Bird watching tower ㉗ Tufts of Ranunculus on river basin ㉘ Tufts of Ranunculus on easternmost boundary .....	147
Figure A.14	Location of the photos taken on 02.09.2021 (date of base map is 08.09.2021) .....	148
Figure A.15	① Salicornia on Gypsum ② Mud beneath Gypsum ③ Juncus and Distichlis spicata border ④ Juncus and Phragmites mixture .....	149
Figure A.16	⑤ Gauge plate on center bridge pillar ⑥ Phragmites and Ranunculus ⑦ Phragmites dominated mixed vegetation ⑧ Pond inside Phragmites and Typha.....	150
Figure A.17	⑨ Steppe ⑩ Pasture ⑪ Pasture and Juncus transition ⑫ Tufts of Ranunculus on easternmost boundary.....	151
Figure C.1	Flow data of Sakarya N. Aktaş Station.....	155

## LIST OF ABBREVIATIONS

### ABBREVIATIONS

ACOMA	Abundance Confusion Matrix
AHSI	Advanced Hyperspectral Imager
ALOS	Advanced Land Observing Satellite
AROSICS	Automated and Robust Open-Source Image Co-Registration Software
BOA	Bottom of Atmosphere
CMA	Color Mixture Analysis
DEM	Digital Elevation Model
DIAS	Copernicus Data and Information Access Services
DoY	Day of Year
DSM	Digital Surface Model
DTM	Digital Terrain Model
ESA	European Space Agency
EU	European Union
FERM	Fuzzy Error Matrix
FSDAF	Flexible Spatio-Temporal Data Fusion
FVC	Fractional Vegetation Cover
GCP	Ground Control Point
GEE	Google Earth Engine
GeFolki	Geoscience Extended Flow Optical Lucas-Kanade Iterative
GeoJSON	Geographic JavaScript Object Notation
GNSS	Global Navigation Satellite System
GSD	Ground Sampling Distance
HSV	Hue-Saturation-Value
HTTPS	Hypertext Transfer Protocol Secure
IDE	Integrated Development Environment

IF	Index of Fuzziness
ISODATA	Iterative Self-Organizing Data Analysis
ISP	Instrument Source Packet
lidar	Light Detection and Ranging
LSMA	Linear Spectral Mixture Analysis
LU/LC	Land Use/Land Cover
MAE	Mean Absolute Error
MATLAB	Matrix Laboratory
MF	Matched Filtering
MLST	Mean Local Solar Time
MNDWI	Modified Normalized Difference Water Index
MODIS	Moderate Resolution Imaging Spectroradiometer
MSE	Mean Squared Error
MSI	Multispectral Instrument
MSSIM	Mean Structural Similarity Index
MTMF	Mixture-Tuned Matched Filtering
NDVI	Normalized Difference Vegetation Index
NDWI	Normalized Difference Water Index
NIR	Near Infrared
OBIA	Object-Based Image Analysis
OLI	Operational Land Imager
OOB	Out-of-Bag
PCA	Principal Component Analysis
PEEW	Potential, Existing, Efficient Wetlands
PSF	Point Spread Function
radar	Radio Detection and Ranging
RANSAC	Random Sample Consensus
RF	Random Forest
RGB	Red-Green-Blue
RMSE	Root Mean Squared Error



RTM	Radiative Transfer Model
SAGA	System for Automated Geoscientific Analyses
SAM	Spectral Angle Mapper
SAR	Synthetic Aperture Radar
SBD	Satellite-Derived Bathymetry
SCAASFER	Soft Classification Accuracy Assessment using SCM, FERM, Entropy, and RMSE
SCM	Sub-Pixel Confusion Uncertainty Matrix
SDA	Stepwise Discriminant Analysis
SEM	Structural Equation Modelling
SNAP	Sentinel Application Platform
SRTM	Shuttle Radar Topography Mission
SSE	Sum of Squared Errors
SSIM	Structural Similarity Index Measure
STAFFN	Spatio-Temporal Adaptive Fusion Model for NDVI
STEP	Science Toolbox Exploitation Platform
SVD	Singular Value Decomposition
SVM	Support Vector Machine
SWIR	Short Wave Infrared
TCWI	Tasseled Cap Wetness Index
TIRS	Thermal Infrared Sensor
TOA	Top of Atmosphere
TWI	Transformed Wetness Index
UAV	Unmanned Aerial Vehicle
UIQI	Universal Image Quality Index
WASI	Water Color Simulator
WMS	Web Map Service

## LIST OF SYMBOLS

### SYMBOLS

$y$	Observations
$e$	Observational residuals
$X$	Coefficient matrix
$\beta$	Parameters
$D()$	Covariance matrix
$\sigma^2$	Variance
$P$	Weight matrix
$e^T P e$	Weighted sum of squares of observational residuals
$\hat{\beta}$	Estimated parameters
$H$	Coefficient matrix of constraints
$w$	Outputs of constraint equations
$\tilde{\beta}$	Estimated parameters of constraints
$k$	Lagrange multipliers
$L$	Curve's maximum value
$\gamma$	Growth rate
$x_0$	Curve's midpoint at x-axis
$r$	Measured reflectance
$m$	Entries of reflectance matrix
$M$	Reflectance matrix
$q$	Number of endmembers
$\alpha$	Fractional abundances
$n$	Residuals for spectral bands
$\mu$	Barrier parameter
$s$	Slack parameter
$\omega$	Band weights

$OA$	Overall accuracy
$CCS$	Correctly classified sites
$RS$	Total number of reference sites
$\kappa$	Kappa statistic
$p_0$	Probability of correct classification
$p_e$	Probability of chance agreement
$R^2$	Coefficient of determination
$SS_{res}$	Sum of squares of residuals
$SS_{tot}$	Total sum of squares
$apm$	Abundance performance metric
$card()$	Cardinality
$c$	Entries of abundance confusion matrix
$C$	Abundance confusion matrix



# CHAPTER 1

## INTRODUCTION

### 1.1 Problem Definition

Industrialization, population growth, and rapid urbanization threaten the natural life and resources of the earth. Considering the fact that earth's resources are finite, they may not be able to keep up with the population at its current growth rate. This fact makes optimum management of natural resources very critical. One of the highly esteemed components of the Earth system is wetlands. They are of great importance to the diversity of biota and ecology, thereby to humans (Moore and Garratt, 2006). It is indeed ironic bearing in mind that the coal establishing the ground for the industrial revolution has been obtained through some of the wetlands dating back to ancient times, such as coal-forming swamps.

There are several wetland definitions in the literature, yet a *wetland* can be plainly defined as any unique ecosystem saturated or flooded with water, either seasonally or permanently. Accordingly, they can be generally distinguished by the presence of surface or underground water. Their soil conditions differ from adjacent lands, which is another distinctive property. Moreover, they are abundant in biota, adaptable to wet conditions; in other words, the lack of flooding-intolerant biota characterizes them. With their extreme biological diversity, they are among the wealthiest and most productive ecosystems (Rafferty, 2011). Thus, they are one of the most economically valuable habitats for humans.

Wetlands can be grouped into two categories as coastal and inland wetlands concerning their geolocation (Reddy and DeLaune, 2008) and into six categories as

swamps, marshes, bogs, fens, wet meadows, and shallow water with respect to their hydrological properties (Keddy, 2010).

Wetlands support the ecosystem in a wide range of ways (Mooney et al., 2005; Mitsch and Gosselink, 2015), which are:

- Dissipating stream energy and providing flood control,
- Providing sediment retention,
- Sequestering and storing carbon (contributing to carbon cycle),
- Providing denitrification (contributing to nitrate cycle),
- Removing phosphorus (contributing to phosphorus cycle),
- Reducing sulfur (contributing to sulfur cycle),
- Storing water, thus refilling groundwater,
- Sheltering various species,
- Enabling tourism and recreational activities, and
- In general, having a high and long-term capacity to filter pollutants for enhanced water quality. Therefore, just as forests are called “the lungs of the earth,” wetlands are called the “kidneys of the earth.”

All those benefits, which have an essential role in mitigating climate change and providing sustainable development, are illustrated in Figure 1.1.

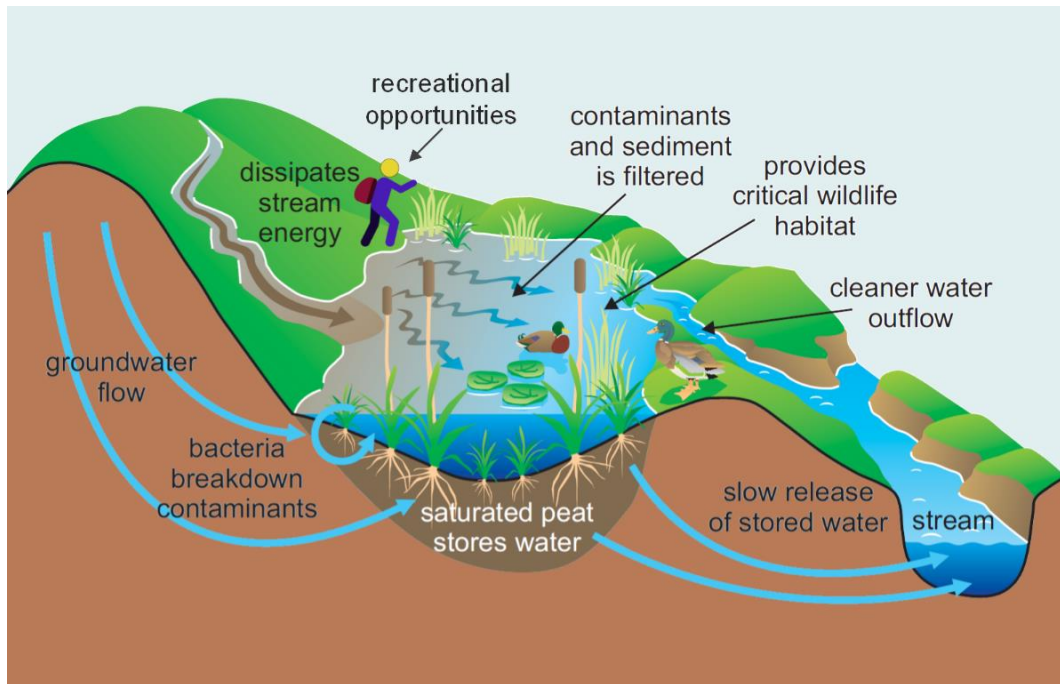


Figure 1.1 Benefits of wetlands (modified from Capital Regional District, 2008)

Since wetlands are such precious entities and matter to all living beings, national and international organizations strive to guarantee their preservation and wise use by means of regulations and treaties. In this respect, an international treaty entitled “The Ramsar Convention on Wetlands of International Importance Especially as Waterfowl Habitat” was signed in the Iranian city of Ramsar in 1971 and came into force in 1975. The Convention is supported by five formally recognized international organizations (Ramsar Convention Secretariat, 2013) that are:

- BirdLife International
- International Union for Conservation of Nature
- International Water Management Institute
- Wetlands International
- World Wide Fund International

These organizations provide technical assistance in line with the agreed goals. According to the investigations, 660 million people benefit from wetlands, which are home to 100 thousand known species (Ramsar Convention Secretariat, 2017). The estimated surface area of worldwide wetlands is 12,1 million km<sup>2</sup> as of 2017. Furthermore, as of January 2022, the number of designated Ramsar Sites and their total surface area are 2.437 and ~2.5 km<sup>2</sup>, respectively (Ramsar Convention Secretariat, 2022). The global distribution of Ramsar Sites is given in Figure 1.2.

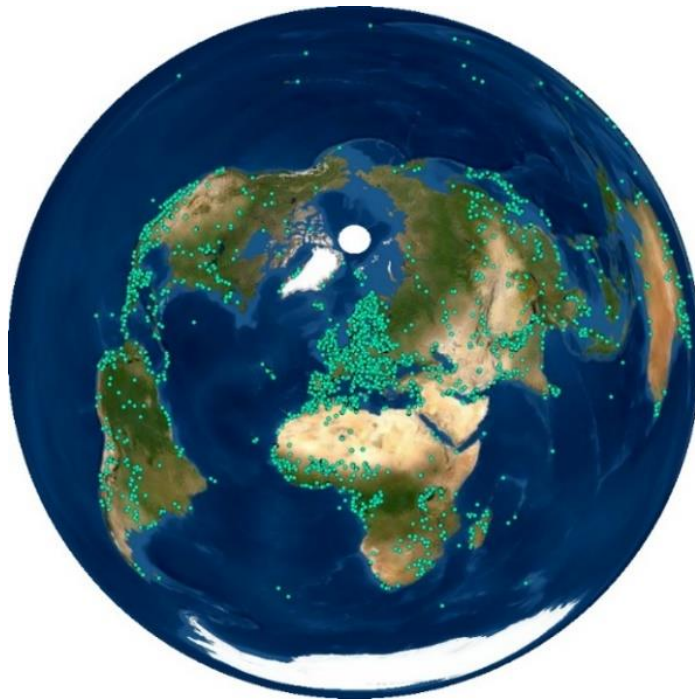


Figure 1.2 Global distribution of Ramsar Sites

Turkey signed the Ramsar Convention in 1993, and it entered into force in 1994. In parallel with this development, the first regulation on wetlands protection was published in the official gazette in 2002. The first regulation was replaced with regulations dated 2005 and 2014, respectively. As of January 2022, the 2014 regulation is in force, including 2017, 2019, and 2021 revisions. There are 14 sites designated as Ramsar in Turkey, given in Table 1.1, with a surface area of 1,845 km<sup>2</sup>. Figure 1.3 shows the locations of these sites.



Table 1.1 Ramsar Sites in Turkey

Name	Site Number	Province	Area (km <sup>2</sup> )	Designation Date
Göksu Delta	657	Mersin	150.0	13.07.1994
Lake Burdur	658	Burdur and Isparta	248.0	13.07.1994
Lake Seyfe	659	Kırşehir	107.0	13.07.1994
Lake Kuş	660	Balıkesir	204.0	13.07.1994
Sultan Marshes	661	Kayseri	172.0	13.07.1994
Kızılırmak Delta	942	Samsun	217.0	15.04.1998
Akyatan Lagoon	943	Adana	147.0	15.04.1998
Lake Uluabat	944	Bursa	199.0	15.04.1998
Gediz Delta	945	İzmir	149.0	15.04.1998
Meke Maar	1618	Konya	2.0	21.07.2005
Yumurtalık Lagoons	1619	Adana	198.5	21.07.2005
Kızören Obrouk	1620	Konya	1.3	02.05.2006
Lake Kuyucuk	1890	Kars	4.2	28.08.2009
Nemrut Caldera	2145	Bitlis	45.9	17.04.2013



Figure 1.3 Geolocation of Ramsar Sites in Turkey

Although they are such valuable ecosystems, their degradation and loss have continued for decades (Daniela et al., 2013; Gardner et al., 2015). Scientific research indicates that 64% of the wetlands have disappeared worldwide since 1900 (Ramsar Convention Secretariat, 2010). Particularly in Asia and Europe, the loss is more significant, which is stressed in various studies (Davidson, 2014; Hu et al., 2017; Leadley et al., 2014). Figure 1.4 shows the shrinkage of wetland areas between 1970 and 2010 through Wetland Extent Index.

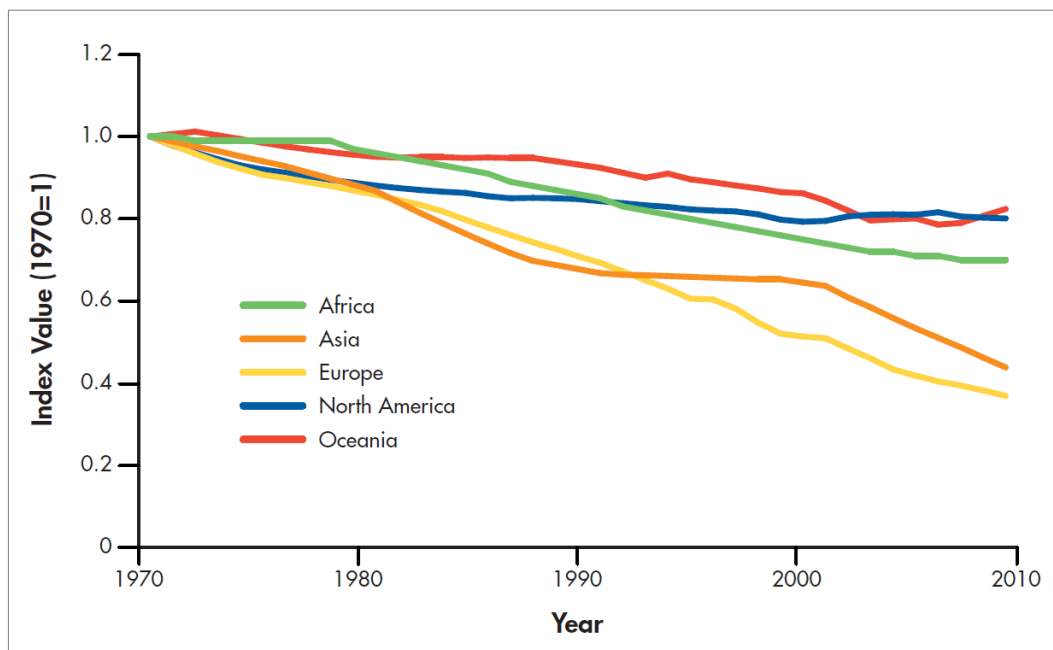


Figure 1.4 Wetland Extent Index for period between 1970 and 2010 (Leadley et al., 2014)

The subject loss can also be interpreted as a significant decrease in access to fresh water, increase in floods, deficiency in carbon storage, and suffering of wetland livelihoods. Although the causes of the loss vary from country to country, they can mainly be listed as follows:

- Dramatic changes in land use triggered by agricultural and farming activities such as rice cultivation and animal grazing

- Construction of dams, dikes, locks, and canals that deteriorates the natural drainage system
- Development of infrastructure works, especially in river valleys and coastal regions
- Air, water, and nutrient pollution

In view of the rapid and continuous loss of those precious habitats, management and conservation become even more crucial (Finlayson et al., 2018; Miklas Scholz, 2016; Russo, 2008; Verhoeven et al., 2006). The accomplishment of these tasks depends on serious monitoring to take necessary precautions. In this regard, monitoring such valuable areas and obtaining crucial information from them play an essential role in contributing to sustainable development. This consideration has been the primary motivation of the studies performed during the preparation of this thesis.

Remote sensing is a very efficient tool for monitoring ecosystems thanks to its ability to collect repetitive information over large areas at various resolutions and wavelengths (Figure 1.5). The practicality and rapidity of data gathering for large areas lower costs as well (Ji, 2008; Lopez et al., 2013; Lyon, 2001; Tiner et al., 2015). In this context, considering the individual size, geographic distribution, and total coverage of wetlands across the earth, remote sensing shines out as the most economically and technically feasible method. Therefore, it is widely used for monitoring these areas and extracting information, primarily land cover classification. However, this classification problem is generally treated at the pixel level, which is not accurate enough to grasp the heterogeneous structure of wetland areas. The pixel-level approach falls short of understanding the wetland dynamics since vast amounts of pixels in subject areas have mixed content. In addition, the existing ontologies are incapable of sensing wetland ecology since water levels and vegetation phenology are very dynamic. Therefore, there is an apparent need for handling mixed pixel problems considering the temporal aspect. Moreover, the

assessment of fractional land cover requires delicate approaches rather than conventional accuracy metrics.

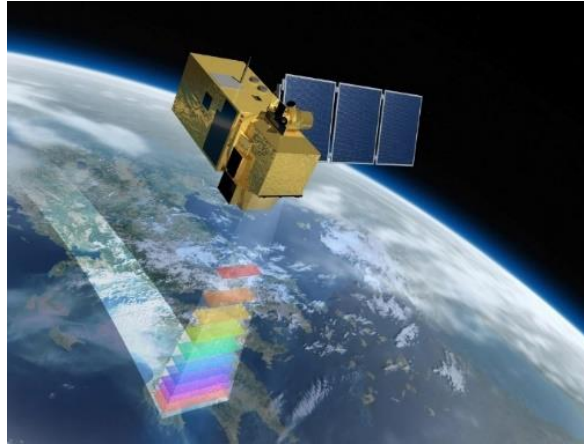


Figure 1.5 Earth observation from space (European Space Agency, 2015)

## 1.2 Research Objectives

The most feasible method using remote sensing tools is investigated to overcome the issues above, and suitable strategies are developed accordingly. In this regard, the first objective of this study is to create a methodology in order to extract accurate boundaries of wetlands for delivering further services to the correct address. Secondly, an appropriate scheme is generated to optimally determine the ontology that can describe the wetland characteristics. This is an essential step because it is impossible to strictly reveal existing conditions and relations without a firm grasp of cover types. To make the proposed procedure utilizable by the whole community, open access satellite imagery is selected as the main data input. Although this increases the applicability and brings economy, two significant obstacles come alongside that are:

- High level of detail provided by high resolution imagery does not exist as the current options for open access Earth observation data are in the medium resolution category.

- Panchromatic band is unavailable in the case of Sentinel-2 imagery. Therefore, alternative approaches should be conducted to upscale bands having lower spatial resolution.

Considering the fact that wetlands contain highly heterogeneous land cover, special approach has to be applied to handle the low detail issue. The sub-pixel analysis is conducted to overcome this problem. In spite of the aforementioned obstacles, medium resolution imagery has a remarkable advantage over high resolution data, which is the presence of data acquired from the different portions of the electromagnetic spectrum. This asset can be conveniently exploited to realize sub-pixel analysis. In this context, the third objective is to develop an enhanced sub-pixel method to extract accurate additional information from each pixel.

Apart from their heterogeneous content, the dynamic structure of wetlands is another concern to be addressed. Thus, another objective of this study is to sort out a spectro-temporal unmixing approach suitable for multispectral satellite images to overcome continuously changing mixed pixels. The multitemporal endmember concept is constituted using diverse seasonal data with this aim in view.

Evaluating the outputs through favorable metrics is imperative once the unmixing methodology is established and tested on sample data. There are various methods in the literature to assess the quality of fractional abundances created by soft (fuzzy) classification techniques. Nonetheless, developing a new metric is the final objective of this study, provided the concern is treated from a slightly different perspective to ensure the interpretation of results straightforwardly.

### **1.3 Overview of Proposed Approach**

On the whole, all critical aspects are investigated and addressed for monitoring the wetlands in an effort to contribute to the conservation of these extraordinary habitats. The flowchart of the research methodology is given in Figure 1.6.

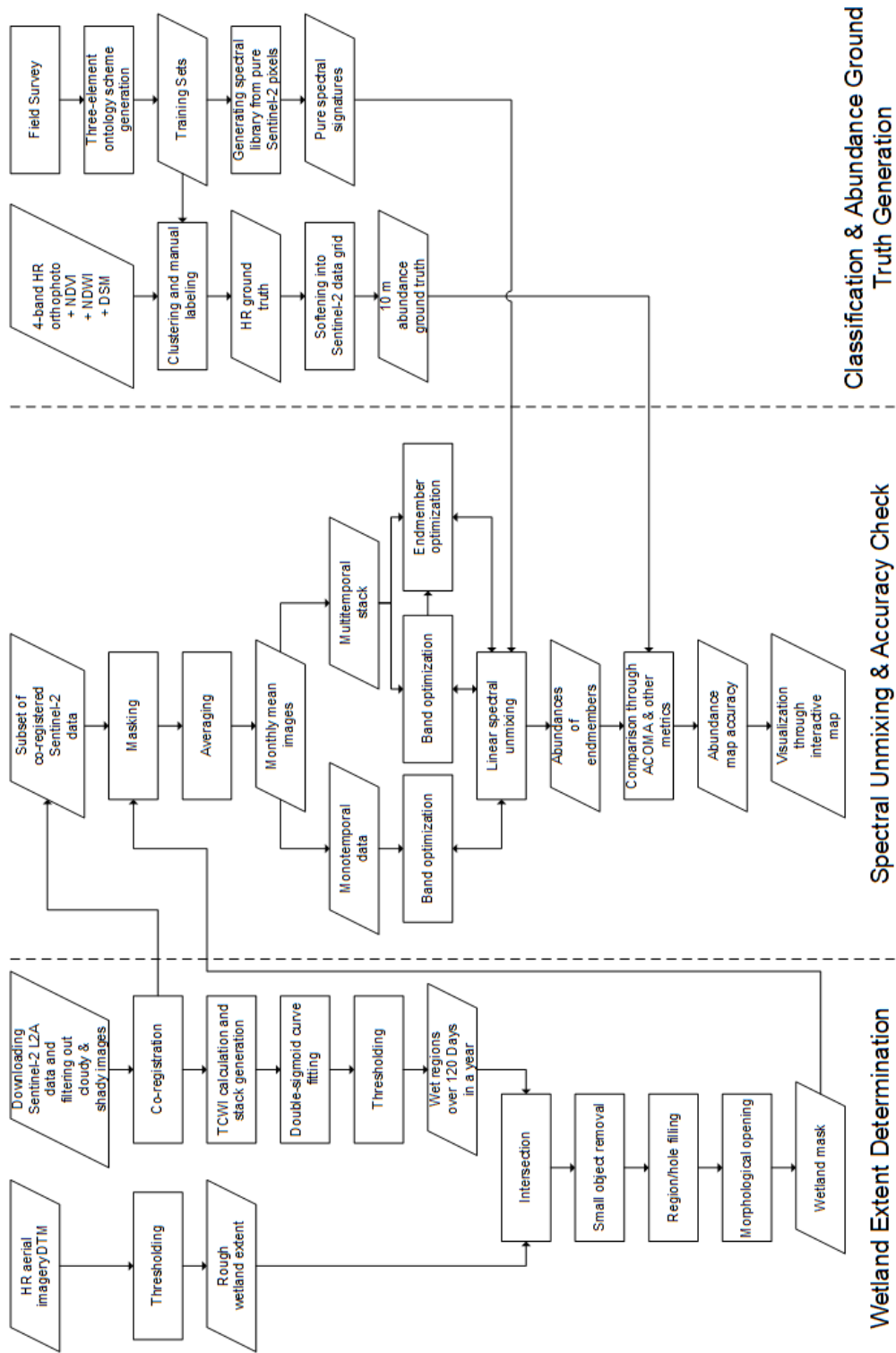


Figure 1.6 Flowchart of research methodology

## 1.4 Contributions of Thesis

In this thesis, a wetland extent determination algorithm and a fully constrained optimized linear spectral unmixing method are presented for the accurate decomposition of wetland habitat that determines the contribution of various land cover types to each pixel, considers the temporal aspect for classification, and explicitly addresses the alteration between water and soil. The major contributions can be summarized as follows:

1. A wetland extent determination strategy is proposed as a pre-processing step through the index-based stack regression and the use of DTM.
2. A three-element ontology library scheme is generated as a basis for the precise endmember selection in a systematic way.
3. A procedure is proposed to create endmember abundance ground truth map through the classification of high resolution aerial imagery and softening into the test data grid.
4. A band weight optimization method is proposed, and the optimized band weights are presented to be used with the same sensor data in similar studies.
5. An endmember optimization method is proposed in the case of utilizing multitemporal endmembers.
6. A new metric is developed, entitled Abundance Confusion Matrix (ACOMA), for the accurate and detailed assessment of fractional cover.

In addition, a list of minor contributions can be given as follows:

1. The applicability of different co-registration algorithms is tested, and the outputs are compared.
2. The applicability of different DEM products as auxiliary input data during the utilization of the extent determination algorithm is tested.
3. Different regularization algorithms are investigated, and their effect on results is revealed.

## 1.5 Outline of Thesis

The rest of this thesis is organized as follows:

In Chapter 2, a thorough literature review is conducted. Different aspects of wetland-related research are overviewed. The methods and approaches are given together with the datasets used. Effects of the utilization of different sensors are mentioned, and complementary features are emphasized.

In Chapter 3, information on the test area is given with descriptive statistics. The change in the legal status of the area from past to present time is indicated. In addition, datasets used for the study are explained in two categories that are ground truth and test. The content of the ground truth is given as products generated using high resolution aerial images. The importance of fieldwork is stressed, and the way how it contributes to the preparation of ground truth through the observations and collected samples is emphasized.

In Chapter 4, the proposed methodology is introduced in detail. The critical points of the operation sequence indicated in the general flowchart are elaborated in subsections. Tested co-registration algorithms are mentioned before moving on to the extent determination, and the final selection is justified. The logic of the extent determination method is explained, and the adopted tools/parameters are indicated. The three-element ontology schema is given, and ground truth generation through the classification supervised by the help of ontology information is explained. The steps followed for obtaining an abundance comparable ground truth are pointed out. The utilized spectral unmixing and adopted improvement strategies are stated, and a novel method for the assessment of fractional abundances is introduced.

In Chapter 5, the experimental results are presented. The obtained accuracies are given for each computation step. The necessity of co-registration of satellite images is demonstrated before moving on to the unmixing operation. The optimized band



weights are presented to the scientific society to be exploited in similar studies utilizing the same satellite data. The different configurations are tabulated for a comprehensible interpretation of the enhancements. The chapter is completed with the discussion part.

In Chapter 6, the conclusions are summarized. The contribution of each operation is revealed in terms of accuracy metrics. The trade-off between introducing temporality and obtaining higher accuracy is specified. The critical steps in the overall process are highlighted, and the significance of the proposed novel assessment strategy is emphasized. The study finishes off with the future recommendations.

The outline of the thesis is given in Figure 1.7.

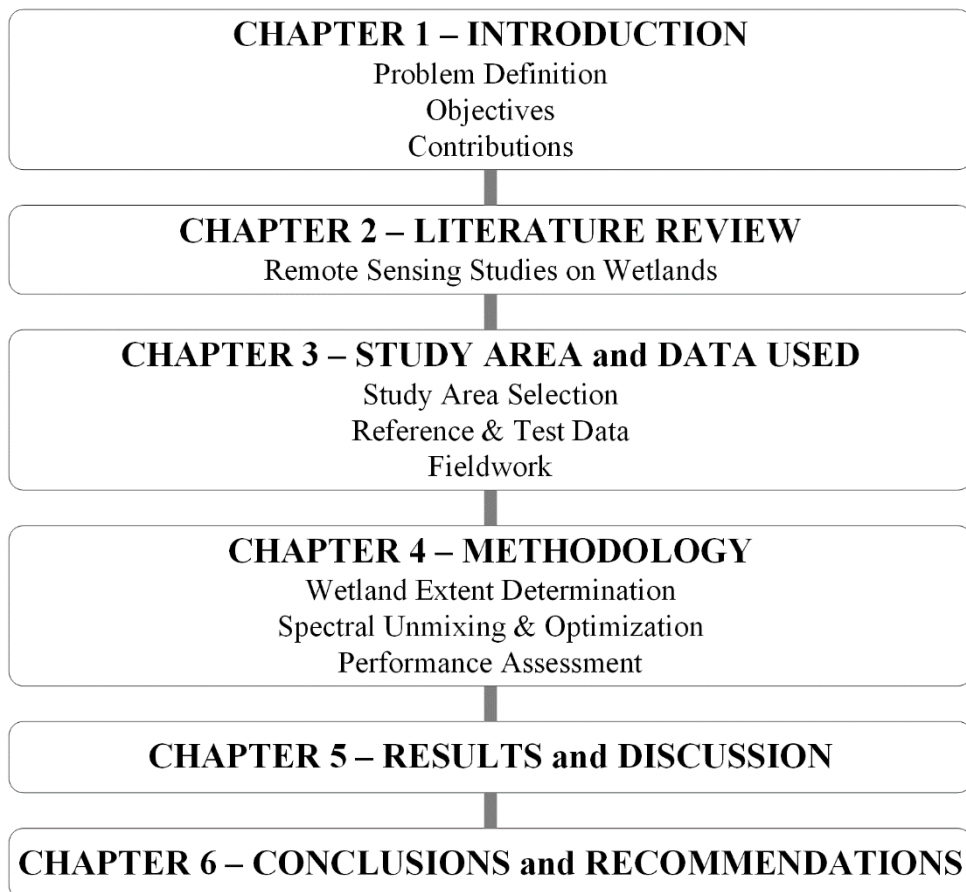


Figure 1.7 Outline of thesis



## CHAPTER 2

### LITERATURE REVIEW

#### 2.1 Wetland Detection

One use of remote sensing for the management of wetlands is detecting their extent. Different approaches have been suggested using optical, radar, and lidar data sources such as aerial imagery, Sentinel, Landsat, Spot, RapidEye, WorldView, Ikonos, QuickBird, Gaofen, MODIS, RADARSAT, ALOS.

Vanderhof et al. (2016) used matched filtering algorithm to reveal surface water connections using Landsat time series. Appropriate bands/indices were extracted from MODIS data via different data reduction techniques in order to map wetland areas (Bansal et al., 2017). Another approach with the same sensor data combines Transformed Wetness Index estimation, time series smoothing, and phenological characterization (Gumbrecht et al., 2017).

Support Vector Machines proved their performance when utilized on Sentinel-2 and WorldView-2 (Araya-López et al., 2018) as well as Sentinel-2, Landsat-8, and RapidEye data (Jakovljević et al., 2019). DTM thresholding, Random Forest (RF) classification, and index exploitation were gathered as the Potential, Existing, Efficient Wetlands (PEEW) approach by Rapinel et al. (2019) to detect different types of wetlands using lidar, Sentinel-1, Sentinel-2, and MODIS annual time series, respectively. Ludwig et al. (2019) presented tile-based dynamic thresholding of water/wetness indices created from the Sentinel-2 time series as another alternative.

## **2.2 Temporal Dynamics of Wetlands**

Various researchers have used remote sensing to detect the temporal dynamics of water within the wetlands. A study focused on water indices (NDWI, MNDWI) using Landsat-5 and Landsat-7 imagery to map water bodies and detect the spatio-temporal change of water inundation on wetlands (Hui et al., 2008). Their methodology successfully determines the water coverage, yet it remains insufficient for estimating the spatio-temporal processes. Another study exploited thresholding on NIR and SWIR for water presence on a large wetland (Lefebvre et al., 2019). They tested Landsat-5, Landsat-7, Landsat-8, and Sentinel-2 data, and it was found that the highest accuracy is obtained from the Sentinel-2 data with a kappa statistic of 0.82. Radar and lidar data as complementary tools to optical data proved their value in understanding the seasonal dynamics of wetlands as well (Kaplan et al., 2019; Zhu et al., 2019).

## **2.3 Wetland Parameters**

Much research has aimed to estimate various wetlands parameters, such as soil organic matter, soil moisture, and biomass using remote sensing. A study was performed focusing on the determination of vegetation spectra using a handheld spectrometer to interpret the impacts of soil salt and water content on plant spectra (Xiaoping et al., 2017). The manually measured data were then compared with the Gaofen-5 Advanced Hyperspectral Imager (AHSI) data. The results indicated that AHSI is better at predicting soil salt content and has advantages in monitoring local high-precision soil salinization. Optimal spectral parameters derived from the Grey Relational Analysis were used to predict soil organic matter content via Backpropagation Neural Network in Ebinur Lake Wetland (Wang et al., 2018). They concluded that the soil organic matter content prediction could be enhanced through fractional derivation, spectral band subdivision, and optimal index selection. Yang et al. (2019) applied Structural Equation Modeling based on statistical approaches to

Sentinel-1 time series data to extract soil properties. They used the ratio of performance to deviation metric to evaluate the results. They obtained a score of 1.47 for soil salinity, 0.99 for soil pH, and 1.00 for soil organic carbon.

## **2.4 Wetland Classification**

Optical and radar remote sensing platforms have been extensively exploited to discover land use/land cover (LU/LC) types using pixel/object-based parametric/non-parametric algorithms. An object-based method was applied for the segmentation and classification of wetlands using Canadian Digital Surface Model (DSM), RapidEye, and Landsat-8 data (Amani et al., 2017). Using the Random Forest classifier in five different study areas, they achieved a mean overall accuracy of 86% and a mean kappa statistic of 82%. The performance of object-based and pixel-based RF algorithms was evaluated to map wetland vegetation using high resolution Gaofen-1 satellite imagery, L-band PALSAR, and C-band RADARSAT-2 data (Fu et al., 2017). They concluded that the object-based method outperforms the pixel-based method by 3 to 10%, and the best overall accuracy, 89.64%, is obtained through the synergistic use of all three sensors. Another application of object-based classification to combined Sentinel-1/2 data produced satisfactory results (Kaplan and Avdan, 2019, 2018). The joint utilization of Sentinel-1 and Sentinel-2 augmented with the System for Automated Geoscientific Analyses (SAGA) Wetness Index for LU/LC mapping on wetlands was evaluated, and a new Object-based Image Analysis (OBIA) approach was proposed by Whyte et al. (2018). Several wetland/non-wetland classes were extracted from Landsat time series spanning 40 years, Gaofen-1 and Spot-7, using five classification methods: maximum likelihood, SVM, iterative self-organizing data analysis (ISODATA), decision tree, and an object-oriented approach (Sun et al., 2018). They concluded that the decision tree provides the highest accuracy, whereas ISODATA has the lowest. Combined optical and SAR data were correctly classified via machine learning algorithms such as RF, resulting in high accuracies of over 90% for the

selected study sites (Salehi et al., 2019). Rather than mapping classes altogether, individual classification using a different feature selection for each class was adopted by Mahdavi et al. (2019). They applied spectral analysis to determine class levels to be mapped, and a merging scheme was established for the remaining classes to escalate the accuracy of the target class. They ended up having overall accuracies of around 93%. Different configurations of RADARSAT-2, simulated compact polarimetric RADARSAT Constellation Mission, and various DEM data were used for the classification of six land cover types with Random Forest (Banks et al., 2019). They stressed the importance of acquisition period, incidence angle, data variations, and elevation models. Various studies demonstrated the productivity and indispensability of vegetation/water indices for LU/LC classification using both multispectral (Doughty and Cavanaugh, 2019) and hyperspectral data sources (Domínguez-Beisiegel et al., 2016; Shen et al., 2019; Stratoulas et al., 2018).

## **2.5 Bathymetry**

The determination of bathymetry in shallow waters is also a famous line of research. A physics-based method was implemented to obtain the remote bathymetry and tested on Worldview-2 data by Eugenio et al. (2013). The potential of Sentinel-2 was assessed for water depths through WASI-2D bio-optical modeling tool, which was found to be promising in shallow waters (Dörnhöfer et al., 2016). An optical empirical algorithm was used to evaluate the robustness of experimental procedures for the development of Satellite-Derived Bathymetry (SDB) models for shallow waters close to the river mouth (Vilar et al., 2018). The efficiency of WorldView-2 data on water depth measurements was evaluated using the Lyzenga Bathymetry Model (Ebaid et al., 2018) as well as Radiative Transfer Model (RTM) (Abasolo et al., 2018). Hyperspectral data, no wonder, were also used for obtaining accurate depth estimation through algorithms based on the water's spectral characteristics (Özdemir and Leloğlu, 2014), as well as enhanced benthic classification accuracy via introducing the Bottom Index algorithm (Kakuta et al., 2018). Cloud computing,

particularly Google Earth Engine (GEE), has become widely used after significant improvements. Collecting low-cost site data to augment publicly available Sentinel-2 optical satellite data accessed by GEE has been adopted to estimate bathymetry using an empirical pre-processing workflow (Traganos et al., 2018). SBD proved its worth when manipulated on Landsat-8 and Pleiades in addition to Sentinel-2 (Duplančić-Leder et al., 2019). Support Vector Regression trained using bathymetric lidar surveys was tested on a UAV point cloud for obtaining improved depth information (Agrafiotis et al., 2019). Research conducted by Casal et al. (2019) concluded that the Linear Band Model outperforms the Band Ratio Model for bathymetry derivation from Sentinel-2 data. The bathymetry algorithm proposed by Yunus et al. (2019) proved that RF is more favorable than empirical models for predicting bathymetry using Sentinel-2 and Landsat-8 data. They discovered that the applied methodology is efficient, particularly at 0 - 10 m coastal depths and up to 30 m clear lake water. Other scientists also investigated the abilities of the Sentinel-2 constellation, and the efficiency of the coastal aerosol band was explored for mapping the dominant coastal marine habitats in addition to the bathymetry in various survey locations in the East Mediterranean (Poursanidis et al., 2019). A ratio transform model was adopted for generating bathymetric maps using Sentinel-2A and 2B in South Florida by Caballero and Stumpf (2019). They justified the ability of Sentinel-2 satellites to extract bathymetric information as well. They calculated median errors around 0.5 m for depths up to 18 m.

## **2.6 Data Fusion**

As in many other research areas, one of the biggest challenges in the area of wetland mapping is to extract more information from the existing data in terms of spatial and temporal properties. There are two main approaches to cope with this issue, which are data fusion (Chang and Bai, 2018; David and Llinas, 2001; Klein, 2012; Lillesand et al., 2015; Mitchell, 2012) and spectral unmixing (Bioucas-Dias and Figueiredo, 2010; Dobigeon et al., 2016; Iordache et al., 2011; Khajehrayeni and Ghassemian,

2020; Li et al., 2012). Flexible Spatio-Temporal Data Fusion (FSDAF) is among the efficient fusion models used for vegetation mapping that blends frequent low and infrequent high resolution data (Zhu et al., 2016). Another fusion model generating enhanced images by blending multispectral and hyperspectral data through guided filtering was tested on the Poyang Lake wetland (Chen et al., 2017). In addition, Spatio-Temporal Adaptive Fusion Model for NDVI products (STAFFN) has been presented by Chen et al. (2018) to combine spatial and temporal features from multiple sensors in an effective way. A decision-based fusion workflow using lidar, radar, and optical data was also developed for wetland classification (Montgomery et al., 2019). Machine and deep learning-based fusion techniques were proposed in this area as well (López-Tapia et al., 2021; Mallick et al., 2021; Mishra and Shahi, 2021). There are various studies using spectral unmixing techniques on wetlands to understand the complex mixture of various components. A method combining RF and Spatial Attraction Models was applied to Landsat data to map wetland flooding in China (Li et al., 2019). A color mixture analysis method was proposed based on the Hue-Saturation-Value (HSV) color space for improving the accuracy and efficiency of Fractional Vegetation Cover (FVC) estimation from UAV-captured RGB images (Yan et al., 2019). A new spectral unmixing approach was applied to Landsat satellite images to extract surface water area information from stock ponds by Jarchow et al. (2020). Chang et al. (2021) have made an effort to detect sub-pixel level changes via clustering and segmenting multitemporal hyperspectral images. Their unmixing method has yielded promising results when tested on the Yellow River Estuary wetland. A sparse unmixing algorithm was proposed by Ding et al. (2021) to detect wetland locations using Landsat-8 OLI multispectral images, and the classification accuracies were compared with the results of the traditional linear unmixing approach. Another spectral unmixing algorithm based on constrained linear least squares established upon an adaptive approach was suggested by Na et al. (2021) for wetland mapping.



## CHAPTER 3

### STUDY AREA AND DATA USED

#### 3.1 Study Area

According to the Ministry of Agriculture and Forestry of the Republic of Turkey (2022), there are 93 wetlands in Turkey grouped under three categories that are international importance (Ramsar), national importance, and local importance. Table 3.1 shows the categorical distribution and area information of wetlands in Turkey.

Table 3.1 Wetlands in Turkey

Wetland Statue	Area (ha)	Forest Area (ha)	Forest Area (%)	Number
International Importance (Ramsar)	184,487	5,623	3.0	14
National Importance	869,697	67,572	7.8	59
Local Importance	28,660	844	2.9	20
Total	1,082,844	74,039	13.8	93

While selecting the study area, closeness is the primary consideration for conveniently carrying out site visits, provided that the region possesses the required investigation criteria. These criteria are diversity in vegetational content, substantial water mass, and considerable total coverage. Figure 3.1 illustrates all the wetlands across Turkey.

In Ankara, there is just one official wetland, namely Tol Lake. It is in the national importance category with an area of 1.4 km<sup>2</sup>. Apart from its relatively small surface area, it lacks water mass and is subject to human interactions like established irrigation canals. Taking these disadvantages of Tol Lake into consideration,

neighboring cities are examined for a more suitable site. Among the alternatives, Balıkdamı wetland appears to be the most appropriate option meeting the criteria mentioned above.

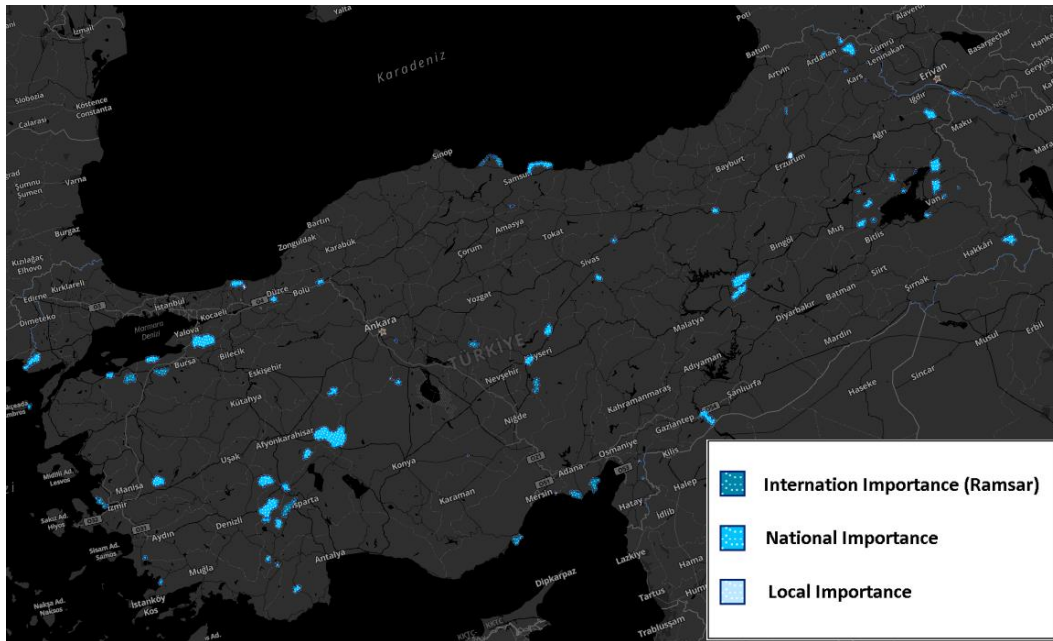


Figure 3.1 Wetlands in Turkey

Balıkdamı, one of the 59 wetlands of Turkey in the national importance category, is selected as the study area in this thesis. It is located west of Central Anatolia within the boundaries of Eskişehir. It is approximately 115 km away from Eskişehir and 135 km away from Ankara city centers. It is about 14.7 km<sup>2</sup> consisting of many ponds and reed beds, and the third-longest river in Turkey, Sakarya, passes through it. It hosts a wide variety of fish types; hence, it is given a name implying the house of fishes by the locals. In addition, the existence of numerous vegetation and bird types increases its importance and value. The area was declared a second-degree natural protection area, wildlife protection area, and wildlife improvement area in 1980, 1994, and 2005, respectively. It officially gained the wetland of national importance status in February 2019.

The bounding box for the study area is designated as 39°10'10" to 39°13'15" N latitudes and 31°35'46" to 31°40'08" E longitudes, given in Figure 3.2. The altitudes for this frame range from 792 m to 929 m.

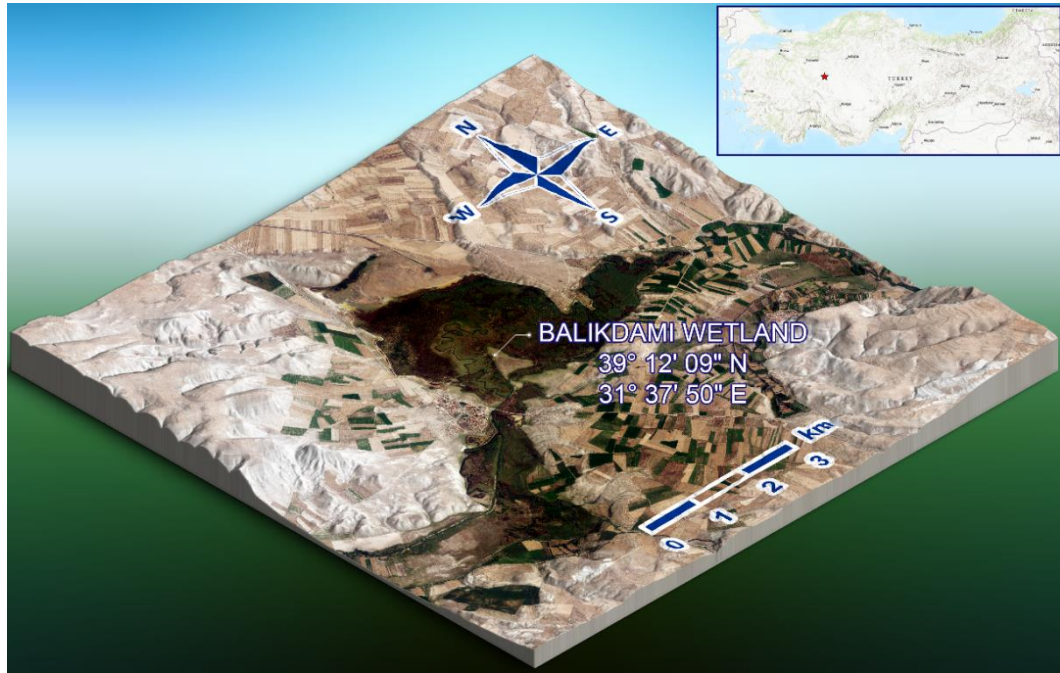







Figure 3.2 Location and topography of Balıkdami






A two-year study conducted between 2002 and 2003 justifies the richness of Balıkdami flora, revealing that there are 51 families and 250 taxa in the region (Koyuncu et al., 2008). The most prevalent families and their distributions are given in Table 3.2.

Table 3.2 Dominant vegetation families in Balıkdamı

Family	Number of Taxa	Rate (%)	Sample Species
Brassicaceae (la) Crucifers (en)	31	12.4	
Poaceae (la) Grasses (en)	29	11.6	
Fabaceae (la) Legumes (en)	25	10.0	
Asteraceae (la) Asters (en)	25	10.0	
Lamiaceae (la) Mints (en)	18	7.2	

*Note. Photos taken from Wikipedia (2022)*




Table 3.2 Dominant vegetation families in Balıkdamı (continued)

Family	Number of Taxa	Rate (%)	Sample Species
Caryophyllaceae (1a) Pinks (en)	12	4.8	
Apiaceae (1a) Umbellifers (en)	10	4.0	
Ranunculaceae (1a) Buttercups (en)	9	3.6	
Liliaceae (1a) Lilies (en)	9	3.6	
Boraginaceae (1a) Borages (en)	8	3.2	

*Note. Photos taken from Wikipedia (2022)*


Balıkdamı is also known as Bird Paradise since it is located at a wide variety of bird populations' migratory routes. According to observations made between 2017 and 2019, 210 bird species from 47 families of 18 orders are identified in the region (Ozkazanc et al., 2019). Among these species, one is categorized as endangered, two as vulnerable, and seven as near threatened with respect to the International Union for Conservation of Nature Red List of Threatened Species, founded in 1964. Details are given in Table 3.3.

Table 3.3 Balıkdamı bird species on red list

Species	Red List Category	Photo
Egyptian vulture	Endangered	
Lesser kestrel	Vulnerable	
Eastern imperial eagle	Vulnerable	



*Note. Photos taken from Wikipedia (2022)*

Table 3.3 Balıkdamı bird species on red list (continued)

Species	Red List Category	Photo
Ferruginous Duck	Near threatened	
Red Kite	Near threatened	
Cinereous vulture	Near threatened	
Pallid harrier	Near threatened	
Red-footed falcon	Near threatened	

*Note. Photos taken from Wikipedia (2022)*

Table 3.3 Balıkdami bird species on red list (continued)

Species	Red List Category	Photo
Black-tailed godwit	Near threatened	
European roller	Near threatened	

*Note. Photos taken from Wikipedia (2022)*

### 3.2 Data Used

This study uses three types of optical sensor datasets in the implementation and evaluation parts. The summary of the datasets is given in Table 3.4. The details are provided in the following three sections.

Table 3.4 Details of data used

Data Type	Aerial Imagery		Satellite Imagery	
Sensor	UltraCam Eagle	UltraCam Eagle Mark3	Sentinel-2	
Acquisition Date	15.07.2015	20.07.2019	2018/2019/2020	April/July 2019
Content	Stereoscopic (forward overlap – 60%) (side overlap – 40%)		Monoscopic (fo – 45%) (so – 40%)	
			Single Frame L2A	



Table 3.4 Details of data used (continued)

<b>Number of Frames</b>	20		12	106	6
<b>Bands Used</b>	Blue, Green, Red, NIR		Blue, Green, Red, NIR	2, 3, 4, 8, 11, 12	2, 3, 4, 5, 6, 7, 8, 8A, 11, 12
<b>Ground Sampling Distance</b>	30 cm		30 cm	10 m*	
<b>Radiometric Resolution</b>	8-bit		8-bit	16-bit	
<b>Generated Product</b>	DSM	DTM	Orthophoto	TCWI Stack	Monthly mean images
<b>Intended Purpose</b>	Introduced as an additional band in orthophoto classification	Utilized in rough wetland extent determination & ortho-rectification of 2019 aerial imagery	Utilized as ground truth in spectral unmixing assessment	Utilized in precise wetland extent determination	Utilized in spectral unmixing

\* 20 m bands are resampled to a 10 m grid using the Nearest Neighbor algorithm

### 3.2.1 Ground Truth

Ground truth data are prepared using high resolution aerial imagery. Two different datasets are exploited, acquired by UltraCam Eagle on 15.07.2015 and UltraCam Eagle Mark3 on 20.07.2019. The Ground Sampling Distance (GSD) of both image sets is 30 cm. These data are delivered with camera calibration reports and exterior orientation parameters by the data providers. Since accurate geolocation and orientation information exists, ground control point (GCP) collection and photogrammetric adjustment process are not applied. Because of the fact that 2015

data are stereoscopic, they are used to generate Digital Surface Model (DSM) and Digital Terrain Model (DTM). As shown in Figure 3.3, 2019 images do not have model overlays. Therefore, the 2015 DTM is utilized to produce orthophoto from the monoscopic 2019 aerial imagery, which forms the basis of the verification stage. The same DTM is also adopted in the wetland determination procedure. Besides, the 2015 DSM is appended to the 2019 orthophoto as an additional band to enhance the image classification later on.

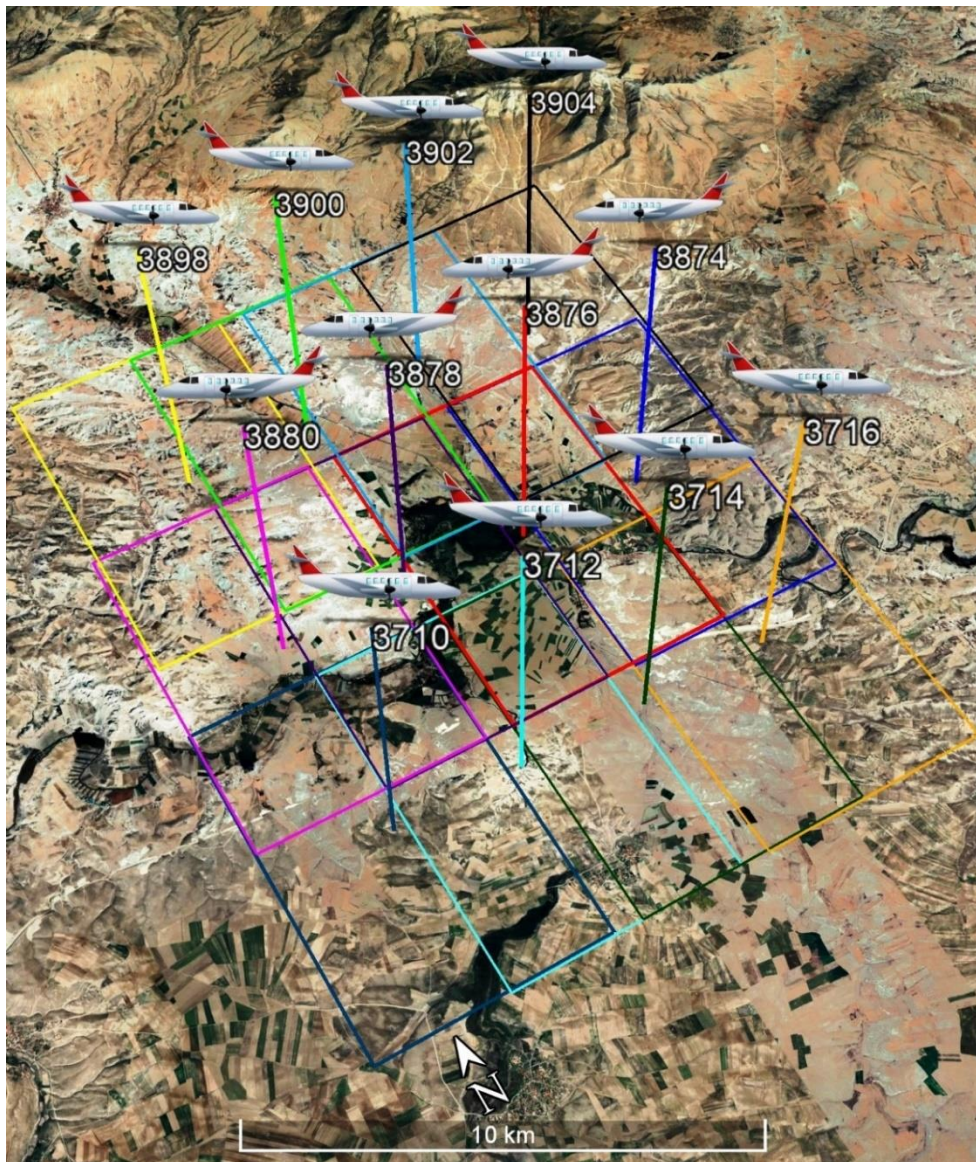


Figure 3.3 Footprints of 2019 aerial imagery

### 3.2.2 Fieldwork

In addition to the aerial imagery, observations carried out during the site visits in three successive years from 2019 to 2021 contribute to the preparation of the ground truth. Many photos are taken, soil/vegetation samples are collected, and video recording is done through a low-cost UAV during the site visits. Photos of different land covers are used to determine the classes (Figure 3.4), and vegetation/soil samples collected on the site (Figure 3.5) help to distinguish fine details. In addition, UAV video supports identifying the land cover, particularly in hard-to-reach regions. An image frame exported from the UAV video is given in Figure 3.6.



Figure 3.4 Passing through Sakarya River (19.08.2020)



Figure 3.5 Ranunculus sample collection (19.08.2020)



Figure 3.6 Single image frame exported from UAV video record (19.08.2020)

All collected information is organized as a log book (Appendix A) not only for this study but also for other ecology and remote sensing research. In addition, the analysis report of the soil samples is given in Appendix B, which was prepared by a professional laboratory.

### 3.2.3 Test Data

In this study, Sentinel-2 optical satellite data are used for both wetland extent determination and supervised spectral unmixing processes. Sentinel-2 is a wide-swath, multispectral imaging mission operated by the European Space Agency (ESA), providing 10m/pixel resolution at best. The constellation is comprised of two polar-orbiting satellites, Sentinel-2A and Sentinel-2B, launched on 23.06.2015 and 07.03.2017, respectively. The satellite couple occupies the same sun-synchronous orbit, yet they are phased at 180° (Figure 3.7).

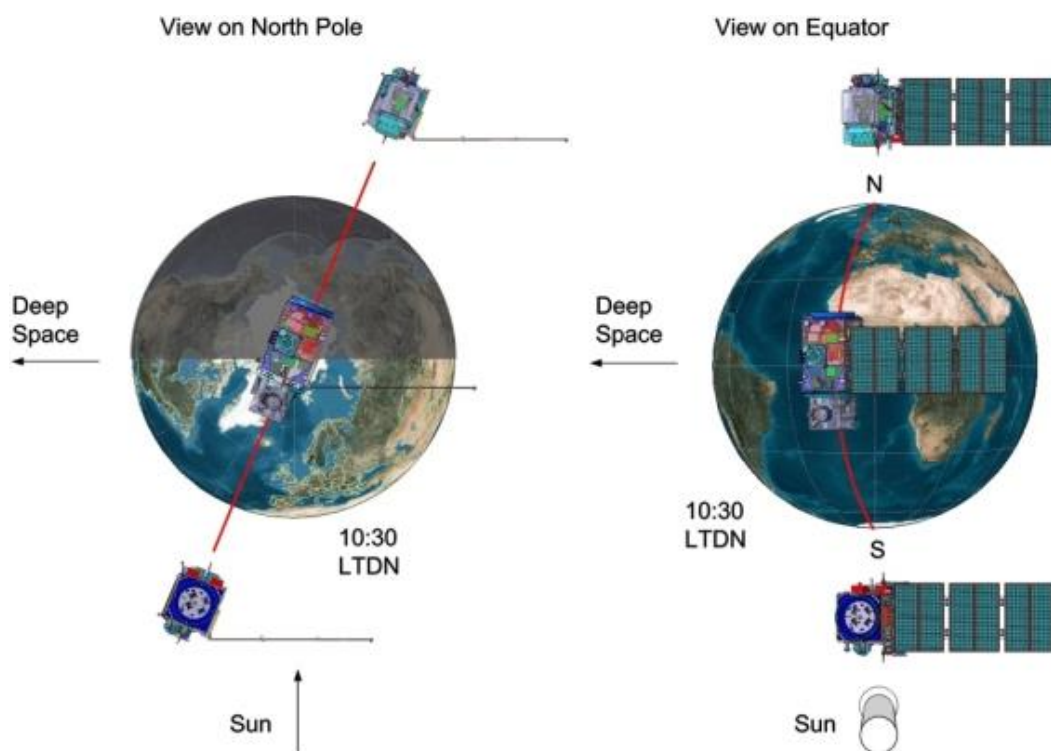


Figure 3.7 Orbital configuration of Sentinel-2 satellites (European Space Agency, 2021)

This orbital configuration results in a high revisit time of 5 days under cloud-free conditions. With a swath width of 290 km, a systematic global optical data acquisition is obtained, contributing to climate change investigation, land monitoring, planning, emergency management, surveillance purposes, and many other applications. Each satellite is equipped with a dual-frequency Global Navigation Satellite System (GNSS) receiver in order to measure orbital position. Both satellites have dedicated propulsion systems to maintain their orbital accuracy. The mean orbital altitude, orbital inclination, orbit period, ground track deviation, and Mean Local Solar Time (MLST) at the descending node are 786 km, 98.62°, 100.6 min,  $\pm 2$  km, and 10:30 a.m., respectively. The reason for choosing this MLST value is to provide a balance between the level of solar illumination and potential cloud cover. Another advantage of the adopted MLST value, which is close to the local overpass time of Landsat missions and almost identical to the Spot-5 configuration, is to enable the integration of Sentinel-2 data with existing and historical missions and support the establishment of long-term time-series datasets (European Space Agency, 2022a). There are 13 spectral bands in the instruments; four provide 10 m, six provide 20 m, and three provide 60 m spatial resolutions. The details are given in Table 3.5.

Table 3.5 Spectral bands for Sentinel-2 sensors (European Space Agency, 2021)

	S2A		S2B		
Band Number	Central Wavelength (nm)	Bandwidth (nm)	Central Wavelength (nm)	Bandwidth (nm)	Spatial Resolution (m)
1	442.7	21	442.3	21	60
2	492.4	66	492.1	66	10
3	559.8	36	559	36	10
4	664.6	31	665	31	10
5	704.1	15	703.8	16	20
6	740.5	15	739.1	15	20

Table 3.5 Spectral bands for the Sentinel-2 sensors (continued)

	S2A		S2B		
Band Number	Central Wavelength (nm)	Bandwidth (nm)	Central Wavelength (nm)	Bandwidth (nm)	Spatial Resolution (m)
7	782.8	20	779.7	20	20
8	832.8	106	833	106	10
8a	864.7	21	864	22	20
9	945.1	20	943.2	21	60
10	1373.5	31	1376.9	30	60
11	1613.7	91	1610.4	94	20
12	2202.4	175	2185.7	185	20

There are five Sentinel-2 product types, which are:

- Level-0 : Compressed raw image data in Instrument Source Packet (ISP) format
- Level-1A : Decompressed Level-0 raw image data
- Level-1B : Top of atmosphere (TOA) radiances in sensor geometry
- Level-1C : Top of atmosphere (TOA) reflectances in cartographic geometry
- Level-2A : Bottom of atmosphere (BOA) reflectances in cartographic geometry

The Level-0 and Level-1A products are not released to users. The highest product level made available to users is Level-2A. Each Level-2A product comprises 100x100 km<sup>2</sup> tiles in UTM/WGS84 projection and has additional outputs such as Aerosol Optical Thickness Map, Water Vapor Map, and Scene Classification Map having Quality Indicators for cloud and snow probabilities at 60 m resolution. On the other hand, the cirrus band (B10) is omitted as it does not contain surface

information. Level-2A products were not used to be systematically generated at the ground segment before March 2018. The users could only produce them through the Sentinel-2 Toolbox using the Level-1C product as input. Starting from that period, they have been generated over Europe. The production was extended to global coverage in December 2018. However, the users can still generate Level-2A data themselves by playing with the processing parameters of their own will.

In this study, Level-2A products generated at the ground segment spanning three years (2018-2019-2020) are utilized. There are 215 available frames for the selected study area belonging to the mentioned period. After the elimination of cloud and shadow-covered data, 106 frames remain. In the wetland extent determination part, B2, B3, B4, B8, B11, and B12 of all 106 frames are used in line with the Tasseled Cap Water Index (TCWI) calculation. In the latter part, 6 out of 106 frames are utilized. All bands except the remaining two 60 m ones (B1 and B9) are benefited, and monthly mean images are formed using the ten bands accordingly.



## CHAPTER 4

### METHODOLOGY

The methodology proposed to determine wetland extent and ground characteristics is already shown schematically in Figure 1.6, together with the preparation of ground truth data to assess the final outputs. The details of these three approaches are explained in the following sections, and related components of the general flowchart are shared separately. In this respect, the flowchart, including Sections 4.1, 4.2, and 4.3, is given in Figure 4.1.

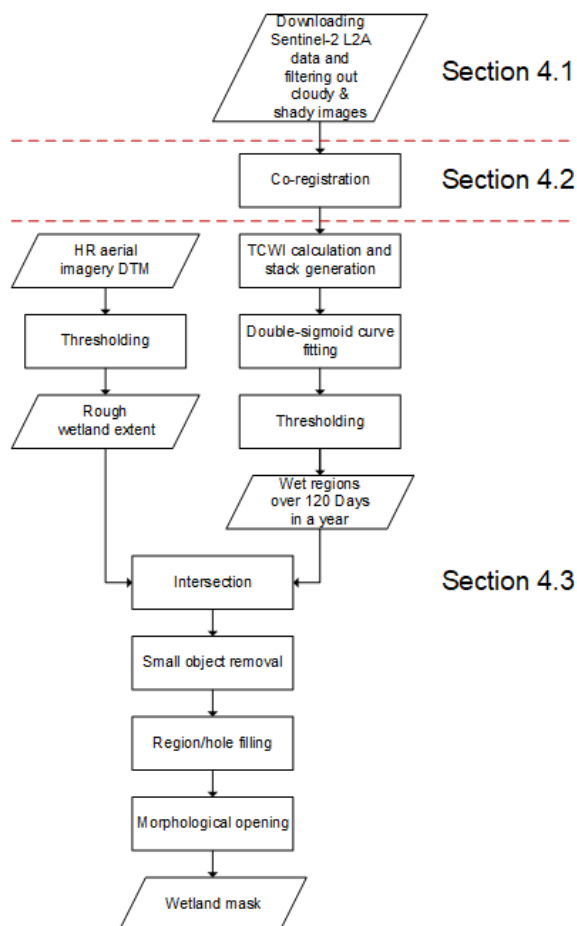


Figure 4.1 Flowchart of Sections 4.1, 4.2, and 4.3

#### **4.1 Downloading and Pre-processing of Sentinel-2 Satellite Imagery**

Sentinel-2 data can be freely downloaded through the Copernicus Open Access Hub operated by the European Space Agency (ESA). The hub provides complete and open access to Sentinel-2 user products. In addition, platforms being a part of the Copernicus Data and Information Access Services (DIAS) can also be utilized to gather subject products. It is likely to make a request for archive data that are generally offline. The data retention period for synchronous access differs according to the profiles in the case of using Open Access Hub. At least the latest month is guaranteed to be delivered, and asynchronous access is provided to archive data, which are restored for download within one hour after request and available for download via HTTPS at least for the subsequent three days. When dealing with time series, this can be challenging and time-consuming.

In this study, data download is performed through the Google Earth Engine. This computing platform allows users to reach multi-petabyte satellite imagery from various sources and realize geospatial analyses using Google's infrastructure. The platform is free for academics and researchers. There are several ways to utilize the provided services, which are a web-based IDE called the Code Editor, a lightweight web application called the Explorer, and Python/JavaScript libraries. The Code Editor is used for the data acquisition in this study, enabling JavaScript implementations. The platform allows different data filters such as date, cloud, and shadow. There are two options for cloud filtering in this respect. Since cloudy pixel percentage is provided in the satellite metadata, introducing a percentage as a threshold is the first option. The second is benefiting from the bitmask band with cloud mask information (QA60) provided with the image data. The problem with the first one originates from percentage information being granule-specific. The region of interest might be a small part of the granule, yet the cloud cover can accumulate in that area. Therefore, the user does not necessarily end up having cloudless imagery, even setting a low threshold. Although the second option works on the

region of interest, it is prone to false negatives to an extent. Therefore, a manual check is carried out on the entire region of interest data to ensure a solid result.

Apart from the fast access to different sensors and levels of original data, the platform is quite an incentive to apply geospatial analyses, thanks to the potent Google infrastructure. During the studies, operations such as time series analyses, calculation of indices, and pseudo-bathymetric information extraction, are realized, particularly before ultimate study area selection as a support tool to find out the best region meeting different research criteria (Figure 4.2 and Figure 4.3).

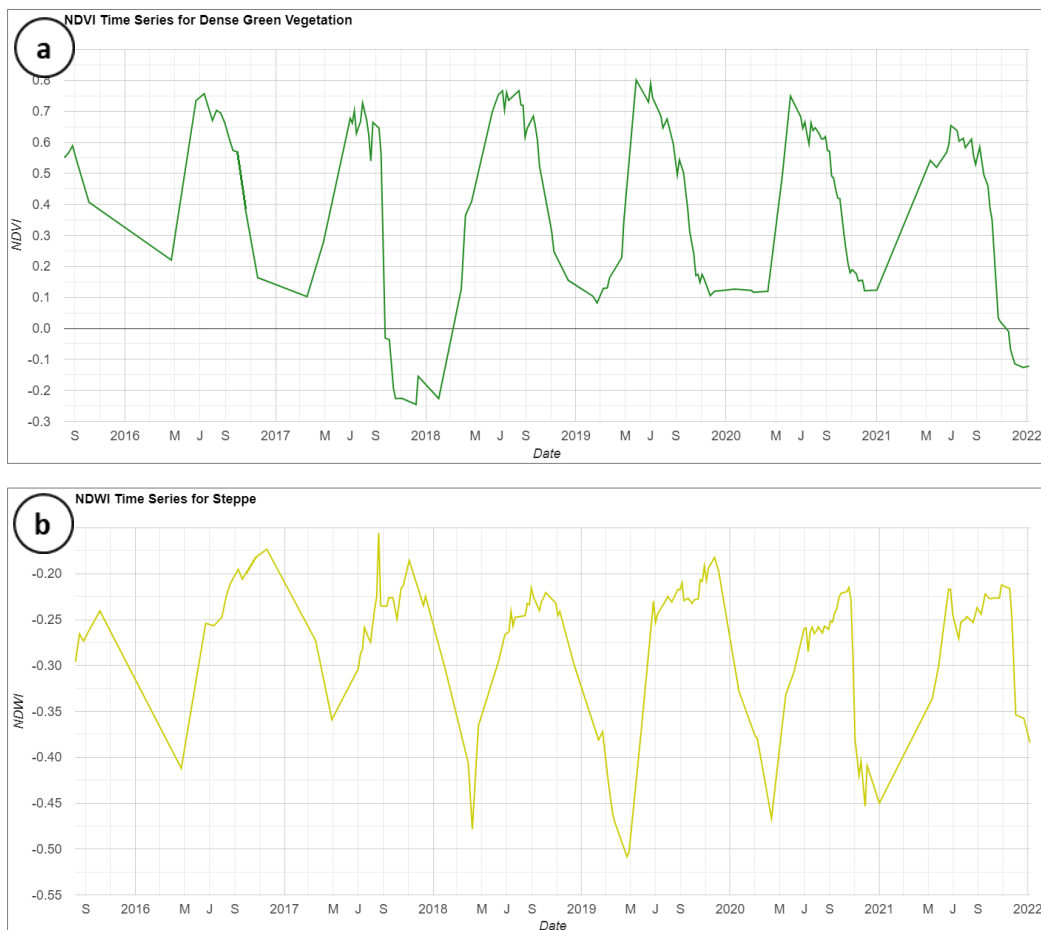


Figure 4.2 Index time series from 7 years data (a) Averaged NDVI of sample vegetation polygon (b) Averaged NDWI of sample soil polygon

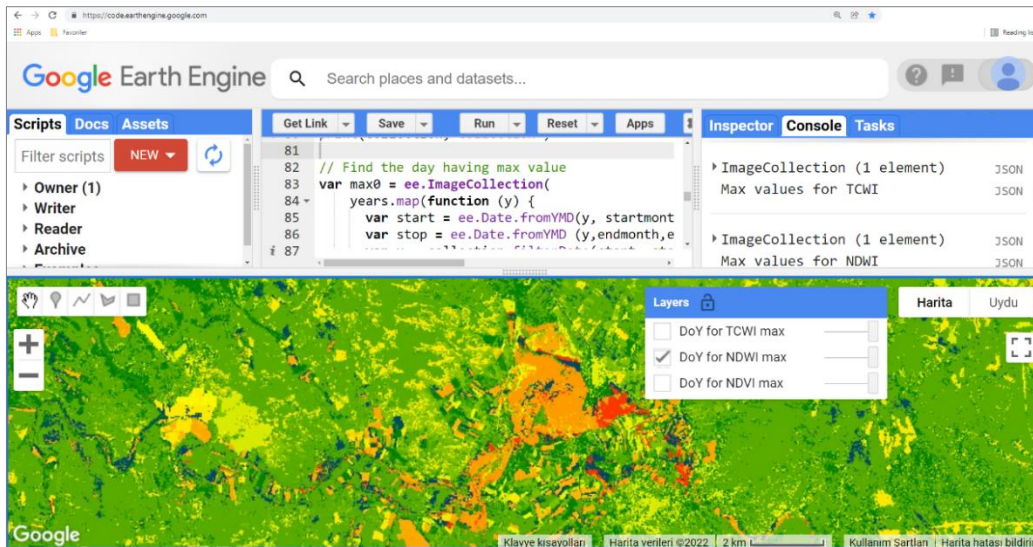


Figure 4.3 Dynamic map showing number of days of 2018 for max index values

## 4.2 Co-registration of Satellite Imagery

Subsequent to downloading and filtering test data, Sentinel-2 L2A images are co-registered to the high resolution reference image. For this task, four different algorithms are examined, which are:

1. Intensity-based in-house MATLAB co-registration routine.
2. Lucas-Kanade algorithm based GeFolki (Geoscience Extended Flow Optical Lucas-Kanade Iterative) Co-registration Processor (Brigot et al., 2016).
3. Cross-correlation based SNAP radar Co-registration Tool (European Space Agency, 2022b).
4. Python package working in the frequency domain, namely Automated and Robust Open-Source Image Co-Registration Software (AROSICS) (Scheffler et al., 2017).

Two test data frames are co-registered to high resolution orthophoto to compare the algorithms. One frame is selected from close to the date of the master image, whereas

the other is from a different season. The procedure is performed using the green bands of reference and target images.

### 4.3 Determination of Wetland Extent

The idea behind the proposed approach is to mathematically detect lands that are mostly wet in a year, as the name wetland implies. The two primary inputs are high resolution DTM, if possible, and medium resolution satellite images spanning a whole year. The former data are used to detect wetland bed via thresholding. Although this step itself should provide adequate information in theory, only rough boundaries can be extracted in reality because of human interference in such fruitful areas. It is very likely to have regions separated from the natural habitat. The latter data step in at this point. In order to define the annual wetness behavior, data preferably from multiple years to construct a more vigorous representation of a yearly dataset are sorted into month-day order for minimizing the gaps between data acquisition dates and estimation errors caused by hard-to-model natural effects.

Another crucial point is to decide the basis index. In this study, Tasseled Cap Wetness Index (TCWI) is adopted because of its proven success in wetland mapping (Ordoyne and Friedl, 2008). The formula used to calculate TCWI is as follows (IDB Project, 2022):

$$\begin{aligned} \text{TCWI} = & 0.1509 B_2 + 0.1973 B_3 + 0.3279 B_4 + 0.3406 B_8 \\ & - 0.7112 B_{11} - 0.4572 B_{12} \end{aligned} \quad (4.1)$$

After calculating TCWI for each co-registered frame, sorting them regarding month-day order, and stacking them, it is possible to estimate wetness values of a single location throughout a year. When the scatter of data points is examined, fourth-order polynomial and double-sigmoid functions are chosen to be fitted on data because of their congruence. Two methods are performed individually on each multiband  $\mathbf{b}$

image stack composed of  $h \times w$  pixel data frame for 365 days, as shown in Figure 4.4.

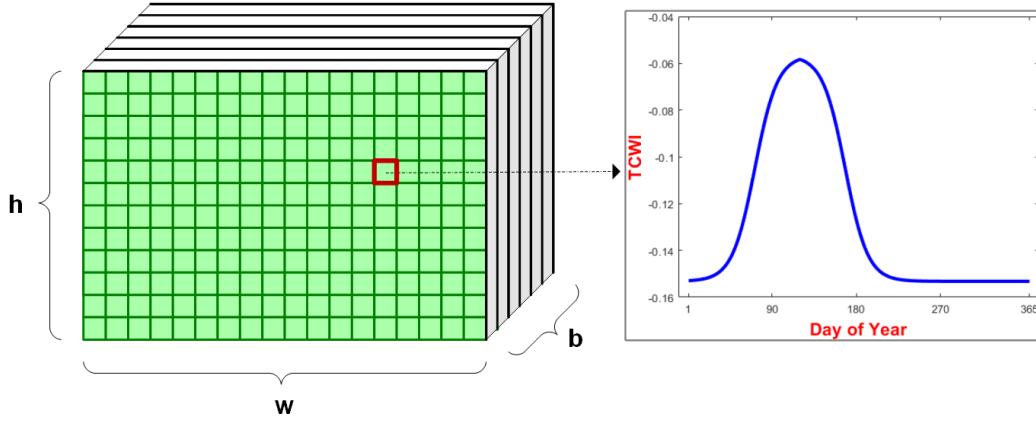


Figure 4.4 Curve fitting on each pixel of image stack

Before realizing curve fitting, one last operation is applied: the outlier detection. Various algorithms are tested, such as Hampel filter, multivariate analysis based on Mahalanobis distance, and mean filter. Due to the fact that blended three-year data contain higher fluctuations than that of a single standard year, a loose filter is selected to avoid marking correct data as the outlier. In this respect, a mean filter is adopted to eliminate just extremely divergent points.

In the beginning, the behavior of the wetland is modeled using a fourth-order polynomial with two constraints. For this implementation, Gauss-Markov Model with constraints method is adopted (Koch, 1999). In Gauss-Markov Model, the functional and stochastic models are written as:

$$\begin{aligned} y + e &= X\beta \\ D(y) &= \sigma^2 P^{-1} \end{aligned} \quad (4.2)$$

where  $y$ ,  $e$ ,  $X$ , and  $\beta$  are observations, observational residuals, coefficient (sensitivity/design) matrix, and parameters, respectively.  $D(y)$  is the covariance

matrix of  $y$  with an unknown variance factor  $\sigma^2$  and known weights  $P$ . The method aims to minimize the observational residuals in the least squares sense, which is obtained through the following equation:

$$e^T P e = \min \quad (4.3)$$

Using matrix algebra, the best linear unbiased estimator of the parameters  $\hat{\beta}$  and its covariance matrix  $D(\hat{\beta})$  are given as:

$$\begin{aligned} \hat{\beta} &= (X^T P X)^{-1} X^T P y \\ D(\hat{\beta}) &= \sigma^2 (X^T P X)^{-1} \end{aligned} \quad (4.4)$$

In the case of constraints,  $H\beta = w$  condition is introduced, where  $H$  is known coefficients and  $w$  is their known corresponding vector. The best linear unbiased estimator of the parameters  $\tilde{\beta}$  and its covariance matrix  $D(\tilde{\beta})$  in the Gauss-Markov Model with constraints are then given as:

$$\begin{aligned} \tilde{\beta} &= (X^T X)^{-1} [X^T y + H^T (H(X^T X)^{-1} H^T)^{-1} (w - H(X^T X)^{-1} X^T y)] \\ D(\tilde{\beta}) &= \sigma^2 [(X^T X)^{-1} - (X^T X)^{-1} H^T (H(X^T X)^{-1} H^T)^{-1} H(X^T X)^{-1}] \end{aligned} \quad (4.5)$$

To represent this minimization problem in matrix form, a vector including Lagrange multipliers ( $k$ ) has to be included. If necessary relations are established, normal equations for the best unbiased estimator of the parameters  $\tilde{\beta}$  and the vector, including multipliers  $k$  are given as:

$$\begin{bmatrix} X^T X & H^T \\ H & 0 \end{bmatrix} \begin{bmatrix} \tilde{\beta} \\ k \end{bmatrix} = \begin{bmatrix} X^T y \\ w \end{bmatrix} \quad (4.6)$$

Eventually, both Equations (4.5) and (4.6) give identical estimators for the parameters.

In this study, the introduced constraints are:

$$\begin{aligned} f(1) &= f(365) \\ f'(1) &= -f'(365) \end{aligned} \tag{4.7}$$

first of which enables the start and end values to be equal. The second one assigns the negative slope of starting point to the end point of the curve to allow a proper continuation.

The second implementation is based on the double-sigmoid function, which is derived from:

$$f(x) = \frac{L}{1 + e^{-\gamma(x-x_0)}} \tag{4.8}$$

where  $L$ ,  $\gamma$ , and  $x_0$  denote the curve's maximum value, growth rate, and  $x$  value at the midpoint, respectively. In this implementation, one of the two sides is formed from the beginning to the pick point of observations. The double-side is obtained via reversing the first function and integrating it through the rest of the functional values. The estimation is done using the Interior-Point algorithm mentioned in Section 4.5. Initial values are extracted from the TCWI image stack, which are the minimum TCWI value, maximum TCWI value, and its corresponding Day of Year (DoY) value.

Once the regression is completed and TCWI values of each pixel are estimated for the calendar year, it is possible to determine areas above a certain wetness level for a certain period using an appropriate query containing relevant thresholds. In this study, the query is formed to identify areas whose TCWI values are larger than -0.1 over 120 days. In other words, regions that are wet for one-third of a year are determined. The final extent is derived by applying morphological operators to the intersection of thresholded high resolution DTM and queried TCWI data.



#### 4.4 Classification Ontology

The flowchart of Sections 4.4, 4.5, 4.6 is given in Figure 4.5.

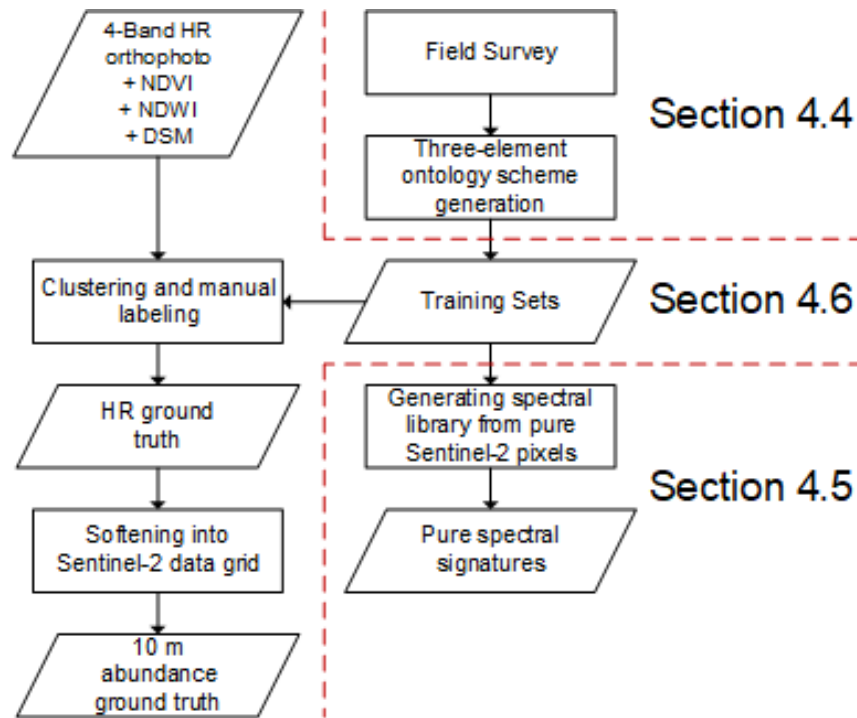


Figure 4.5 Flowchart of Sections 4.4, 4.5, and 4.6

The choice of the classes is critical for the success of any classification and the usefulness of the results. A systematic approach is adopted based on vegetation, soil, and water cycle. In this context, three site visits were carried out in December 2019, August 2020, and July 2021. During these visits, many samples were collected, and different classes were geographically marked on the field. In order to determine soil types and their behavior, soil analysis was performed by a professional laboratory. Various combinations of image clustering are utilized to distinguish classes spectrally and correlate with field observations (Figure 4.6).

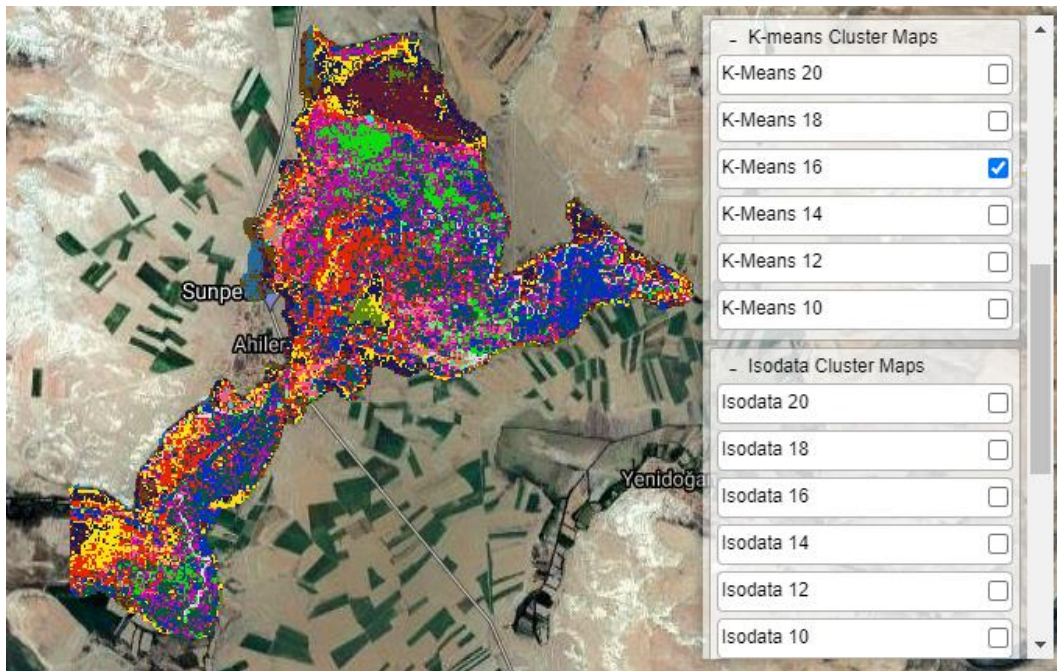


Figure 4.6 Clustering trials

In the beginning, the land cover is categorized into seven groups that are algal bloom, burned vegetation, mud, steppe, rushes, reed, and water regarding the 2019 site visit. The supervised classification trials start accordingly. The number of classes is increased with respect to the quality results. Besides, the second and third site visits fulfilled later on help collect more information and differentiate classes better. The classes are continuously re-organized, and training polygons are modified. In addition, statistical enhancements, such as creating sub-classes from pre-determined common categories separately by applying 2-means unsupervised classification, help formalize the ontology and reach the final types. In the end, nine classes characterizing the wetland cover are determined, which ensures the best representation. The reference polygons are derived accordingly. The resulting ontology is shown in Table 4.1. This three-element approach provides a common basis for wetland ontologies.

Table 4.1 Three-element ontology

No	Class Name	Hydrology	Vegetation	Soil
1	Gypsum	Saturated soil during the hot season, very shallow water during winter	Clusters of <i>Salicornia europea</i> and <i>Salicornia prostrata</i> (glasswort), small tufts of <i>Distichlis spicata</i> (inland saltgrass)	Surface: strong alkali, very salty, limy, medium organic substance, silty loam textured  Underlayer: strong alkali, very salty, very limy, high organic substance, clay textured
2	Juncus	No water cover or occasional water during winter	Juncus with 30% – 80% coverage / rest is same as the class “Pasture”	Same as the class “Steppe”
3	Pasture	0 – 2 m above the winter water level	Short green grass throughout the year	Same as the class “Steppe”
4	Phragmites	Water during winter	Dense <i>Phragmites australis</i> (common reed)	Not visible
5	Ranunculus	Water cover all year, slow flow	<i>Ranunculus trichophyllus</i> (threadleaf crowfoot)	Not visible

Table 4.1 Three-element ontology (continued)

No	Class Name	Hydrology	Vegetation	Soil
6	Shallow Water	Water cover during December – March interval	No vegetation or ignorable vegetation	Same as the class “Gypsum”
7	Steppe	2+ m above the winter level / no water cover	Partial green grass during January – April interval	Weak alkali, not salty, very limy, high organic substance and silty clay loam textured
8	Typha	Tendency for longer duration under water in comparison to Phragmites	Typha angustifolia (narrowleaf cattail) and Typha latifolia (broadleaf cattail)	Not visible
9	Water	Permanent water, increase in phytoplankton during the warm season	No vegetation	Not visible

The illustrations for the given classification ontology are shown in Figure 4.7.



Figure 4.7 Illustrations for given classification ontology ① Gypsum ② Juncus ③ Pasture ④ Phragmites ⑤ Ranunculus ⑥ Shallow Water ⑦ Steppe ⑧ Typha ⑨ Water

## 4.5 Spectral Library Generation from Pure Pixels

To be able to find out class distributions inside a coarse pixel via spectral unmixing explained in Section 4.7, spectra of the classes are required. The critical point is to extract spectrum values from the pixels, perfectly characterizing the category. In other words, the pixel content should not be mixed, thereby guaranteeing the representation of the exact member. This concept is known as pure pixel or pure spectral signature. In order to ensure extracting pure spectral signatures of the final classes (named as endmembers in spectral unmixing), the following procedure is carried out:

1. Intersecting each training polygon with the Sentinel-2 grid
2. Calculating the area of each partition
3. Assigning the value to the corresponding Sentinel-2 cell
4. Removing the cells whose calculated area stay below the threshold
5. Grouping the remaining cells according to the class information
6. Extracting the mean reflectance values from the Sentinel-2 image for the grouped class polygons

The procedure is illustrated in Figure 4.8.

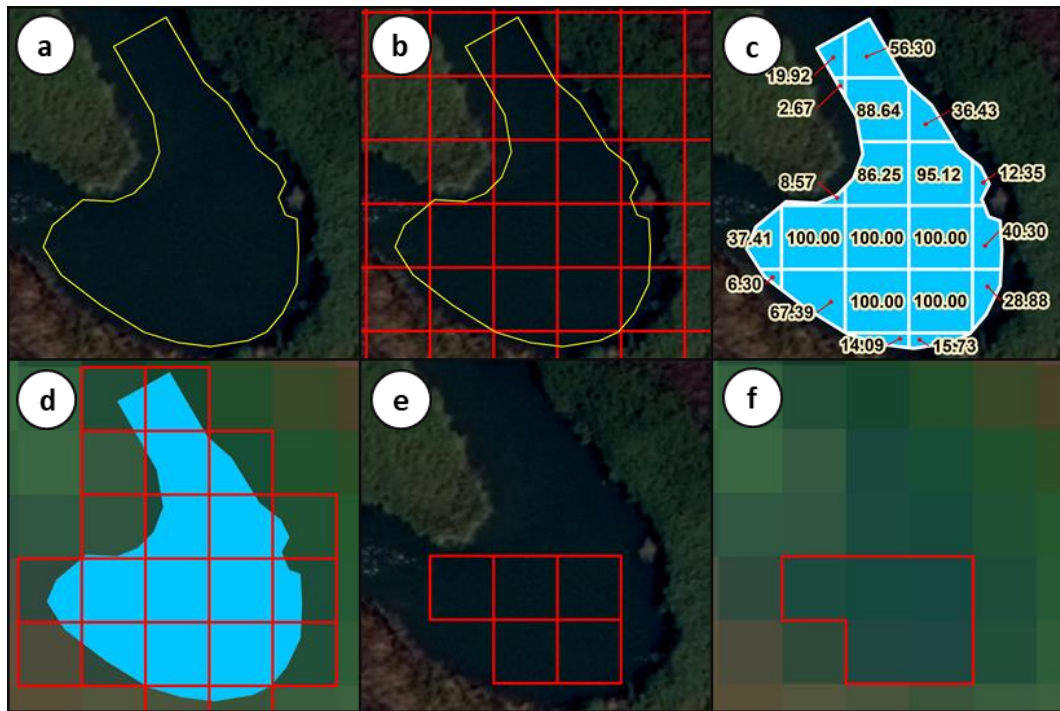


Figure 4.8 Spectral library generation from pure pixels (a) Training polygon (b) Step-1 (c) Step-2 (d) Step-3 (e) Step-4 (f) Steps-5&6

#### 4.6 Generation of Ground Truth for Abundances

The generation of ground truth relies on the RF supervised classification algorithm of the 4-band high resolution orthophoto. After finalizing the classes under the light of the three-element ontology approach, manually labeled training sets are polygonized on the orthophoto. Before moving onto the RF classification, the reference data is augmented with two indices and surface elevation. In addition to the existing R/G/B/NIR bands, NDVI, NDWI, and DSM bands are appended to the data to increase the classification accuracy. All three additional bands are rescaled to [0, 255] intervals in line with the radiometry of the orthophoto. In order to reduce variability, the model is trained through the 5-fold cross-validation technique.

The second step is to convert the classified image into an abundance map at 10 m resolution. In other words, the reference hard classification is softened into the

Sentinel-2 grid. This operation requires the calculation of class ratios for each corresponding cell of the test image to be unmixed. When the spatial resolutions of reference (30 cm/pixel) and test data (10 m/pixel) are taken into consideration, one test cell contains approximately 1,100 reference pixels. In view of the fact that test pixel size is not a multiple of reference pixel size, the classified reference image is converted to vector format and intersected with the test data grid to get exact abundance values. Then, quantities of classes (abundances) in each satellite grid are calculated considering the overlapping partitions. Since this process requires various operations, a model is created on model builder through the following steps:

1. Classifying the orthophoto using RF algorithm
2. Converting raster classes into vector polygons
3. Intersecting each class polygon with the Sentinel-2 grid
4. Calculating areas of outputs
5. Dissolving intersection polygons in corresponding Sentinel-2 pixel
6. Adding the abundance field and converting the calculations into the unit interval  $([0, 1])$
7. Joining the abundance field with the Sentinel-2 grid
8. Exporting each class grid as a single band raster

The outputs of the algorithm are given in Figure 4.9.



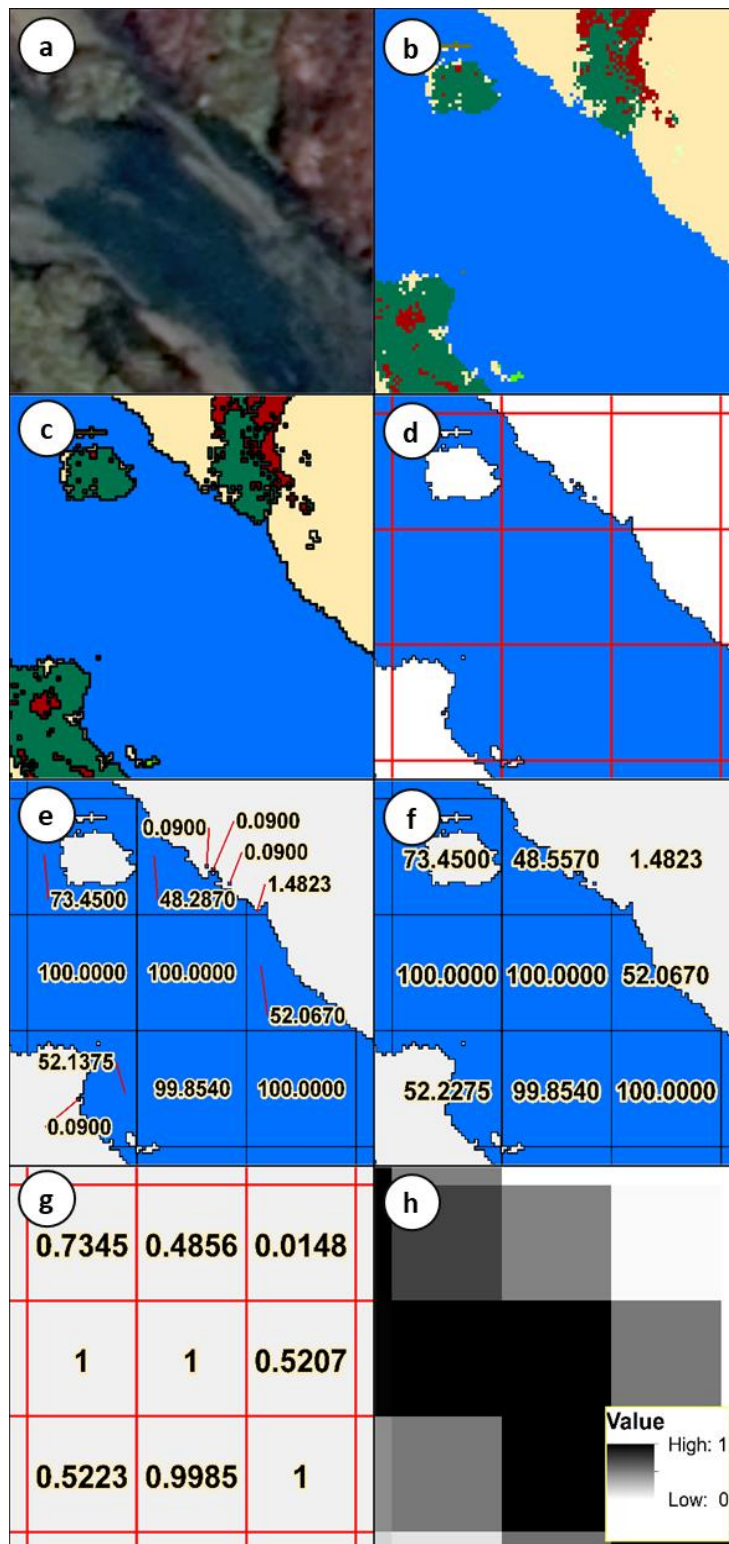


Figure 4.9 Illustrations of outputs after each step (a) Orthophoto (b) Step-1 (c) Step-2 (d) Step-3 (e) Step-4 (f) Step-5 (g) Steps-6&7 (h) Step-8

## 4.7 Spectral Unmixing of Multispectral Images

The flowchart of Sections 4.7, 4.8, and 4.9 is given in Figure 4.10.

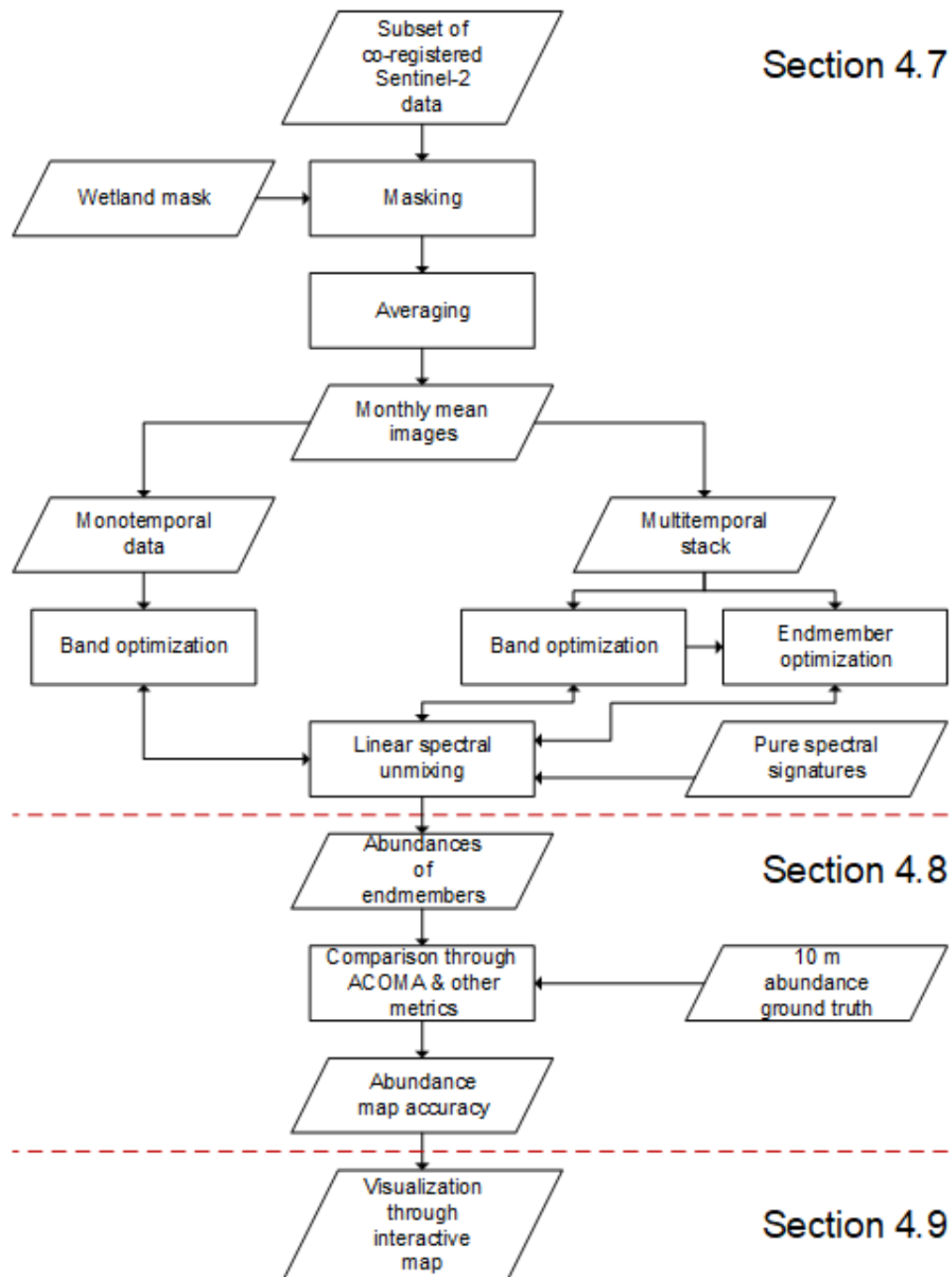


Figure 4.10 Flowchart of Sections 4.7, 4.8, and 4.9

One of the primary purposes of this study is to estimate the abundance values of major classes within each pixel. In other words, soft classification is intended rather than hard classification. The reason behind tackling the problem in this way is that the spatial resolution of the sensor is not high enough to separate different elements, and they occupy a single-pixel jointly in return. Therefore, spectral unmixing is adopted in this study.

The two main options for spectral unmixing are linear and nonlinear models. Most of the unmixing algorithms assume that the measured spectrum of a mixed pixel is the linear combination of the spectral signatures of existing elements. This approach is known as the Linear Mixture Model, which neglects the multiple scattering effects in the data acquisition. On the other hand, nonlinear models take the secondary reflections or intimate mixtures into account. They can be mainly grouped as the Bilinear Mixture Model and Intimate Mixture Model. The Bilinear Mixture Model considers the interactions between only two elements in addition to their individual contributions. In the case of the Intimate Mixture Model, several elements contribute to the measured spectrum of the pixel (Dobigeon et al., 2016). Figure 4.11 illustrates the types of mixture models.

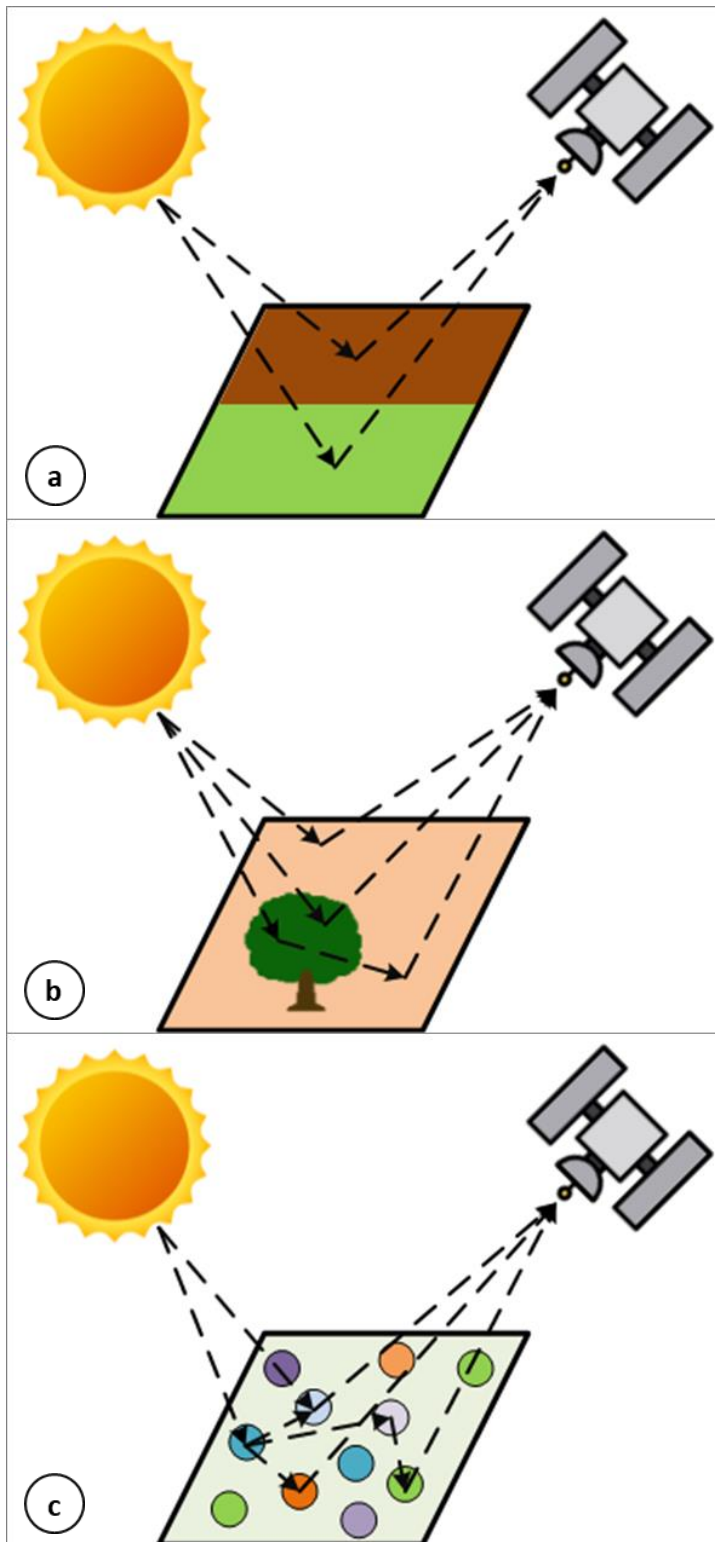


Figure 4.11 Illustrations for mixture models (a) Linear Mixture Model (b) Bilinear Mixture Model (c) Intimate Mixture Model

The Linear Mixture Model forms the basis of the operations performed in this study. For each pixel, it can be formulated as follows:

$$r_i = \sum_{j=1}^q m_{ij} \alpha_j + n_i \quad (4.9)$$

where  $r_i$  is the measured reflectance value at spectral band  $i$ ,  $m_{ij}$  is the reflectance of the  $j$ -th endmember at spectral band  $i$ ,  $\alpha_j$  is the fractional abundance of the  $j$ -th endmember, and  $n_i$  is the residual for the spectral band  $i$ .

Considering the data to be unmixed have  $b$  bands, Equation (4.9) can be reformulated in compact matrix form as:

$$r = M\alpha + n \quad (4.10)$$

where  $r$  is a  $b \times 1$  vector containing the observed spectrum of the pixel,  $M$  is a  $b \times q$  matrix containing  $q$  endmembers (pure spectral signatures),  $\alpha$  is a  $q \times 1$  vector containing the fractional abundances of the endmembers, and  $n$  is a  $b \times 1$  vector containing the residuals affecting the observations at each spectra band.

To be able to reflect consistency with reality, two constraints are introduced that are abundance non-negativity, represented as:

$$\alpha_i \geq 0 \quad (i = 1, \dots, q) \quad (4.11)$$

or in compact form by:

$$\alpha \geq 0 \quad (4.12)$$

and abundance sum-to-one, represented as:

$$\sum_{i=1}^q \alpha_i = 1 \quad (4.13)$$

or in compact form by:

$$1_q \alpha = 1 \quad (4.14)$$

where  $1_q$  is a  $1 \times q$  vector containing ones.

In this task, the contributions come from the optimization of band weights and endmember spectra in order to derive closer agreement with reality and hence higher accuracy. Therefore, prior to the Constrained Linear Least Squares solution, band weights are optimized through the Interior Point Algorithm (Byrd et al., 1999), which follows a barrier approach incorporating Sequential Quadratic Programming (Nocedal and Wright, 2006) and Trust Region techniques (Moré and Sorensen, 1983) to solve the issues occurring in the iteration. The Interior Point approach to constrained minimization solves a sequence of approximate minimization problems, in which the problem is given as:

$$\begin{aligned} & \min_x f(x) \\ & \text{subject to } g(x) \leq 0 \text{ and } h(x) = 0 \end{aligned} \quad (4.15)$$

where  $g(x)$  and  $h(x)$  are constraint functions.

For each barrier parameter  $\mu > 0$ , the approximate problem is written as:

$$\begin{aligned} & \min_{x,s} f_\mu(x, s) = \min_{x,s} f(x) - \mu \sum_i \ln(s_i) \\ & \text{subject to } s \geq 0, h(x) = 0 \text{ and } g(x) + s = 0 \end{aligned} \quad (4.16)$$

where  $s$  is the slack parameter. As  $\mu$  decreases to zero, the minimum of  $f_\mu$  should approach the minimum of  $f$ ; in other words, the sequence of solutions to Equation (4.16) should converge to a stationary point. The algorithm uses either a direct step, also known as the Newton step or a conjugate gradient step at each iteration to solve the approximation problem.

Two constraints are introduced before the optimization takes place. One of them is setting a lower bound for band weights, which is logically greater than or equal to zero. The second one is fixing one of the band weights to a stationary value in order to constitute a reference point, which is chosen to be the NIR band's weight equals to one due to its higher brightness. The last operation is the calculation of the error function. This is performed by calculating squared residual based on overall accuracy at each iteration. The computation of overall accuracy is achieved using the Abundance Confusion Matrix (ACOMA), explained in the next section.

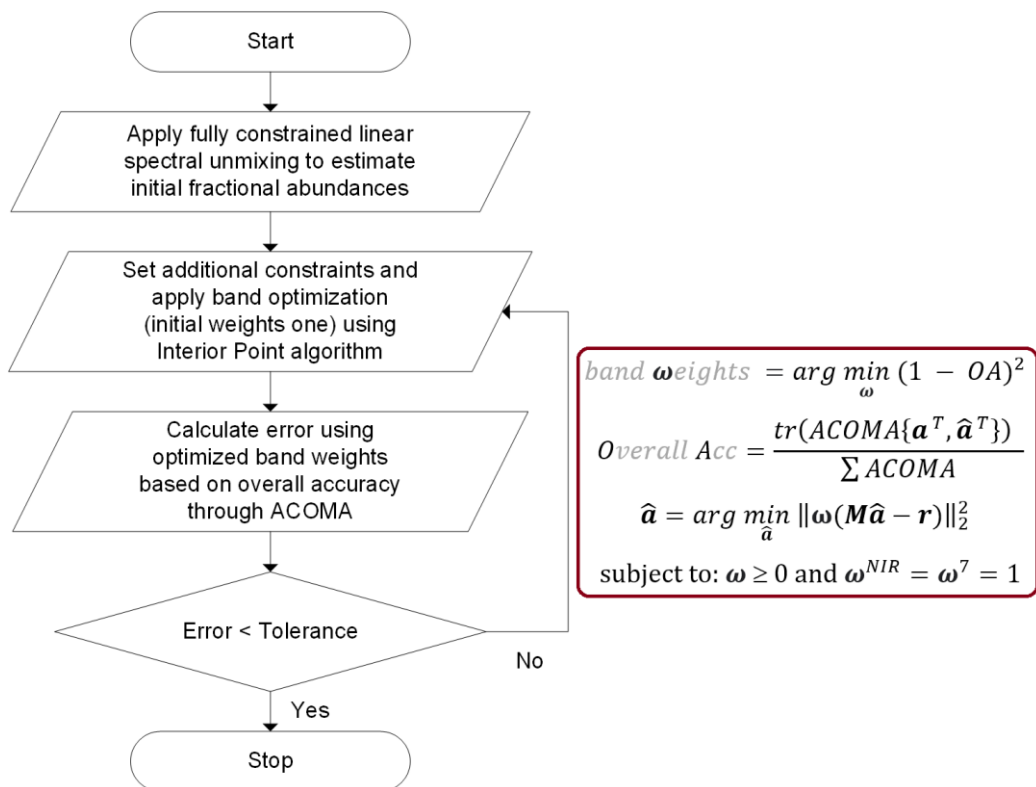


Figure 4.12 Flowchart of band optimization process

After the band weights are optimized, the endmember spectra are optimized with original and optimized band weights using Interior Point Algorithm as well in an effort to minimize reconstruction error. The reconstruction image is obtained by multiplying the reference abundances and optimized endmember spectra at each iteration. No constraint is introduced in this implementation. Figure 4.13 shows an example of the original image and its corresponding reconstruction.

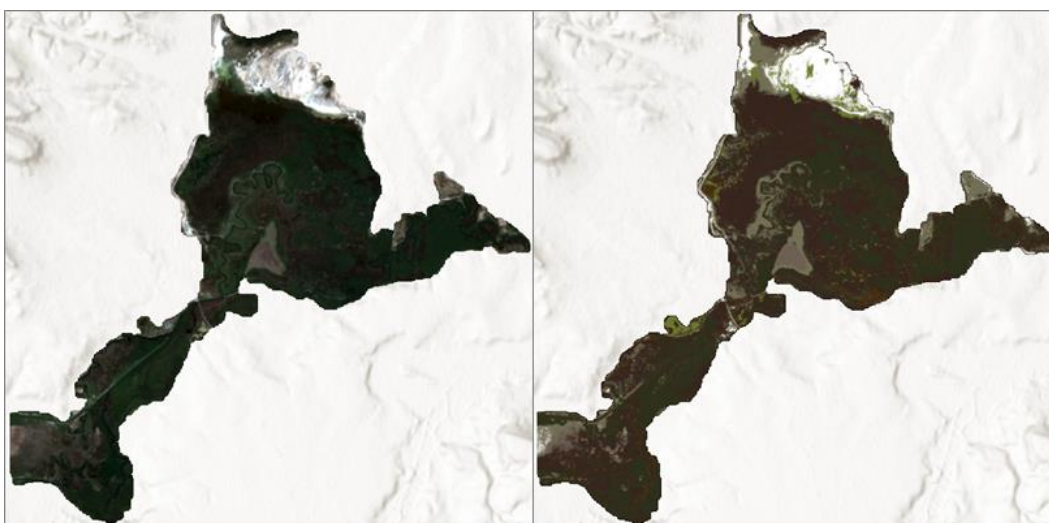


Figure 4.13 Example of original (left) vs. reconstructed (right) RGB images

#### 4.8 Performance Assessment

The performance assessment of the wetland extent determination is carried out using the metrics given in Table 4.2.

Table 4.2 Performance metrics for evaluating wetland extent determination

<b>Frame Area (FA)</b>	Extracted from the map
<b>Manually Marked Area (MMA)</b>	Extracted from the map
<b>Predicted Area (PA)</b>	Extracted from the map



Table 4.2 Performance metrics for evaluating wetland extent determination (continued)

<b>Union of MMA and PA</b>	$MMA \cup PA$
<b>True Positive Area (TPA)</b>	$MMA \cap PA$
<b>True Negative Area (TNA)</b>	$FA \setminus (MMA \cup PA)$
<b>False Positive Area (FPA)</b>	$PA \setminus (MMA \cap PA)$
<b>False Negative Area (FNA)</b>	$MMA \setminus (MMA \cap PA)$
<b>Sensitivity/Recall (True Positive Rate)</b>	$\frac{TPA}{TPA + FNA}$
<b>Specificity/Selectivity (True Negative Rate)</b>	$\frac{TNA}{TNA + FPA}$
<b>Precision (Positive Predictive Value)</b>	$\frac{TPA}{TPA + FPA}$
<b>Negative Predictive Value</b>	$\frac{TNA}{TNA + FNA}$
<b>Miss Rate (False Negative Rate)</b>	$\frac{FNA}{FNA + TPA}$
<b>Fall-out (False Positive Rate)</b>	$\frac{FPA}{FPA + TNA}$
<b>False Discovery Rate</b>	$\frac{FPA}{FPA + TPA}$
<b>False Omission Rate</b>	$\frac{FNA}{FNA + TNA}$
<b>Overall Accuracy</b>	$\frac{TPA + TNA}{TPA + TNA + FPA + FNA}$
<b>F<sub>1</sub> Score</b>	$\frac{2TPA}{2TPA + FPA + FNA}$

The classification performance for the high resolution orthophoto is assessed by the calculation of the standard confusion matrix indicating the producer's and user's accuracies, together with the omission and commission errors. Additionally, overall accuracy ( $OA$ ), kappa statistic ( $\kappa$ ), and coefficient of determination ( $R^2$ ) are computed.

The overall accuracy ( $OA$ ) is calculated through Confusion Matrix as follows:

$$OA = \frac{CCS}{RS} \quad (4.17)$$

where  $CCS$  is the correctly classified sites, and  $RS$  is the total number of reference sites.

The kappa statistic ( $\kappa$ ), which is widely used to measure the classifier performance, is calculated as follows:

$$\kappa = \frac{p_0 - p_e}{1 - p_e} \quad (4.18)$$

where  $p_0$  is the probability of correct classification, and  $p_e$  is the probability of chance agreement.

The coefficient of determination ( $R^2$ ), which is a measure of how well observations are estimated by the model based on the proportion of total variation of estimations, is calculated as follows:

$$R^2 = 1 - \frac{SS_{res}}{SS_{tot}} \quad (4.19)$$

where  $SS_{res}$  is the sum of squares of residuals, and  $SS_{tot}$  is the total sum of squares.

Two new metrics are introduced for the assessment of abundances obtained via spectral unmixing.

The proposed abundance performance metric (*apm*), indicating the rate at which the maximum abundance value of each pixel belongs to the same endmember both in reference and unmixed data, is defined as:

$$apm = \frac{card(A)}{h \times w} \quad (4.20)$$

where  $A$  is the set of consistent abundance elements that have the characteristic mentioned above, whereas  $h$  and  $w$  are the height and width of the unmixed data. The algorithm for the calculation of  $A$  is given in Algorithm 1.

---

Algorithm 1

---

```

1. start
2. read reference_abun $h \times w \times b$ , unmixed_abun $h \times w \times b$ 
3.  $A = 0$ 
4. for  $i = 1 : (h \times w)$ 
5.   [val1, idx1] = max (reference_abun $i$ );
6.   [val2, idx2] = max (unmixed_abun $i$ );
7.   if idx1 == idx2;
8.      $A += 1$ ;
9.   end if
10. end for
11. stop

```

---

Below is a simple example of how the metric works at a two-pixel sample.

Height	Reference		Target	
	Width		Width	
	Pixel-1	Pixel-2	Pixel-1	Pixel-2
Class 1 - Gypsum	0.00	0.00	0.05	0.05
Class 2 - Juncus	0.05	0.10	0.00	0.00
Class 3 - Pasture	0.05	0.00	0.20	0.10
Class 4 - Phragmites	0.10	0.00	0.10	0.45
Class 5 - Ranunculus	0.40	0.10	0.35	0.15
Class 6 - Shallow W.	0.05	0.05	0.00	0.00
Class 7 - Steppe	0.15	0.05	0.00	0.00
Class 8 - Typha	0.00	0.60	0.20	0.15
Class 9 - Water	0.20	0.10	0.10	0.10
	1.00	1.00	1.00	1.00

This example states that there are two 1 x 2 images to be compared. The cardinality value is one because only the first pixel has the highest abundance for the same class (band) in both reference and target images. Then, the solution is computed using the given formula:

$$apm = \frac{card(A)}{(h \times w)} = \frac{1}{(1 \times 2)} = 0.50 = 50\%$$

The interpretation of this result is that half of the total number of pixels have an agreement in terms of possessing the highest abundance for the same class.

All these metrics give an idea about the overall performance; however, there is still a need for a technique showing class-level performances like the standard confusion matrix.

Various approaches have been proposed for assessing soft/fuzzy classification results in the literature. Early practices tended to either harden the soft classification outputs or focus just on pure pixels in order to apply traditional accuracy metrics. As

expected, the results were not very liable due to information loss (Foody and Trodd, 1993; Wang, 1990). Another study conducted by Foody (1996) suggested using measures of closeness through distance metrics and probability distributions. Binaghi et al. (1999) proposed a method quantifying the index of fuzziness (IF) based on Hamming distance of reference and target fuzzy sets. This method was improved by Stehman et al. (2007) in terms of precision and standard errors of the less common classes, utilizing stratified random sampling estimators. Using a generalized area-based error matrix introduced by Lewis and Brown (2001), relative errors were derived together with the overall and class-based proportions of the area in error. Silván-Cárdenas and Wang (2008) proposed a new technique, the sub-pixel confusion-uncertainty matrix, indicating the confusion intervals through the magnitude of maximum error around the center value. A software tool named Soft Classification Accuracy Assessment using SCM, FERM, Entropy, and RMSE (SCAASFER) was developed that makes the use of the techniques mentioned above (Khangarot et al., 2016). In addition to matrices, a metric like overall accuracy and kappa, namely the correctness coefficient involving the generation of the binary map for each class from ground truth, was introduced by Emami and Mojaradi (2009).

This study proposes a new approach, namely Abundance Confusion Matrix (ACOMA), which considers the issue from a slightly different perspective. It is also the adaptation of the confusion matrix, providing the accuracy of fractional compatibility.

The main contribution provided by ACOMA is the determination of area allocation for a single pixel through regression when there are infinite solutions. If the number of classes is  $N$ , the method takes reference abundances,  $a_{ik}$ , and estimated abundances,  $\hat{a}_{ik}$ , where  $i$  denotes the class number ( $\in \{1, 2, \dots, N\}$ ) and  $k$  denotes the pixel number. The method calculates an error matrix from whom the omission and commission errors, together with overall accuracy and kappa statistic, can be derived. It allows for assessing the partial agreement for each element rather than one-to-one matching. The entries of the ACOMA,  $c_{ij}$ , are defined as “the actual

abundance of class  $i$  which is attributed to class  $j$ ” on average. Firstly, the abundance confusion matrix for a single pixel,  $C_k$ , is calculated. The diagonal elements can easily be found as  $c_{ii,k} = \min(a_{ik}, \hat{a}_{ik})$ . For the rest of the matrix, there are the following constraints:

$$a_{ik} = \sum_j c_{ij,k}, \quad \hat{a}_{ik} = \sum_j c_{ji,k} \quad \text{and} \quad c_{ij,k} \geq 0 \quad (4.21)$$

Because of the constraints, if  $a_{ik} < \hat{a}_{ik}$ , all elements in the  $i$ -th column except the diagonal element are zero. Similarly, all elements in the  $j$ -th row except the diagonal element are zero if  $a_{ik} > \hat{a}_{ik}$ . For the remaining entries, a linear equation in the form of  $\mathbf{Ax} = \mathbf{b}$  can be constructed. However, matrix  $\mathbf{A}$  is rank deficient in most of the cases, especially if  $N$  is large. The problem can be solved by some sort of regularization like using a minimum norm constraint. Lawson-Hanson algorithm, LU decomposition, QR decomposition, singular value decomposition (SVD), orthogonal decomposition, Tikhonov regularization, and TNT-NN algorithm are tested to solve this problem. The first four methods do not provide uniform distribution of estimations in case of rank deficiency, whereas the last three methods do. Nevertheless, the fifth and sixth can produce negative outputs since they do not have a non-negativity constraint. Therefore, the TNT-NN is adopted, a fast active set method primarily developed to solve non-negative least squares problems (Myre et al., 2017). The approach also enables the balanced distribution of estimations in case of rank deficiency.

Once the pixel level abundance confusion matrix is calculated, the ACOMA is the sum of all pixel level matrices. That is:

$$\mathbf{C} = \sum_k \mathbf{C}_k \quad (4.22)$$

Below are two simple examples of how the metric works at the pixel level. Assuming the problem is given as:

	C1	C2	C3
<b>Known Abundance</b>	0.60	0.30	0.10
<b>Estimated Abundance</b>	0.50	0.20	0.30

The confusion matrix is quickly found to be:

Confusion Matrix	Estimated			
		0.50	0.00	<i>a</i>
Known	0.00	0.20	<i>b</i>	<b>0.30</b>
	0.00	0.00	0.10	<b>0.10</b>
	<b>0.50</b>	<b>0.20</b>	<b>0.30</b>	

Then, the solution is:

$$\begin{bmatrix} 1 & 0 \\ 0 & 1 \\ 1 & 1 \end{bmatrix} \begin{bmatrix} a \\ b \end{bmatrix} = \begin{bmatrix} 0.1 \\ 0.1 \\ 0.2 \end{bmatrix} \quad (4.23)$$

Since the rank of the matrix is two, the unique solution is  $a = b = 0.1$ . As a result, the Abundance Confusion Matrix (ACOMA) is:

		Overall Accuracy = 0.80				
True Class	C1	0.50	0.00	0.10	83.3%	16.7%
	C2	0.00	0.20	0.10	66.7%	33.3%
	C3	0.00	0.00	0.10	100.0%	
		100.0%	100.0%	33.3%		
			66.7%			
		C1	C2	C3	Predicted Class	

In the case of four classes, an example problem is given as:

	<b>C1</b>	<b>C2</b>	<b>C3</b>	<b>C4</b>
<b>Known Abundance</b>	0.50	0.20	0.20	0.10
<b>Estimated Abundance</b>	0.40	0.30	0.10	0.20

The confusion matrix is found to be:

<b>Confusion Matrix</b>	<b>Estimated</b>				
<b>Known</b>	0.40	<i>a</i>	0.00	<i>b</i>	<b>0.50</b>
	0.00	0.20	0.00	0.00	<b>0.20</b>
	0.00	<i>c</i>	0.10	<i>d</i>	<b>0.20</b>
	0.00	0.00	0.00	0.10	<b>0.10</b>
	<b>0.40</b>	<b>0.30</b>	<b>0.10</b>	<b>0.20</b>	

The equations can be written as:

$$\begin{aligned}
 a + b &= 0.10 \\
 c + d &= 0.10 \\
 a + c &= 0.10 \\
 b + d &= 0.10
 \end{aligned}
 \tag{4.24}$$

or in the compact matrix form as:

$$\begin{bmatrix} 1 & 1 & 0 & 0 \\ 0 & 0 & 1 & 1 \\ 1 & 0 & 1 & 0 \\ 0 & 1 & 0 & 1 \end{bmatrix} \begin{bmatrix} a \\ b \\ c \\ d \end{bmatrix} = \begin{bmatrix} 0.10 \\ 0.10 \\ 0.10 \\ 0.10 \end{bmatrix}
 \tag{4.25}$$



where determinant is zero, and there will be an infinite number of solutions. This issue can be solved by regularization. This is where the TNT-NN fast active set method steps in, as mentioned above. TNT-NN produces the following outputs:

$$\begin{aligned}
 a &= 0.0493 \\
 b &= 0.0507 \\
 c &= 0.0507 \\
 d &= 0.0493
 \end{aligned}
 \tag{4.26}$$

As a result, the Abundance Confusion Matrix (ACOMA) is:

		Overall Accuracy = 0.80					
True Class	C1	0.40	0.05	0.00	0.05	80.0%	20.0%
	C2	0.00	0.20	0.00	0.00	100.0%	
	C3	0.00	0.05	0.10	0.05	50.0%	50.0%
	C4	0.00	0.00	0.00	0.10	100.0%	
		100.0%	66.7%	100.0%	50.0%		
		33.3%		50.0%			
		C1	C2	C3	C4	Predicted Class	

#### 4.9 Visualization of Gathered and Generated Data

In this thesis, a dynamic web map containing all gathered and generated data is created for visualization purposes. There are numerous open-source and commercial mapping & data visualization libraries like Leaflet, OpenLayers, D3, MapBox GL JS, Kartography, Mango, GIS Cloud, Carto, Google Maps JavaScript API, and ArcGIS API for JavaScript. Leaflet, a lightweight, relatively simple, and flexible open-source JavaScript library for generating interactive maps, is utilized for the visualization task. JavaScript programming language is primarily used for defining

the interactive behavior of web pages by accessing and modifying the contents. Although the core library is tiny by design to avoid dependencies, there are dozens of ready-to-use plugins available for users to extend the functionality of web mapping applications. Hence, most of the necessary tools are already included in the extensive plugin library. Leaflet inherently supports Web Map Service (WMS) layers, GeoJSON layers, vector layers, and tile layers. Support for many other types of layers can be ensured via plugins. In the case of establishing a web server, it is possible to share interactive maps through the internet, which is the essential purpose of the platform. On the other hand, it can also be used as a desktop application just for personal use.

## CHAPTER 5

### RESULTS AND DISCUSSION

#### 5.1 Results

##### 5.1.1 Co-registration of Satellite Imagery

Two test data frames are co-registered to high resolution orthophoto to compare the algorithms. One frame is selected from close to the date of the master image, whereas the other is from a different season. The procedure is performed using the green bands of reference and target images. Table 5.1 shows the correlation coefficients for each algorithm.

Table 5.1 Correlation of coefficient values for each algorithm

Date of Reference	20.07.2019	
Date of Target	11.02.2019	31.07.2019
Metric	Correlation Coefficient	
Original	0.69	0.87
In-house routine	0.70	0.88
GeFolki	0.70	0.88
SNAP radar	0.70	0.88
AROSICS	0.70	0.88

All alternatives produce the same result in terms of correlation coefficients. Nevertheless, with its practical capabilities, such as ensuring tie point data export, including displacement vector information, and easy implementation of batch processing thanks to the Python environment, AROSICS is primarily adopted in this

thesis. Since the data to be co-registered are more than 100 frames, straightforward batch processing is a vital requirement. Moreover, the software supports cloud and shadow masking as well as three-step outlier detection using reliability, Mean Structural Similarity Index (MSSIM), and Random Sample Consensus (RANSAC) filtering techniques. Figure 5.1 shows one of the co-registered images with the collected tie points and their absolute shift values.

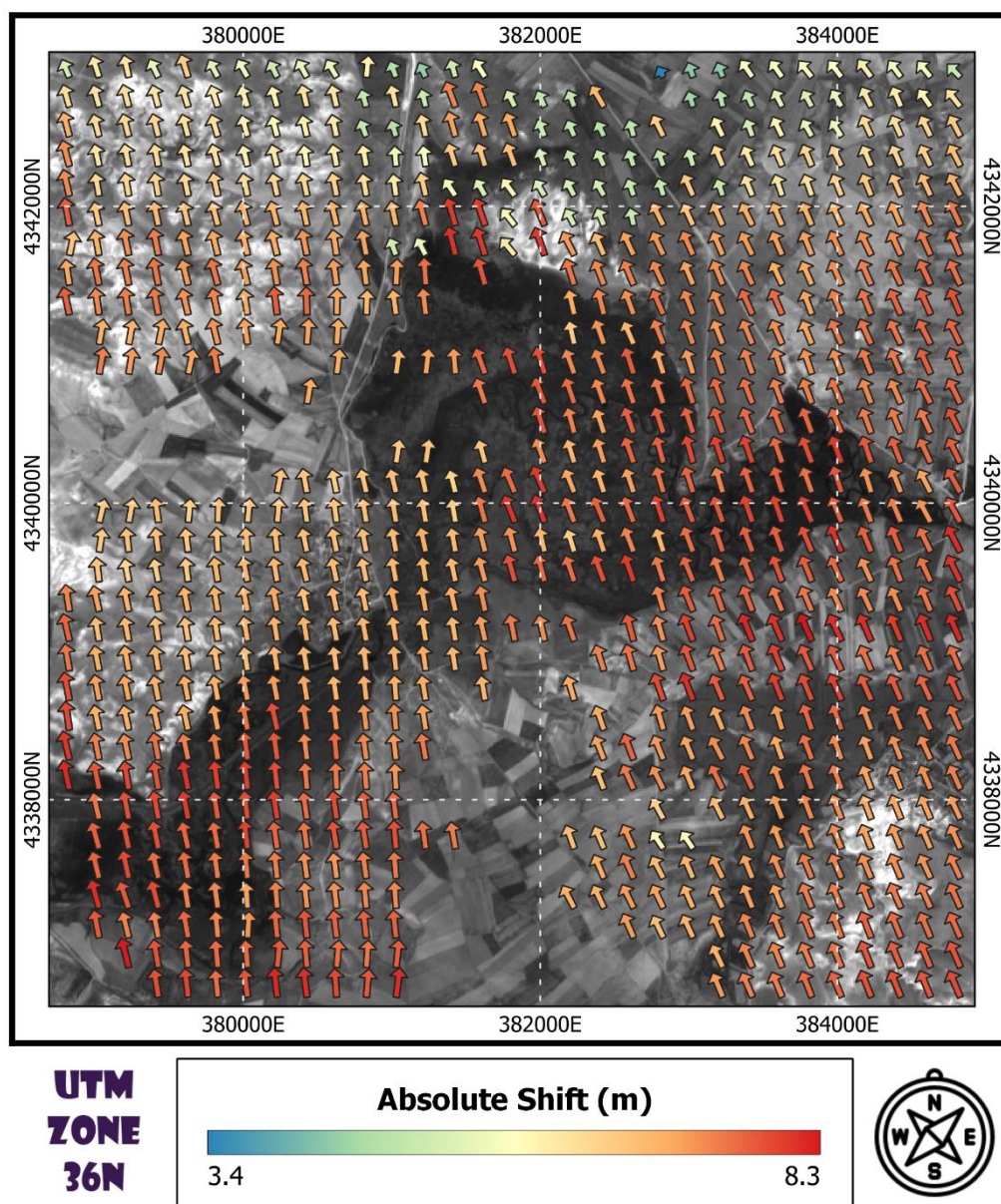


Figure 5.1 Absolute shift values of tie points for image dated 23.03.2019

### 5.1.2 Wetland Mask

With respect to the flowchart given in Figure 4.1, the first thresholding is applied to DTM for the extraction of rough boundaries. When the area is examined, the best elevation thresholding values appear to be 797 and 804 to describe the wetland bed. The thresholding procedure is tested using open-access DEM data as well. With this end in view, Advanced Land Observing Satellite (ALOS) HR Terrain Corrected DEM (12.5m), Copernicus EU-DEM v1.1 (25m), and Shuttle Radar Topography Mission (SRTM) Global v3.0 (~30m) data are examined. Reasonable wetland beds are obtained, as demonstrated in Figure 5.2.

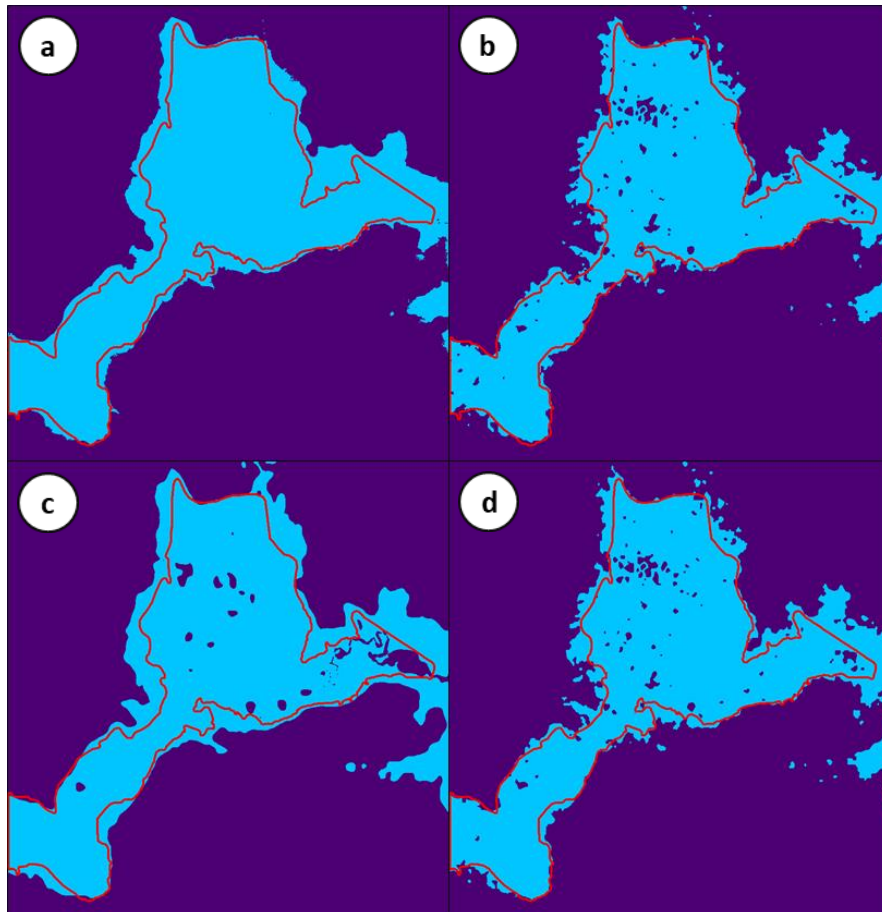


Figure 5.2 Comparison of different elevation models - Red polygon represents ground truth extent digitized manually from high resolution orthophoto (a) Aerial DTM (b) ALOS (c) Copernicus (d) SRTM

Meanwhile, fine adjustment is performed using 106 cloud and shadow-free co-registered images. The results of the fourth-order polynomial with two constraints can be seen in Figure 5.3, Figure 5.4, and Figure 5.5.

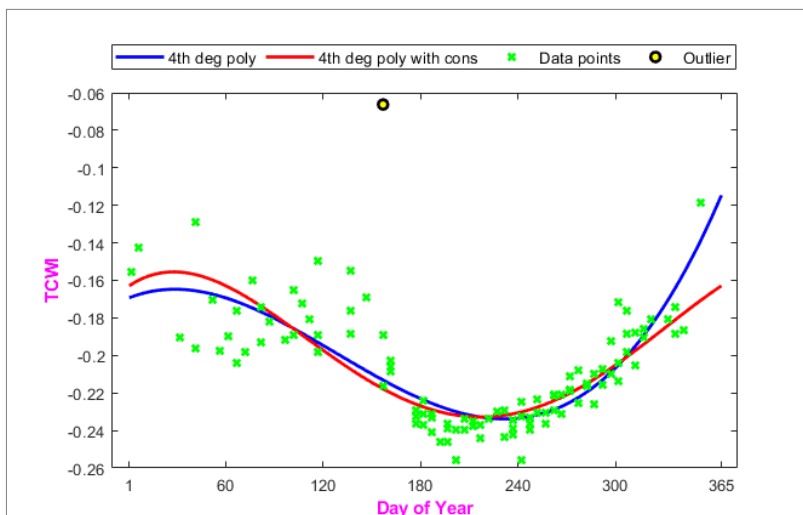


Figure 5.3 Example of fourth-order polynomial fitting on 106-band image stack

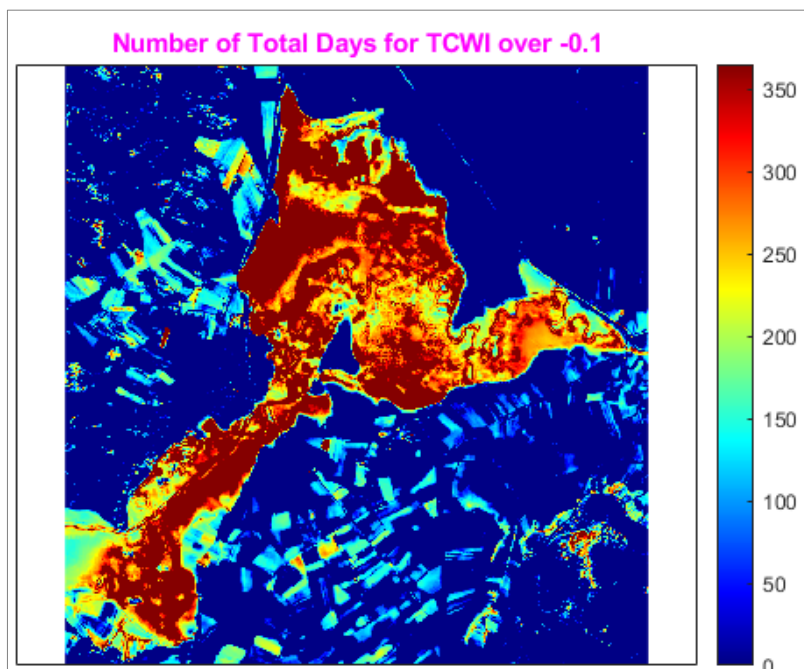


Figure 5.4 Total number of days having TCWI over -0.1 in a calendar year

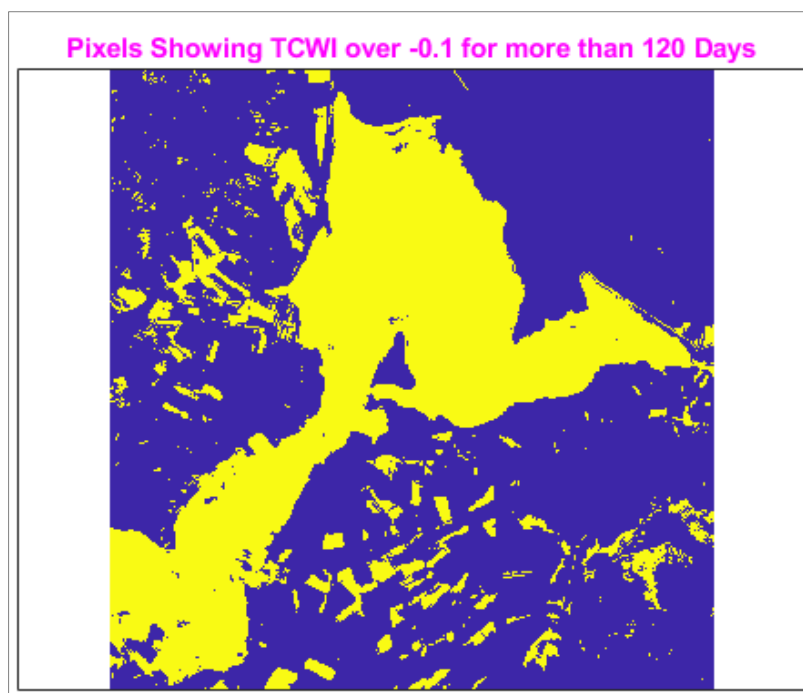


Figure 5.5 Locations having TCWI over -0.1 more than 120 days in a calendar year

The results of double-sigmoid optimization can be seen in Figure 5.6, Figure 5.7, and Figure 5.8.

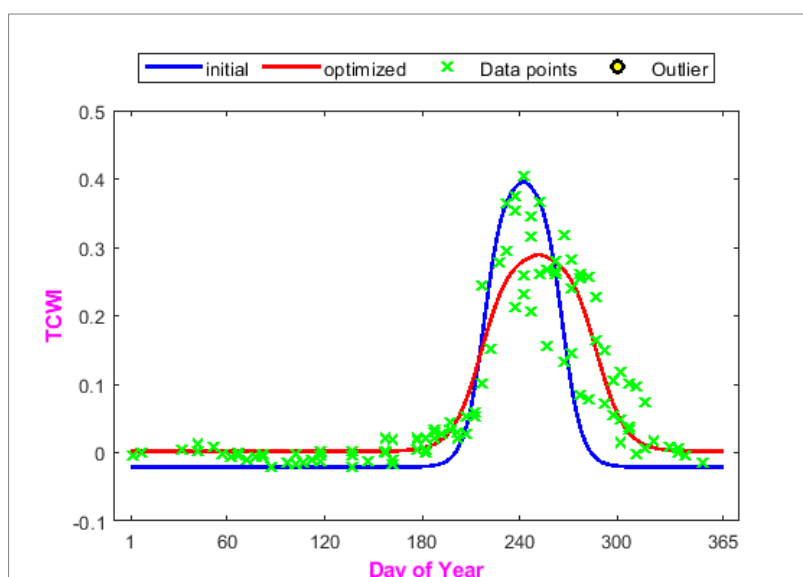


Figure 5.6 Example of double-sigmoid curve fitting on 106-band image stack

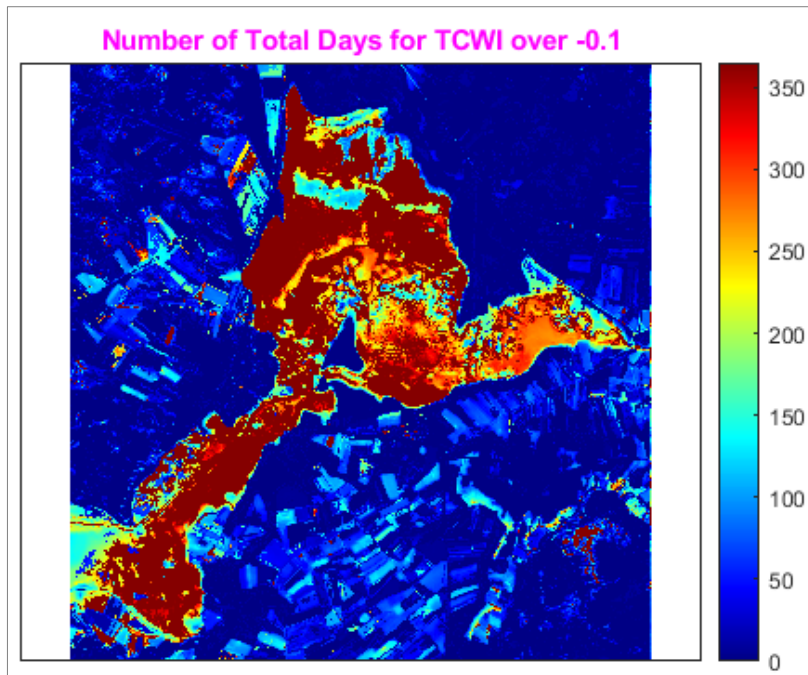


Figure 5.7 Total number of days having TCWI over -0.1 in a calendar year

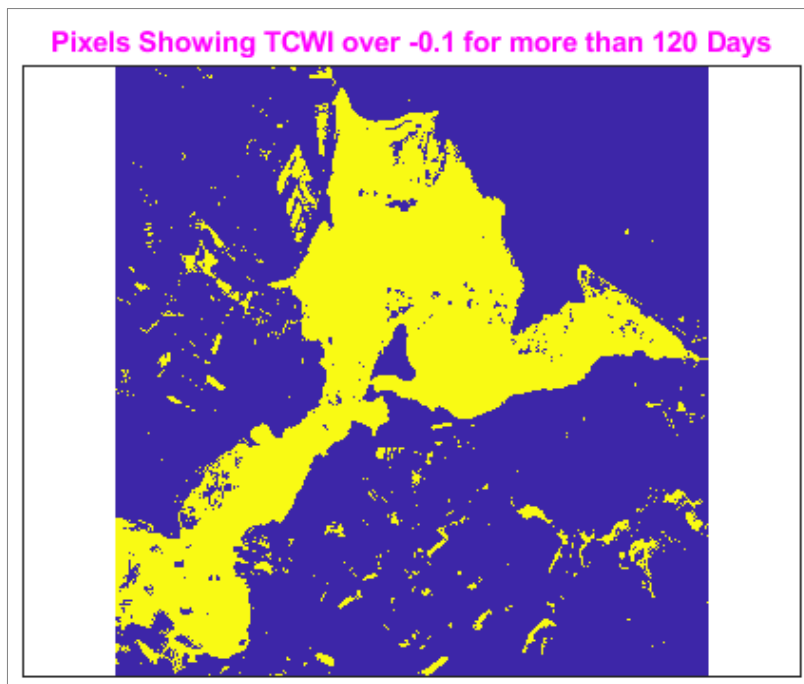


Figure 5.8 Locations having TCWI over -0.1 more than 120 days in a calendar year



Both of the methods provide satisfactory results in terms of accuracy (Table 5.2) and can be applied to other wetlands considering the inherent features. However, in this study, it is proceeded with the double-sigmoid fitting since it gives better results with regard to cleaning out agricultural fields.

Table 5.2 Standard deviations of fitting results

<b>Standard Deviation</b>	<b>Fourth-Order Polynomial with Two Constraints</b>		
	<b>All pixels</b>	<b>Outside ground truth extent</b>	<b>Inside ground truth extent</b>
<b>max</b>	0.1459	0.1459	0.1024
<b>min</b>	0.0066	0.0099	0.0066
<b>mean</b>	0.0395	0.0425	0.0297
<b>Standard Deviation</b>	<b>Double-Sigmoid Function</b>		
	<b>All pixels</b>	<b>Outside ground truth extent</b>	<b>Inside ground truth extent</b>
<b>max</b>	0.1461	0.1461	0.1331
<b>min</b>	0.0067	0.0090	0.0067
<b>mean</b>	0.0413	0.0446	0.0302

After intersecting this output with the thresholded DTM, small object removal, hole filling, and morphological opening operations are applied to obtain the final extent. The evolution of the mask is given in Figure 5.9.

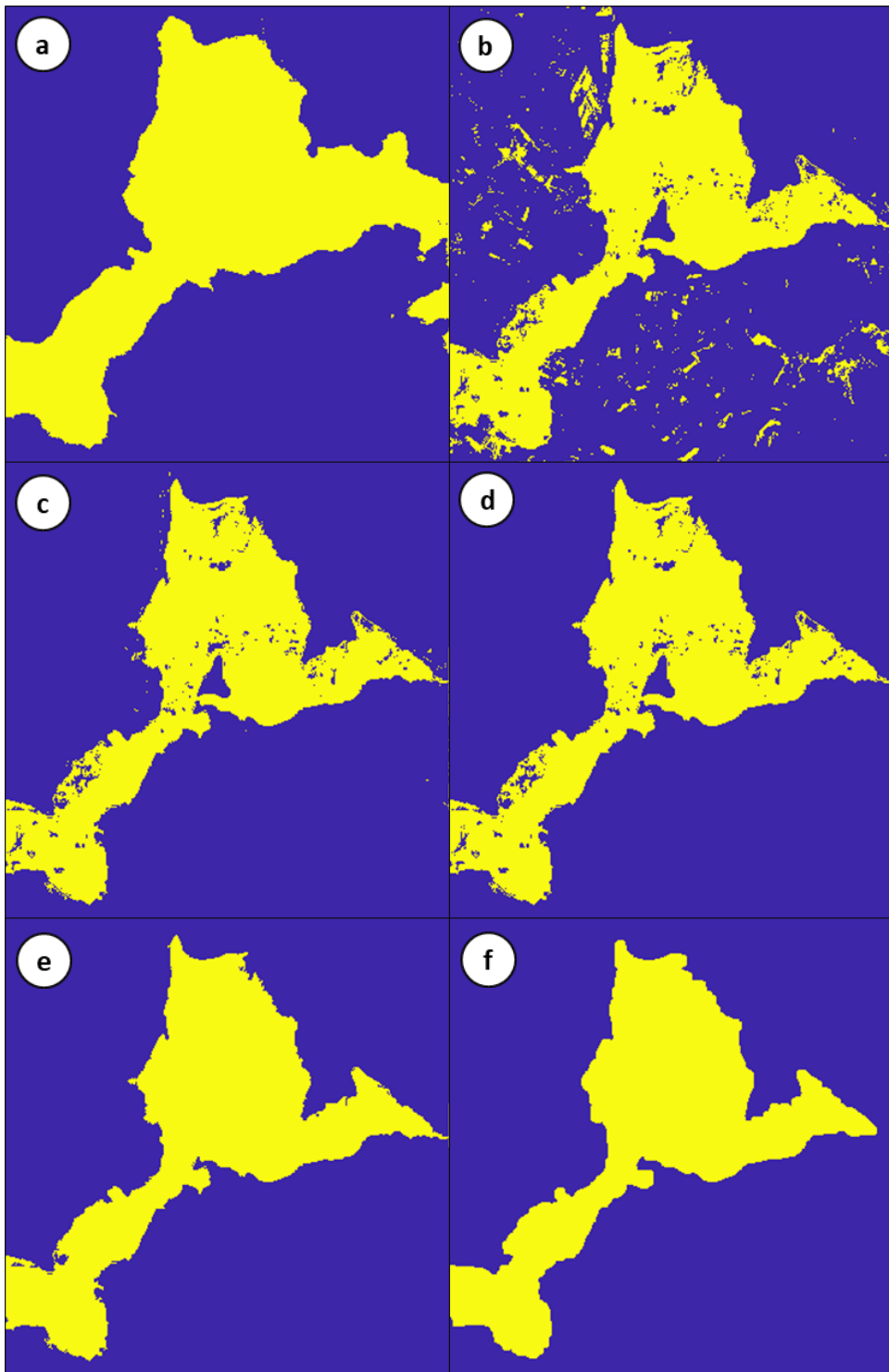


Figure 5.9 Evolution of wetland mask (a) DTM thresholding (b) Double-sigmoid fitting on TCWI stack (c) Intersection of a and b (d) Small object removal (e) Region/hole filling (f) Morphological opening

The final extent is compared with the ground truth extent digitized manually from high resolution orthophoto (Figure 5.10).

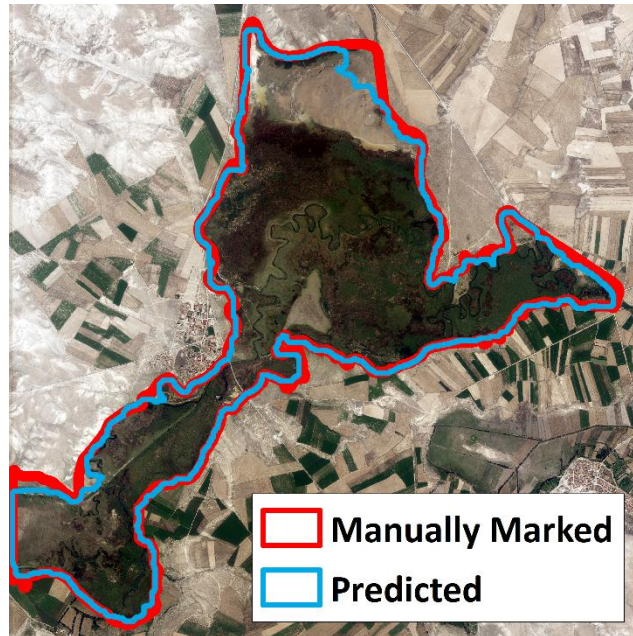


Figure 5.10 Manually marked vs. predicted wetland boundaries

The metric computations for the comparison are given in Table 5.3.

Table 5.3 Extent determination metric results for double-sigmoid fitting

<b>Frame Area (FA)</b>	3,899.10 ha
<b>Manually Marked Area (MMA)</b>	959.98 ha
<b>Predicted Area (PA)</b>	912.01 ha
<b>Union of MMA and PA (MMA <math>\cup</math> PA)</b>	967.20 ha
<b>True Positive Area (MMA <math>\cap</math> PA)</b>	904.79 ha
<b>True Negative Area (FA <math>\setminus</math> (MMA <math>\cup</math> PA))</b>	2,931.90 ha
<b>False Positive Area (PA <math>\setminus</math> (MMA <math>\cap</math> PA))</b>	7.22 ha
<b>False Negative Area (MMA <math>\setminus</math> (MMA <math>\cap</math> PA))</b>	55.19 ha
<b>Sensitivity/Recall (True Positive Rate)</b>	94.25 %

Table 5.3 Extent determination metric results for double-sigmoid fitting (continued)

<b>Specificity/Selectivity (True Negative Rate)</b>	99.75 %
<b>Precision (Positive Predictive Value)</b>	99.21 %
<b>Negative Predictive Value</b>	98.15 %
<b>Miss Rate (False Negative Rate)</b>	5.75 %
<b>Fall-out (False Positive Rate)</b>	0.25 %
<b>False Discovery Rate</b>	0.79 %
<b>False Omission Rate</b>	1.85 %
<b>Overall Accuracy</b>	98.40 %
<b>F<sub>1</sub> Score</b>	96.67 %

### 5.1.3 Spectral Signatures of Classes

Using the method explained in Section 4.5, the spectral signatures of the final classes are extracted. For the period between February and August 2019, the results are demonstrated in Figure 5.11.

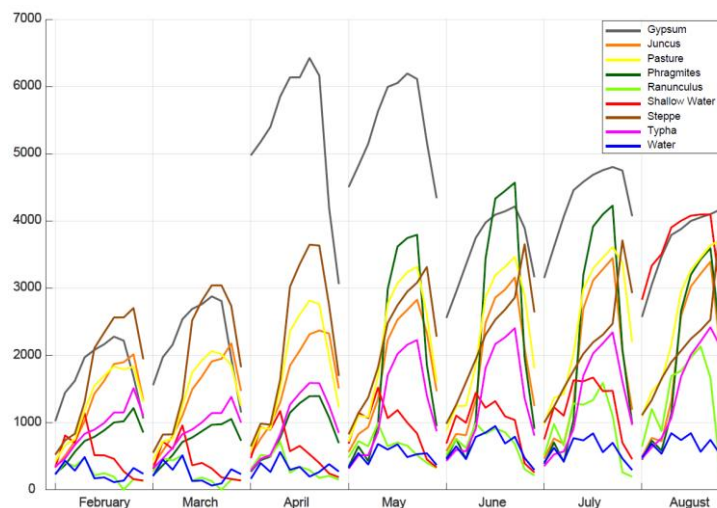


Figure 5.11 Spectral signatures of classes of 2019 mean monthly imagery for period between February and August

In order to check how the individual pixels contribute to the class-based spectral signatures, plots for polygon mean superimposed on single-pixel lines are generated for each class (Figure 5.12). In this way, the purity and similarity of pixels are inspected. In addition to the ten satellite bands, NDVI, NDWI, and TCWI bands are appended. In the end, irrelevant pixels are excluded, and the spectral library is refined accordingly.

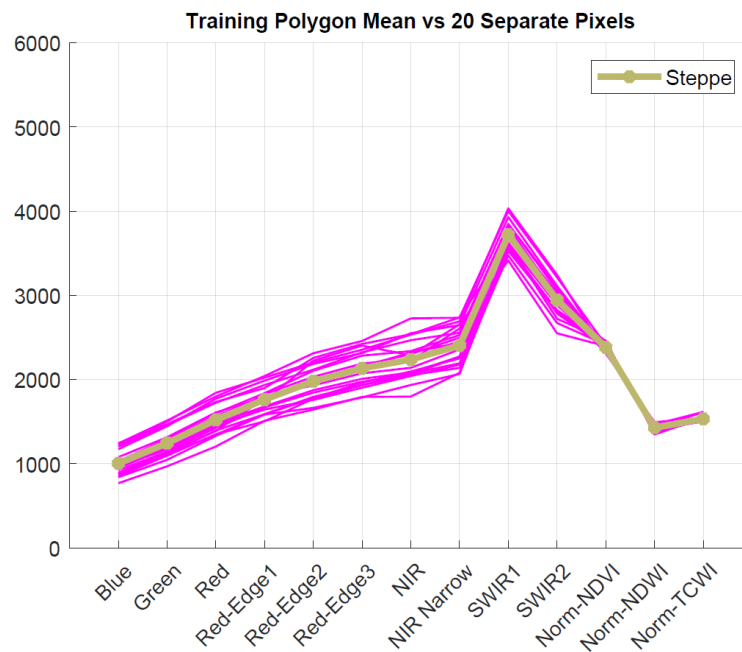


Figure 5.12 Spectrum comparison between mean and individual pixels

#### 5.1.4 Classification of Reference Orthophoto

5-fold cross-validated RF classification is performed in an effort to group wetland cover under nine classes mentioned in Section 4.4, which are Gypsum, Juncus, Pasture, Phragmites, Ranunculus, Shallow Water, Steppe, Typha, and Water. The confusion matrix is calculated once the procedure is completed (Figure 5.13). Using the elements of the calculated confusion matrix, the  $OA$ ,  $\kappa$ , and  $R^2$  are found as 98.86%, 98.56%, and 97.23%, respectively.

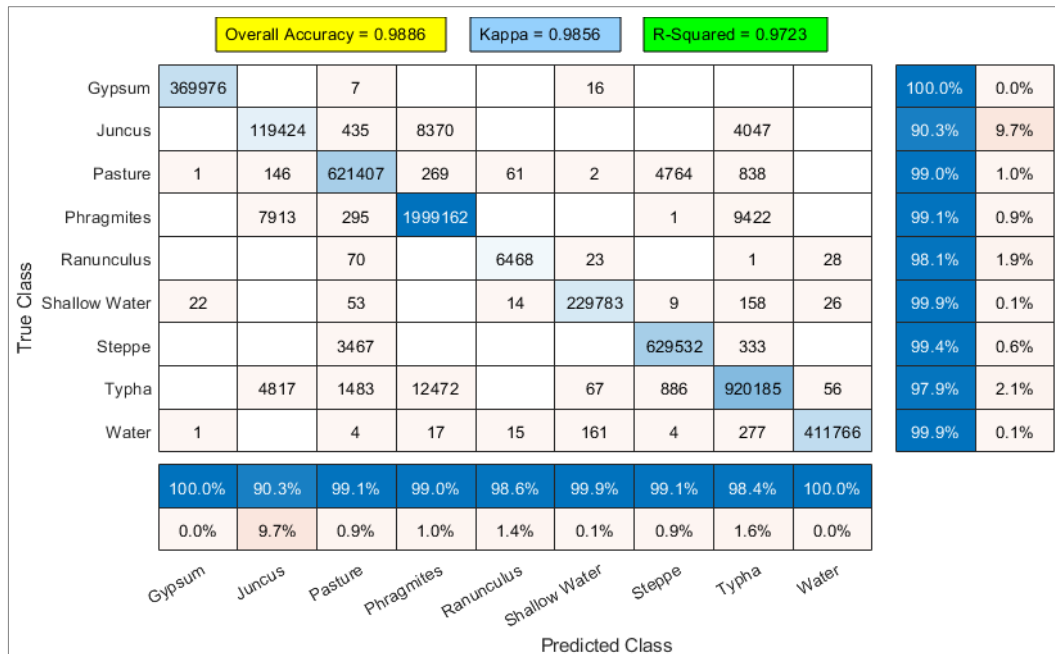


Figure 5.13 Confusion matrix for RF classification of orthophoto

The computed predictor importance estimates indicate that the DSM, NIR, and blue bands have the highest impacts (Figure 5.14, left). Moreover, out-of-bag (OOB) classification errors suggest that 15 trees are sufficient to reach the minimum error level (Figure 5.14, right).

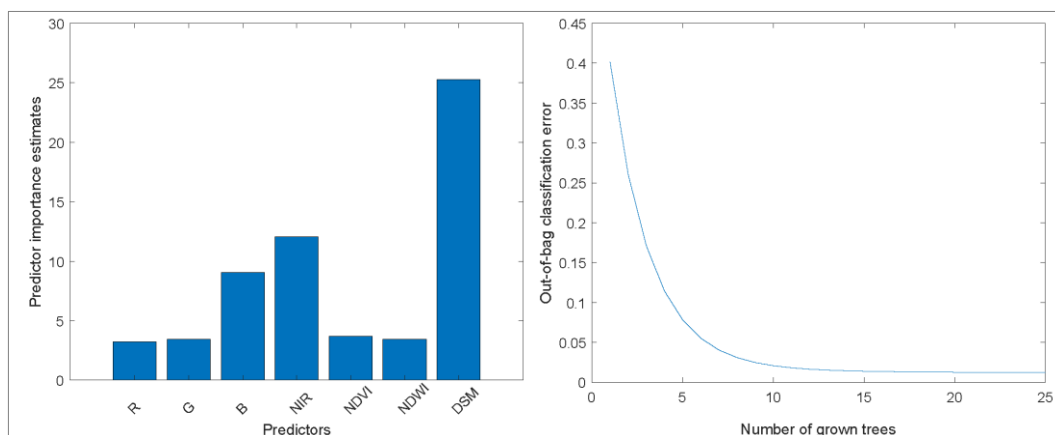


Figure 5.14 Parameter importance (left) and OOB error (right)

The output of the classification is displayed in Figure 5.15.

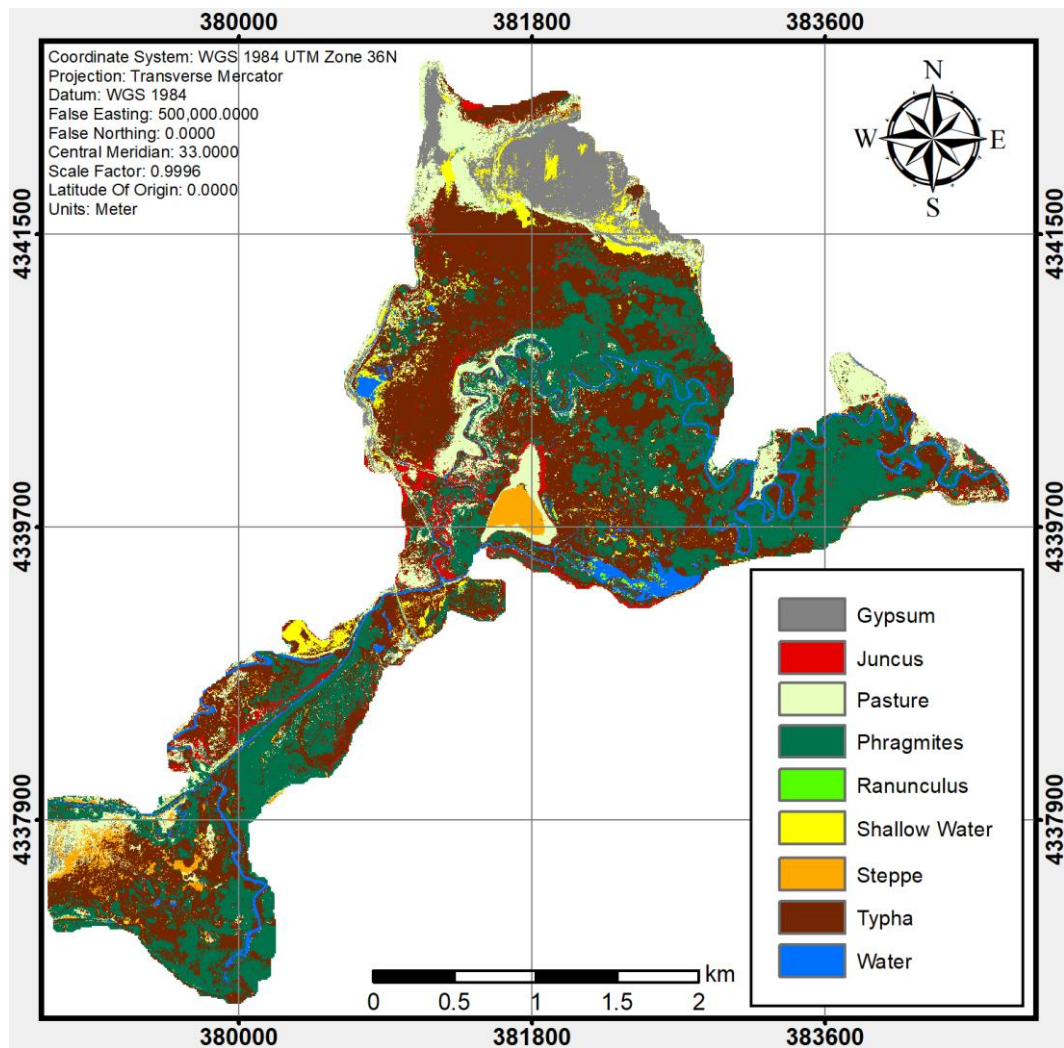


Figure 5.15 Classified orthophoto

## 5.1.5 Soft Classification of Sentinel-2 L2A Data

### 5.1.5.1 Spectral Unmixing

Five cloudless Sentinel-2 L2A images are used at this unmixing stage. The acquisition dates are given in Table 5.4. Considering the acquisition date of reference

data (20.07.2019), the maximum time interval between reference and target images is 19 days.

Table 5.4 Acquisition dates of Sentinel-2 July imagery

Acquisition Dates
01/07/2019
06/07/2019
16/07/2019
26/07/2019
31/07/2019

The final test data are formed by taking an average of above five frames to minimize the noise. The fully constrained linear spectral unmixing is performed subsequent to the band weight optimization procedure. The optimized band weights are given in Table 5.5, which are obtained through the algorithm demonstrated in Figure 4.12.

Table 5.5 Optimized band weights

Band No	Description	Weight
2	Blue	2.79
3	Green	3.98
4	Red	2.59
5	Vegetation Red Edge	1.27
6	Vegetation Red Edge	0.19
7	Vegetation Red Edge	0.21
8	Near Infrared	1.00
8A	Narrow Near Infrared	0.15
11	Short Wave Infrared	0.25
12	Short Wave Infrared	0.31



During the unmixing, non-negativity and sum-to-one constraints are included in line with the logic of the study. The estimated abundances are then compared with the reference data examining the ACOMA together with other aforementioned metrics. The accuracy metrics calculated for the spectral unmixing before and after the band weight optimization are given in Table 5.6.

Table 5.6 Comparison of spectral unmixing accuracy metrics for unoptimized and optimized band weight cases

	Without Optimization	With Band Optimization
<b>Overall Accuracy (OA)</b>	0.57	0.66
<b>Kappa (<math>\kappa</math>)</b>	0.46	0.56
<b>Coefficient of Determination (<math>R^2</math>)</b>	0.42	0.64
<b>Abundance Performance Metric (<i>apm</i>)</b>	0.64	0.73

The calculated abundance confusion matrix for the band weight optimization case is given in Figure 5.16.

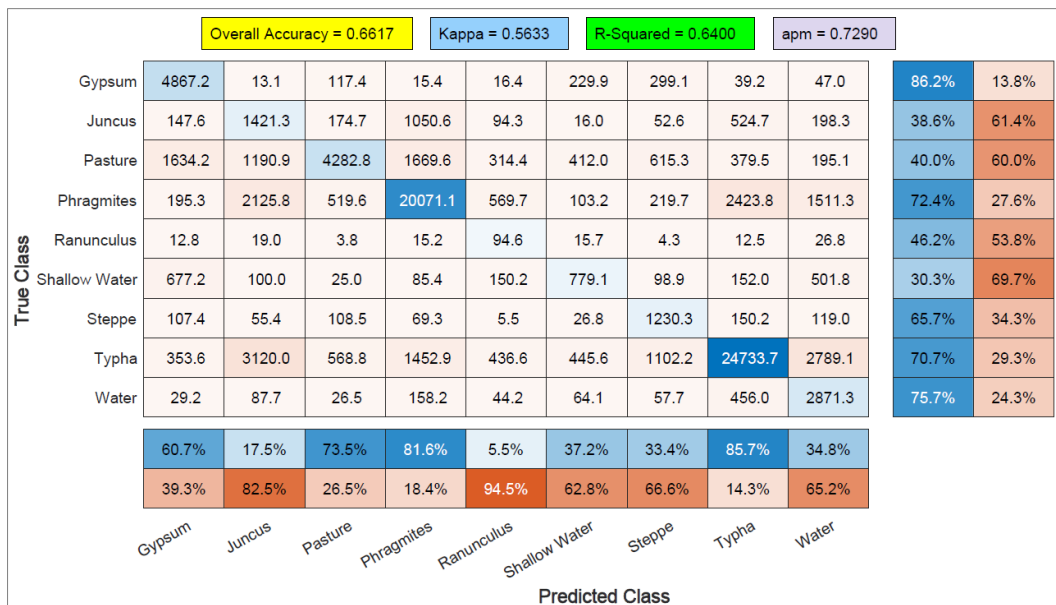


Figure 5.16 ACOMA for unmixed test data

In addition to the calculated metrics, endmember abundance distributions (Figure 5.17) and standard deviations are computed (Figure 5.18).

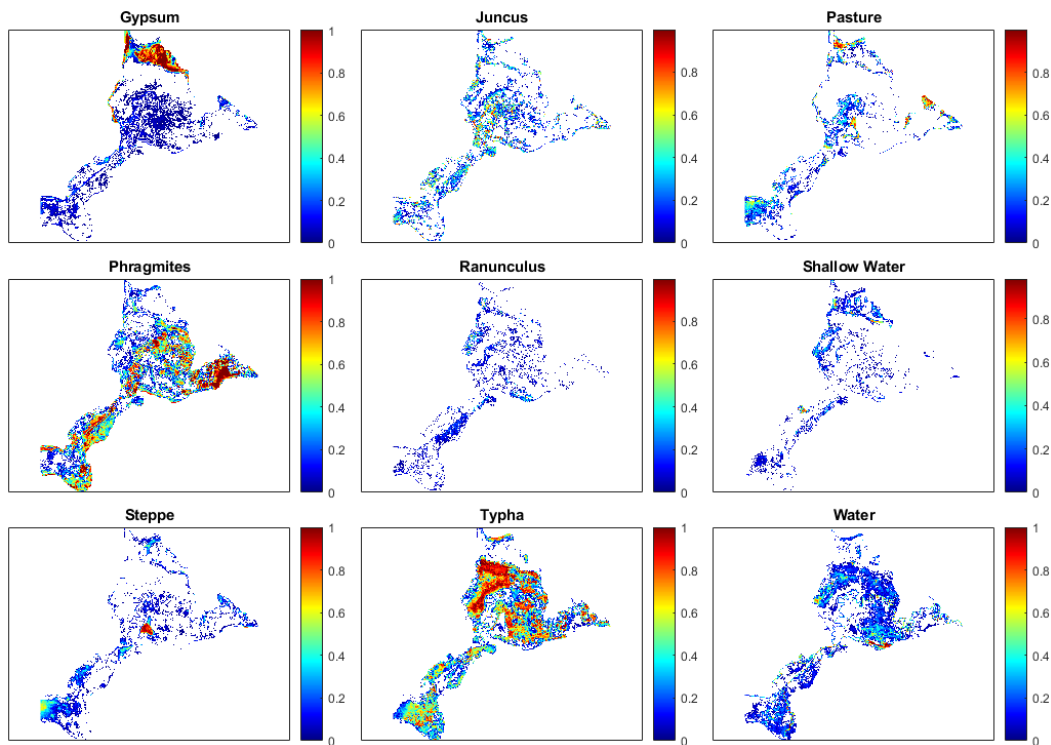


Figure 5.17 Abundance distribution for each endmember

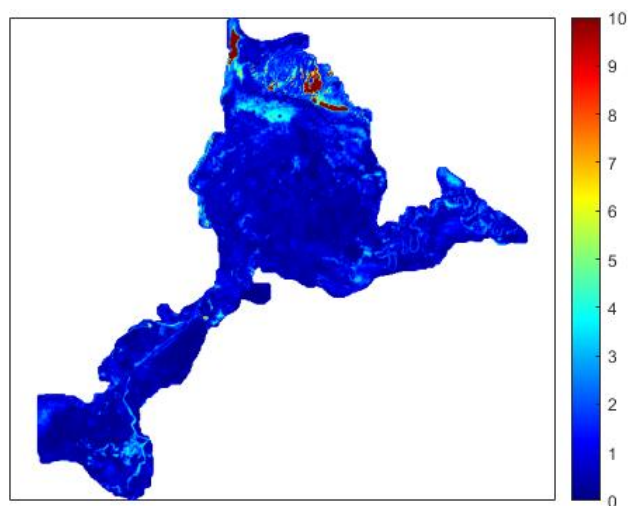


Figure 5.18 Standard deviations for monotemporal unmixing

Besides, the scatter plot of the reference and unmixed data is generated (Figure 5.19).

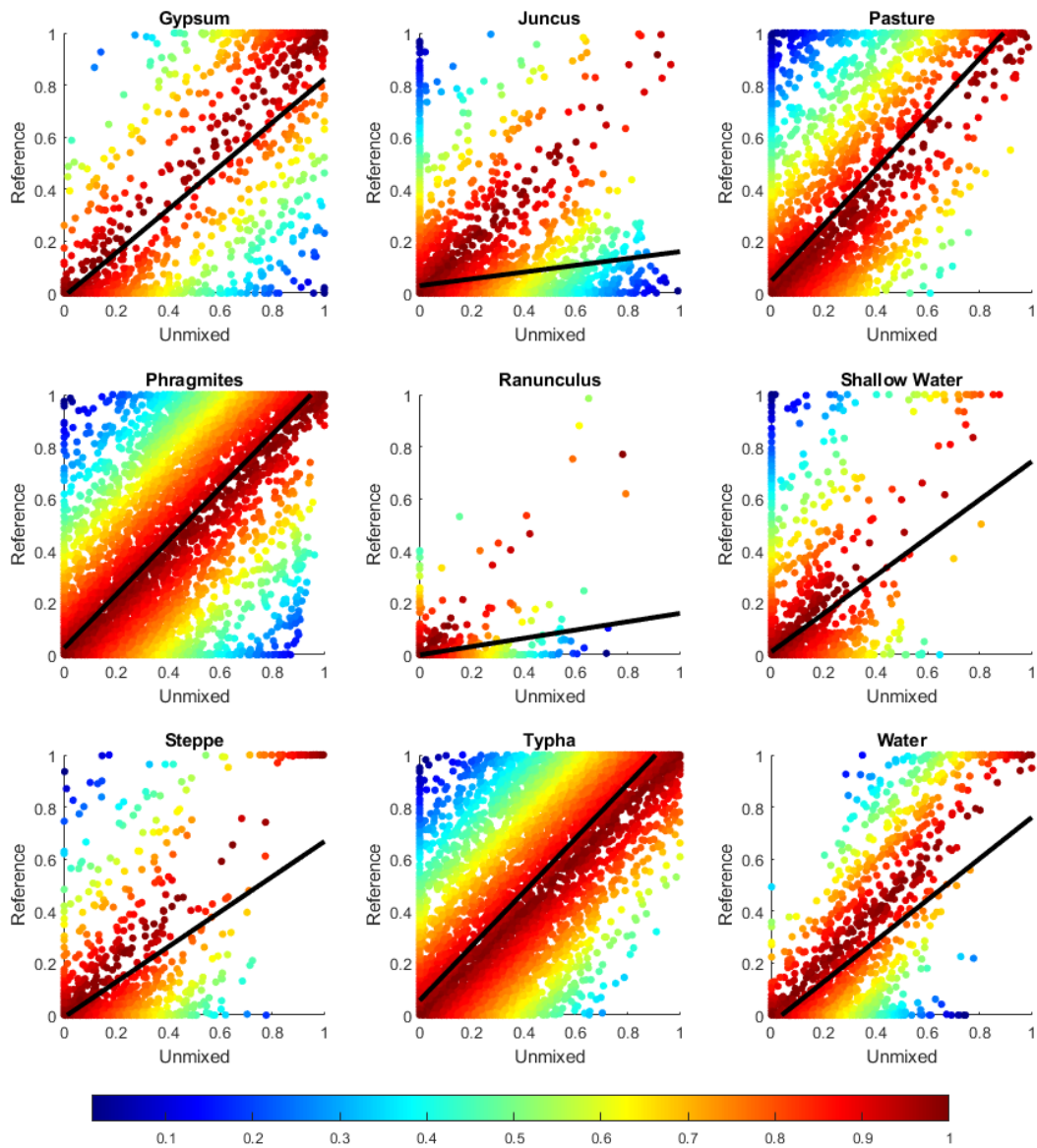


Figure 5.19 Scatter plot for randomly selected 10% of reference and unmixed pixels (colorbar shows consistency whereas black line denotes least squares line)

Abundance values are examined through a sample route to reveal the transition between land cover classes. The route and its direction are given in Figure 5.20. It intersects 45 unmixed pixels, whose contents are calculated and visualized with smoothing in Figure 5.21.

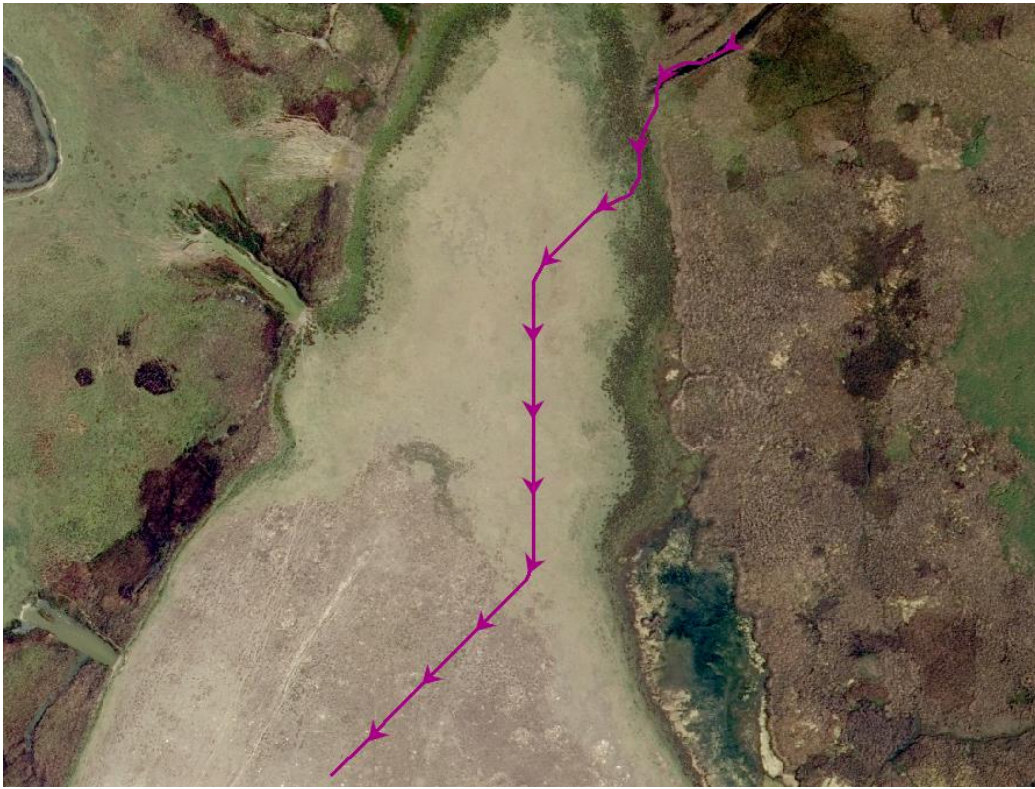


Figure 5.20 Transition route along which plant zonation is observed

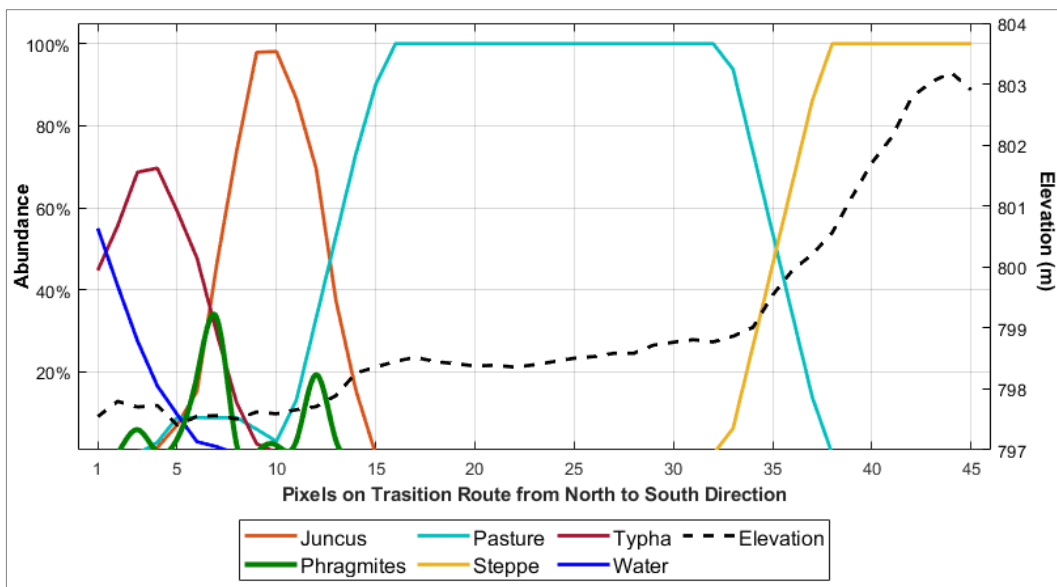


Figure 5.21 Plant zonation along transition route

The spectral unmixing accuracy is also compared with the RF classification of the same satellite data. Thus, the confusion matrix is calculated for the Sentinel-2 mean image (Figure 5.22). As in ground truth orthophoto classification, a 5-fold cross-validated RF approach is applied through the training polygons established to create the pure pixel spectral library.

		Overall Accuracy = 0.6423				Kappa = 0.5339				R-Squared = 0.0305		
True Class	Gypsum	5731080	2658	405577	829		57766	54977	8689	145	91.5%	8.5%
	Juncus	4214	1805257	592728	1029598	164	8716	11307	626669	1711	44.2%	55.8%
	Pasture	1666843	1633449	6729604	287252	797	362784	599637	564775	3789	56.8%	43.2%
	Phragmites	100	5452129	1456936	20309946	1966	27843	42650	3472209	30626	66.0%	34.0%
	Ranunculus	13756	6507	23643	24481	10511	80116	6471	51676	10097	4.6%	95.4%
	Shallow Water	907800	39777	153193	76704	2555	1049528	79603	410959	133682	36.8%	63.2%
	Steppe	19332	62686	351651	16363		105766	1134094	385351	1500	54.6%	45.4%
	Typha	68425	4266731	902397	4861216	11556	967288	665661	26412209	720996	67.9%	32.1%
	Water	29208	159484	51655	571760	20075	315406	19498	1203934	1842196	43.7%	56.3%
			67.9%	13.4%	63.1%	74.7%	22.1%	35.3%	43.4%	79.7%	67.1%	
		32.1%	86.6%	36.9%	25.3%	77.9%	64.7%	56.6%	20.3%	32.9%		
		Gypsum	Juncus	Pasture	Phragmites	Ranunculus	Shallow Water	Steppe	Typha	Water		
		Predicted Class										

Figure 5.22 Confusion matrix for RF classification of Sentinel-2 data

The comparison between the RF classification and spectral unmixing for an example area is shown in Figure 5.23.

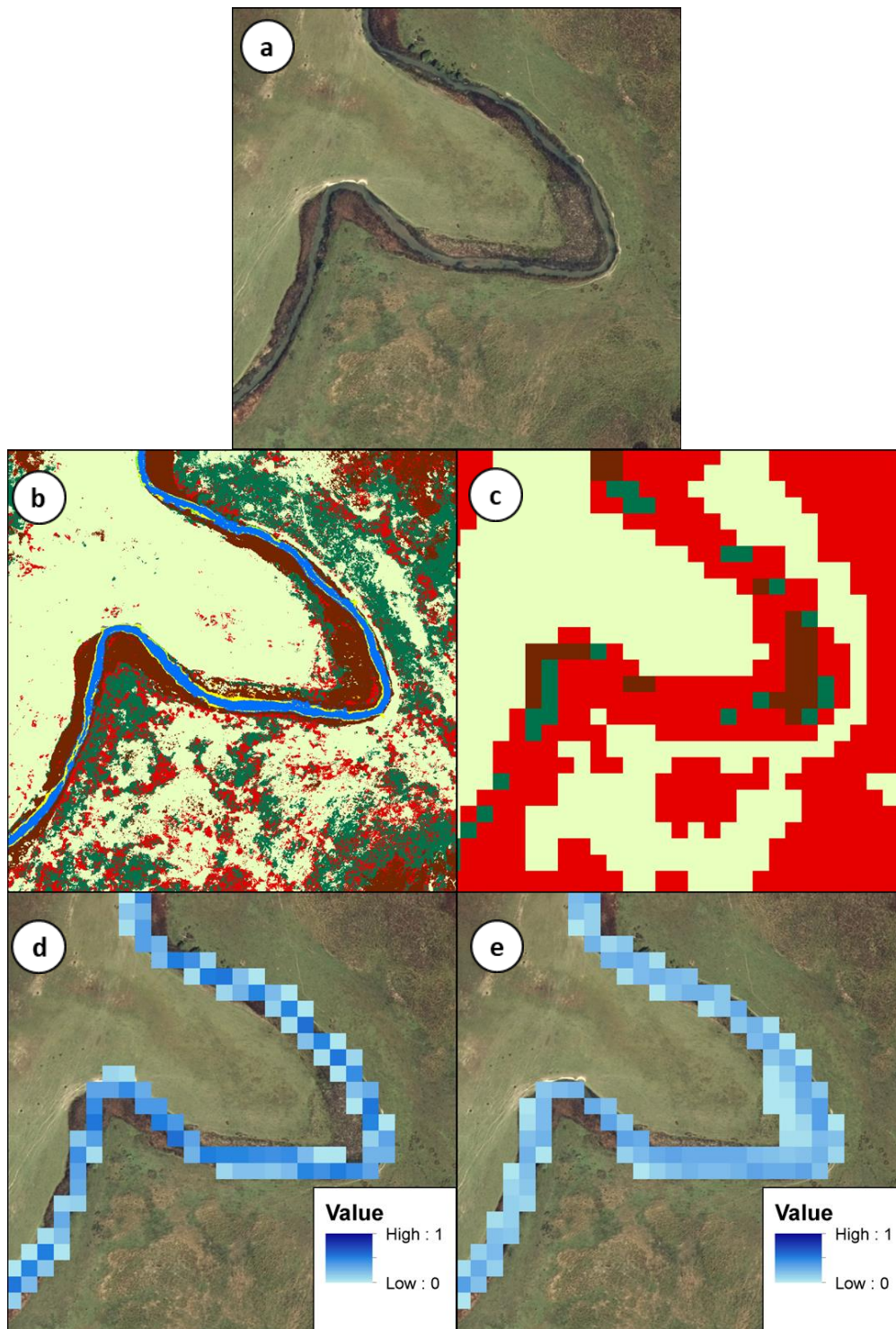


Figure 5.23 Example of land cover determination (a) RGB Orthophoto (b) Orthophoto RF classification (c) Sentinel-2 RF classification (d) Reference abundance data for water class only (e) Unmixing result for water class only

### 5.1.5.2 Spectro-Temporal Unmixing

In the next step, datasets of two seasons are stacked in order to exploit vegetation phenology for better classification and observe temporal changes throughout the year. For this task, imagery of April and July are utilized. In addition to the images mentioned in Table 5.4, an image dated 27/04/2019 is included in the process. So, a single April and an average of five July images are concatenated into a stack. Since there is only one cloudless image in April, averaging does not apply for April.

In addition to the band weight optimization, the endmember spectra are optimized using the sum of squared residuals between actual and reconstructed images as the error function. The original and optimized spectra are demonstrated in Figure 5.24.

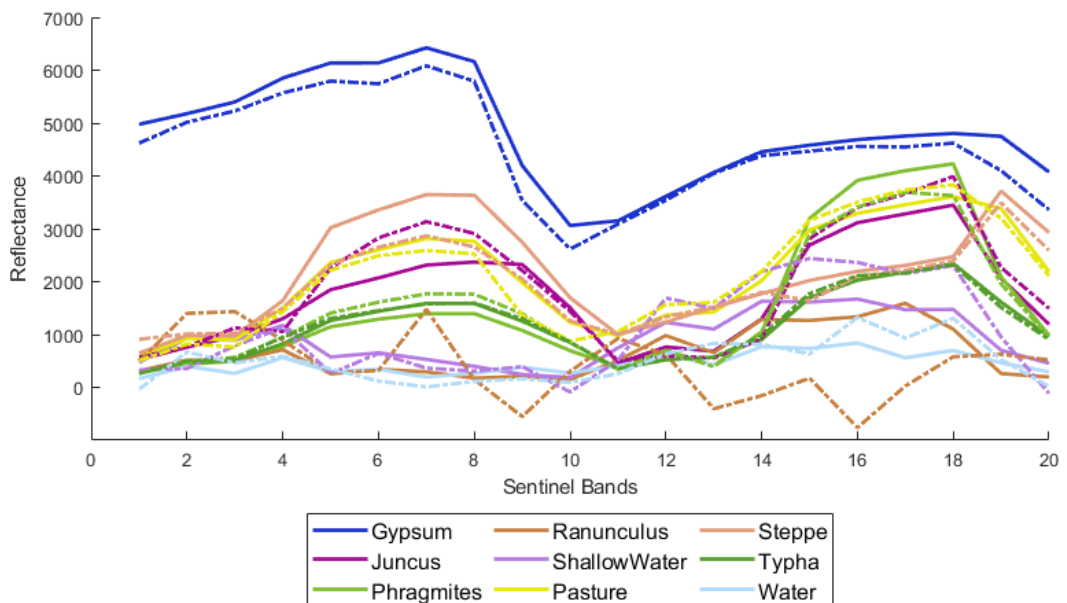


Figure 5.24 Unoptimized (solid) vs. optimized (dashed) endmember spectra for April and July image stack

After the spectra optimization, the spectral unmixing procedure is performed for the different combinations, and an accuracy check is carried out for the estimated

abundances. Different configurations are compared to reveal the impact of the individual and combined optimization steps (Table 5.7).

Table 5.7 Comparison of spectral unmixing accuracy metrics for different configurations

	Without Optimization	With Band Optimization	With Endmember Optimization	With Band and Endmember Optimization
<b>OA</b>	0.47	0.59	0.57	0.66
<b><math>\kappa</math></b>	0.37	0.49	0.47	0.56
<b><math>R^2</math></b>	0.13	0.49	0.40	0.64
<b><i>apm</i></b>	0.48	0.65	0.63	0.73

The calculated abundance confusion matrix for the combined optimization case is given in Figure 5.25.

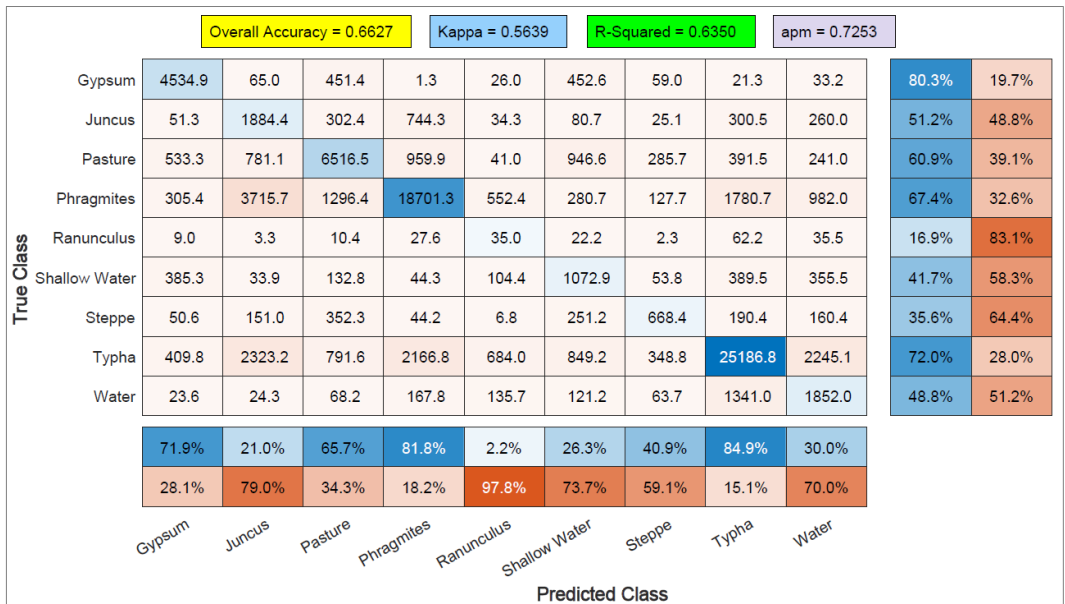


Figure 5.25 ACOMA for stacked data



Endmember abundance distributions (Figure 5.26) and standard deviations are computed (Figure 5.27) for the multitemporal outputs as in the single-input case.

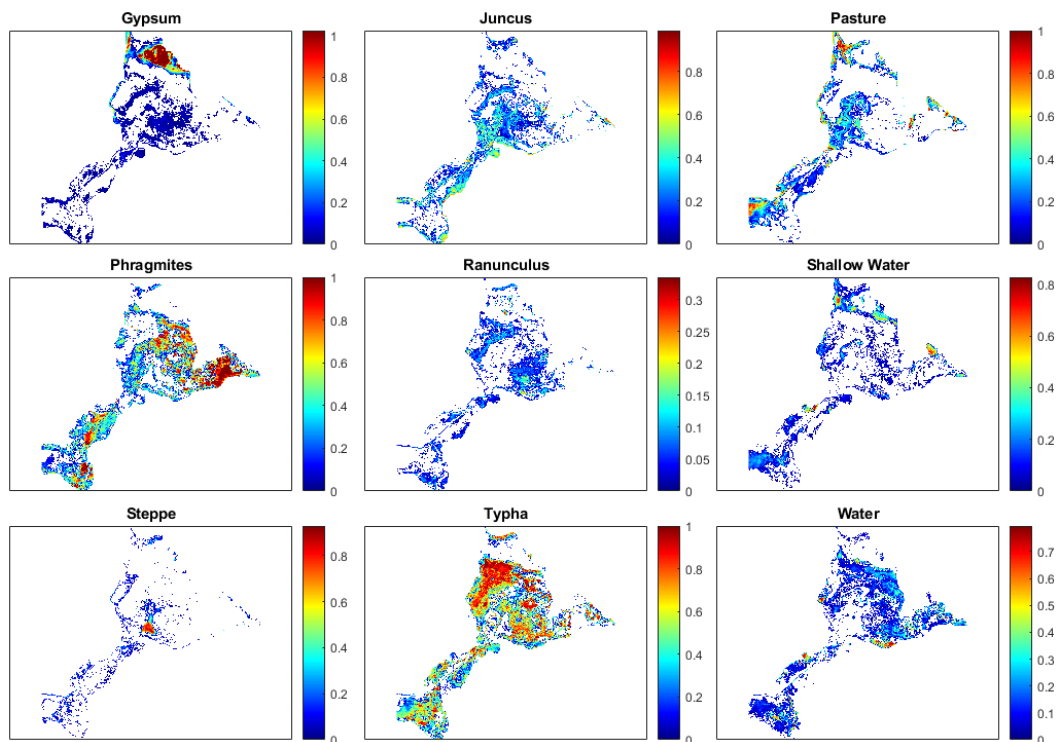


Figure 5.26 Abundance distribution for each multitemporal endmember

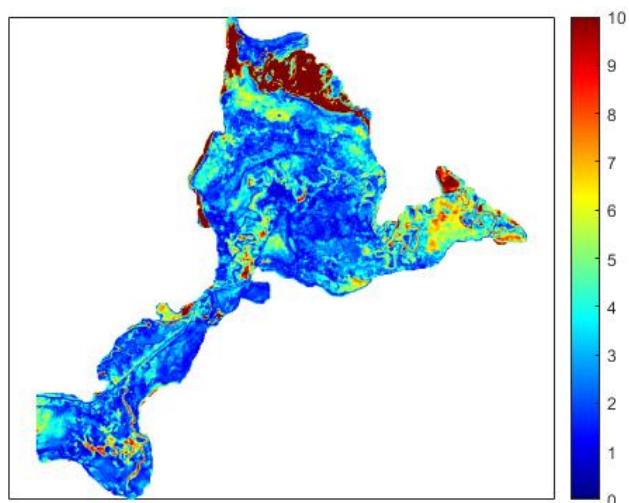


Figure 5.27 Standard deviations for multitemporal unmixing

Besides, the scatter plot of the reference and unmixed data is generated (Figure 5.28).

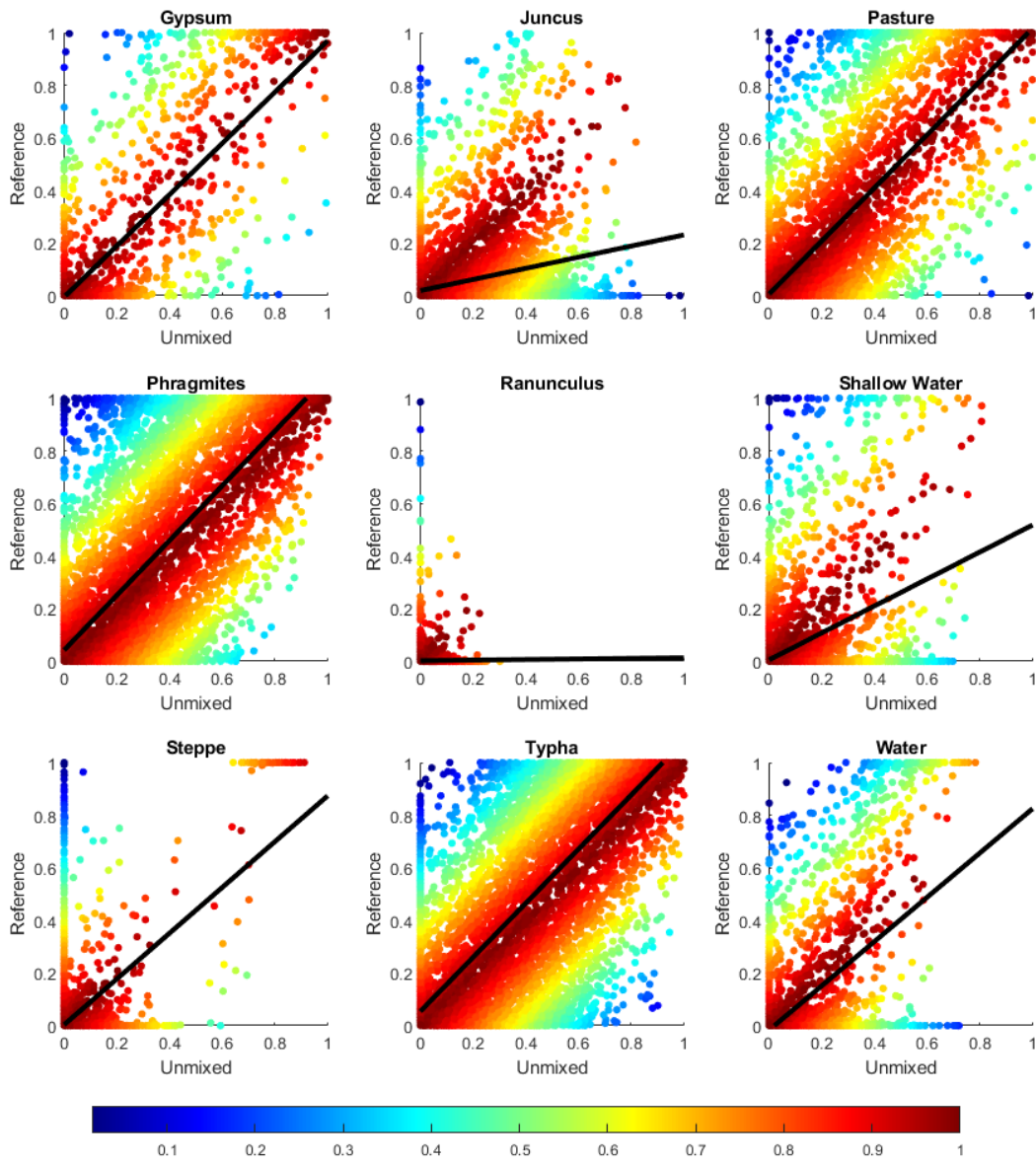


Figure 5.28 Scatter plot for randomly selected 10% of reference and unmixed multitemporal pixels (colorbar shows consistency whereas black line denotes least squares line)

The delta between monotemporal and multitemporal cases is computed for a more straightforward interpretation by subtracting the multitemporal stack from the monotemporal image. The result is given in Table 5.8.

Table 5.8 Delta matrix between monotemporal and multitemporal ACOMA

Gypsum	332.3	-52.0	-334.0	14.1	-9.6	-222.7	240.1	17.9	13.8
Juncus	96.3	-463.1	-127.7	306.3	60.0	-64.7	27.5	224.2	-61.6
Pasture	1100.9	409.9	-2233.7	709.7	273.4	-534.6	329.6	-12.0	-46.0
Phragmites	-110.1	-1589.9	-776.8	1369.8	17.3	-177.5	92.0	643.1	529.3
Ranunculus	3.8	15.6	-6.6	-12.3	59.5	-6.4	2.1	-49.7	-8.7
Shallow Water	291.9	66.1	-107.8	41.1	45.8	-293.8	45.1	-237.5	146.3
Steppe	56.9	-95.5	-243.8	25.1	-1.3	-224.4	561.9	-40.1	-41.4
Typha	-56.2	796.8	-222.8	-713.9	-247.4	-403.6	753.4	-453.1	544.0
Water	5.6	63.4	-41.7	-9.7	-91.5	-57.1	-6.0	-885.0	1019.3
<b>True</b> <b>Predicted</b>	Gypsum	Juncus	Pasture	Phragmites	Ranunculus	Shallow Water	Steppe	Typha	Water

### 5.1.6 Data Visualization

All input and output data are collected under a dynamic map for practical access and more straightforward interpretation. A temporary web server is exploited for publishing. The platform is also convenient to be used on desktop computers in case of the absence of a web server. It has a very user-friendly and easy-to-use interface. The map shows the dynamic scale and cursor coordinates continuously. It is

equipped with functional tools such as swipe, zoom, and geocoding. It has an additional magnifier and allows distance/area measurement, real-time location display, and local vector data upload. Figure 5.29 shows the interface of the interactive map.

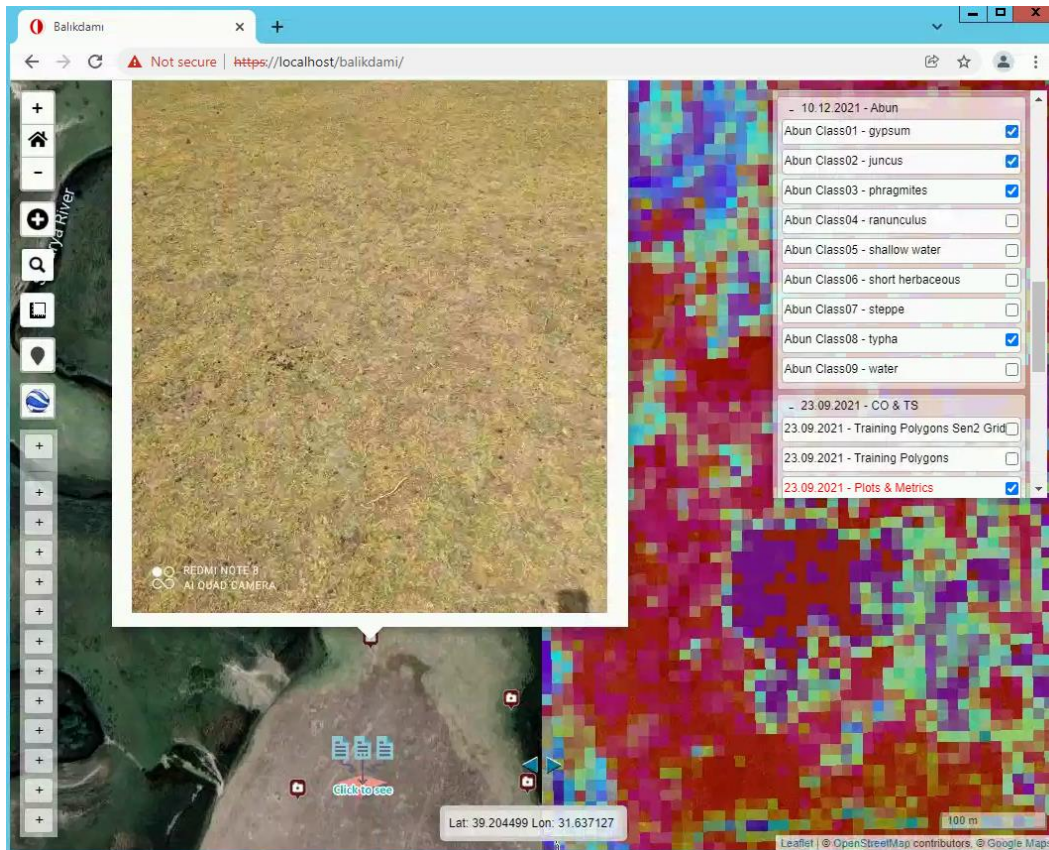


Figure 5.29 Visualization of inputs and outputs via the interactive map

## 5.2 Discussion

In order to check the necessity of co-registration, a simple test is performed, which is shifting the reference abundance map for one pixel in the east direction since it is very likely to have an offset to such a degree in the satellite data. For the assessment of the variation between original and shifted values,  $R^2$  is calculated. The value of 0.72 suggests that a significant loss occurs if there is a misalignment. Since absolute

shifts of more than half a pixel ( $> 5$  m) are present in the satellite imagery, as shown in Figure 5.1, the necessity of co-registration is verified.

In the evaluation of the co-registration process, only the correlation coefficient is appraised as an assessment metric. The reason not to use distance-based metrics such as the sum of squared errors (SSE), mean squared error (MSE), root mean squared error (RMSE), and mean absolute error (MAE) is because the reference data generated from aerial imagery quantify radiance, whereas the target satellite data quantify scaled BOA reflectance. Even if normalization is applied, this variation causes inconsistency in the comparison outputs. The similarity-based metrics such as spectral angle mapper (SAM), structural similarity index measure (SSIM), and universal image quality index (UIQI) are not also reported since one of the target images dates back to five months earlier in addition to the former reasoning. The gap between the acquisition dates of reference and target data results in a substantial amount of absolute dissimilarity. In the case of utilizing reference and target datasets of similar nature and close acquisition dates, checking the mentioned metrics will be useful.

The proposed wetland extent determination algorithm indicates that the actual extent is extracted with a miss rate of 5.75%. It should be noted that the algorithm's precision is very high (99.21%). One of the challenges is the existence of large agricultural fields irrigated all year long in the vicinity of wetland. They tend to reflect wetland characteristics in a wetness sense. Another error source is the existence of arid regions, especially in the north part, where the large Gypsum cover locates. This part remains entirely parched during the summer season, insomuch that a cracked texture occurs. As a result, the TCWI stays low in this area, and the thresholding operation incorrectly filters out that part of the wetland. Even though introducing proper settings during morphological operations sorts out this issue on a large scale, the most significant error accumulation is still observed in the northernmost boundary of the wetland, where the TCWI values hardly ever exceed the specified threshold throughout the year. On the other hand, there is no vital error,

in general, affecting the subsequent phases, and the proposed approach is essentially applicable to wetlands in arid and semi-arid climates.

The best part of the proposed wetland extent determination algorithm is that it does not necessarily require high resolution DEM. Publicly available elevation data provide sufficient locational accuracy to fulfill the DEM thresholding requirement for rough boundary extraction. A sensible outcome is obtained as a starting point even with 1-arc second SRTM data dating back to 2000. The rest is handled through the use of Sentinel-2 data. In case of need, other free-of-charge satellite data such as Landsat-8 can be utilized.

The data provider claims 2 m absolute mapping accuracy for the provided interior and exterior parameters. As a rule of thumb, the expected relative accuracy of an aerial mapping project is within one to three times GSD, that is, a value between 30 cm and 90 cm for this dataset. On the other hand, the sub-pixel scale co-registration procedure is applied to the satellite images using the generated orthophoto. Therefore, the reference orthophoto is not corrected for better positional accuracy.

The orthophoto classification looks virtually flawless, with an overall accuracy of 98.86%. The main reason for achieving unexpectedly high accuracy is the designation strategy of training samples, which is simple random sampling. Simple random sampling may lead to relatively deceptive performance originating from sampling error if the collected sample of a class is not large enough to represent the views of the entire population. Although it is challenging to implement stratified random sampling in such a highly heterogeneous environment containing relatively small land covers, it should be preferred to ensure equal statistical power when comparing sub-pixels. On the other hand, adding the extra bands and applying the folding procedure should be credited as well as the Random Forest classification method itself since it utilizes bagging and feature randomness to create uncorrelated forest structures. In turn, the RF outperforms single decision trees thanks to the improved performance and generalization. Among the classes, *Juncus* has relatively

low accuracy (Figure 5.13) and is confused with Phragmites, Typha, and Pasture. This confusion makes sense since the Juncus cover is mainly located at these classes' transition zones. The most likely cause for the confusion is that the Juncus cover is not dense.

The DSM, NIR, and blue are the highest importance bands concerning the predictor importance estimates. Since the altitude has a distinctive effect on most land cover classes, DSM is logically the dominant feature. The NIR band effectively separates water bodies from vegetation with its sensitivity to vegetation type, biomass, moisture content, and general plant health. Thus, it comes after DSM rationally. It is not surprising to have the blue band in third place since it provides good water penetration. Therefore, it is widely preferred in remote sensing applications like submerged aquatic vegetation, turbidity, and bathymetric mapping. It should be borne in mind that Figure 5.14 shows relative importance. In order to reveal the contribution of other bands, the RF orthophoto classification is renewed just using the mentioned three dominant bands. Figure 5.30 demonstrates that the accuracy decreases dramatically, mainly for two classes. Hence, other features provided by different spectral portions should not be omitted.

		Overall Accuracy = 0.9482		Kappa = 0.9343		R-Squared = 0.8889						
True Class	Gypsum	369581		15			381	20	1	1	99.9%	0.1%
	Juncus		76870	4773	43990	2			6640	1	58.1%	41.9%
	Pasture	11	4872	597752	3580	755	1671	9483	9355	9	95.3%	4.7%
	Phragmites		38482	3399	1910395	2			64510	5	94.7%	5.3%
	Ranunculus		2	1654	2	3265	379		1145	143	49.5%	50.5%
	Shallow Water	1266		1315		76	225035	74	857	1442	97.8%	2.2%
	Steppe	29		11420			21	620771	1082	9	98.0%	2.0%
	Typha	9	7466	9375	41578	674	544	1673	878288	359	93.4%	6.6%
	Water	5	10	53	24	69	1899	22	1340	408823	99.2%	0.8%
			99.6%	60.2%	94.9%	95.5%	67.4%	97.9%	98.2%	91.2%	99.5%	
		0.4%	39.8%	5.1%	4.5%	32.6%	2.1%	1.8%	8.8%	0.5%		
		Gypsum	Juncus	Pasture	Phragmites	Ranunculus	Shallow Water	Steppe	Typha	Water		
		Predicted Class										

Figure 5.30 RF classification results for 3-band (Blue/NIR/DSM) composite

The smaller weights calculated for bands 5, 6, 7, 8A, 11, and 12 compared to bands 2, 3, and 4 (Blue, Green, and Red) are reasonable since they are resampled from  $20m \times 20m$  pixels using the Nearest Neighbor algorithm. Ultimately, the proposed band optimization step justifies its significance regarding the increases in accuracy metrics. The  $OA$ ,  $\kappa$ ,  $R^2$ , and  $apm$  escalate in the order of 9%, 10%, 22%, and 9%, respectively (Table 5.6). The increase in  $R^2$  is strikingly formidable as it doubles the other metrics. This increase means that the distribution of errors is homogenized apart from obtaining better predictions. In other words, error accumulation for an individual class is avoided. Two classes, Juncus and Ranunculus, have sizably high commission errors. Nonetheless, it is still meaningful to keep them, considering the relatively lower omission errors. Particularly the total surface area of Ranunculus is already tiny and very dispersed in the reference data, causing inefficiency in the pure spectral signature determination. This issue, unfortunately, propagates into the unmixing process heavily.



The endmember abundance distributions shown in Figure 5.17 apparently reveal the class-based presence throughout the wetland area. Broader red areas seen on Gypsum, Phragmites, and Typha sub-plots signify that these three classes are more compact than other classes. The following classes are Pasture, Steppe, and Water in terms of denseness. Another noticeable point is the existence of water to a certain extent all over the wetland. The unified Shallow Water and Water cover demonstrates that nearly the whole land is partly wet, reflecting the general wetland character. This feature is also consistent with the findings of the wetland extent determination part. The overestimation of Ranunculus is notable, whose reason is already emphasized.

Figure 5.18 suggests that the highest standard deviations are observed in the Gypsum class. At first glance, it might seem quite odd to have such a large and continuous cover in the lead. Although abundance estimates are accurate and spectral signature is extracted from a sufficient number of truly pure pixels, the figure demonstrates the higher residuals between original and reconstructed images obtained over the brightest areas. This anomaly occurs due to moisture. Even though the surface is arid, the underneath moisture modulates the radiance values. This collective modulation, in return, does not affect the accuracy of abundance estimation but the class spectrum.

Figure 5.19 delineates the scatter of the predicted abundances against reference data. The aspects mentioned earlier are clearly highlighted. The class-based levels for over and underestimates are more comprehensible thanks to the least square lines. It can be easily realized that the Ranunculus and Juncus classes are highly overestimated.

One of the great potentials of the adopted approach is its ability to ensure plant zonation in transition routes. Figure 5.21 cleverly demonstrates the results generated for the example route given in Figure 5.20. It illustrates the class alterations starting from the waterside to an inner region. As moving towards inland, the water content of the pixels gradually decreases, whereas the plants slowly emerge. The area where

this route lies is explored during site visits. As Figure 5.21 illustrates, the order of plants is Typha, Phragmites, and Juncus. The smooth transition in between can also be seen in the high resolution base map. Besides, the broad Pasture and Steppe regions without mixed content reveal themselves. The increasing elevation values observed through the route support the other findings. The slope alterations seen on the transition spots of the plot agree with the class interactions. It should be expressed that the elevation values slightly fluctuate between adjacent pixels because they are calculated by averaging the pixels of the high resolution elevation model falling into the related Sentinel-2 grid. In other words, each corresponding elevation value on the plot represents the mean of approximately 1,100 high resolution pixels.

The spectral unmixing approach proves its functionality in identifying sparse land covers. As shown in Figure 5.23, narrow land covers with respect to the Sentinel-2 grid are able to be detected with the implemented procedure. In addition to preventing the disappearance of sparse land covers, the  $OA$ ,  $\kappa$ , and  $R^2$  of 66%, 56%, and 64% for fractional mapping (Figure 5.16) and 64%, 53%, and 3% for hard classification (Figure 5.22) prove that the unmixing approach outperforms the pixel-based classification in terms of the accuracy. Especially the difference for  $R^2$  values is very remarkable, which signifies the class-based error accumulation in the hard classification. This difference lies behind the extremely low producer's accuracy for the Ranunculus class given in Figure 5.22.

In the multitemporal case, endmember optimization is implemented in contrast to the monotemporal case. In theory, the lower bound for the estimated spectra must be zero since reflectance values cannot be negative. However, no bound is set to cancel out artifacts. For this reason, some of the band spectra belonging to the Ranunculus class end up with negative values, as seen in Figure 5.24. The calculation of metrics stresses the importance of optimization steps. The best results are obtained when the proposed band weights are utilized together with the optimized spectra for the spectro-temporal case. In addition to the reported two-month stack accuracies, composites created from different combinations of more months' data are unmixed

and evaluated. However, the overall accuracy does not rise above the result of the two-month composite. This is mainly due to irregular land surface phenology caused by external factors/anomalies. Under entirely natural conditions, stacking data from more months/seasons/years is expected to provide higher accuracy. On the other hand, the temporal behavior of changes can still be interpreted thanks to the ACOMA.

As in the monotemporal case, ACOMA provides an outstanding contribution to interpreting the outcomes. When the results of the monotemporal and multitemporal implementations are compared (Figure 5.16 vs. Figure 5.25), the exchange between particular classes draws attention. One of the most evident exchanges that can be commented on in Table 5.8 is the transformation of Pasture into Gypsum. This makes perfect sense because stack data include April/July images, whereas the monotemporal data contain only July information. In other words, entering the summer season has an effect of a decrease in the water level and drying grass. Another relation is seen between Phragmites and Juncus. Since the flowering months are July and August for Juncus (Groww, 2022), a larger area of the Juncus cover is anticipated in July compared to April. Thus, this alteration is reasonable as well. Lastly, the interaction between Typha and Water is striking. Especially the last row of the delta matrix reveals this relation. Considering the fact that Typha grows primarily next to the water in the area, this relation is comprehensible. On the other hand, the reason for such a decrease in the Typha cover is a bit confusing.

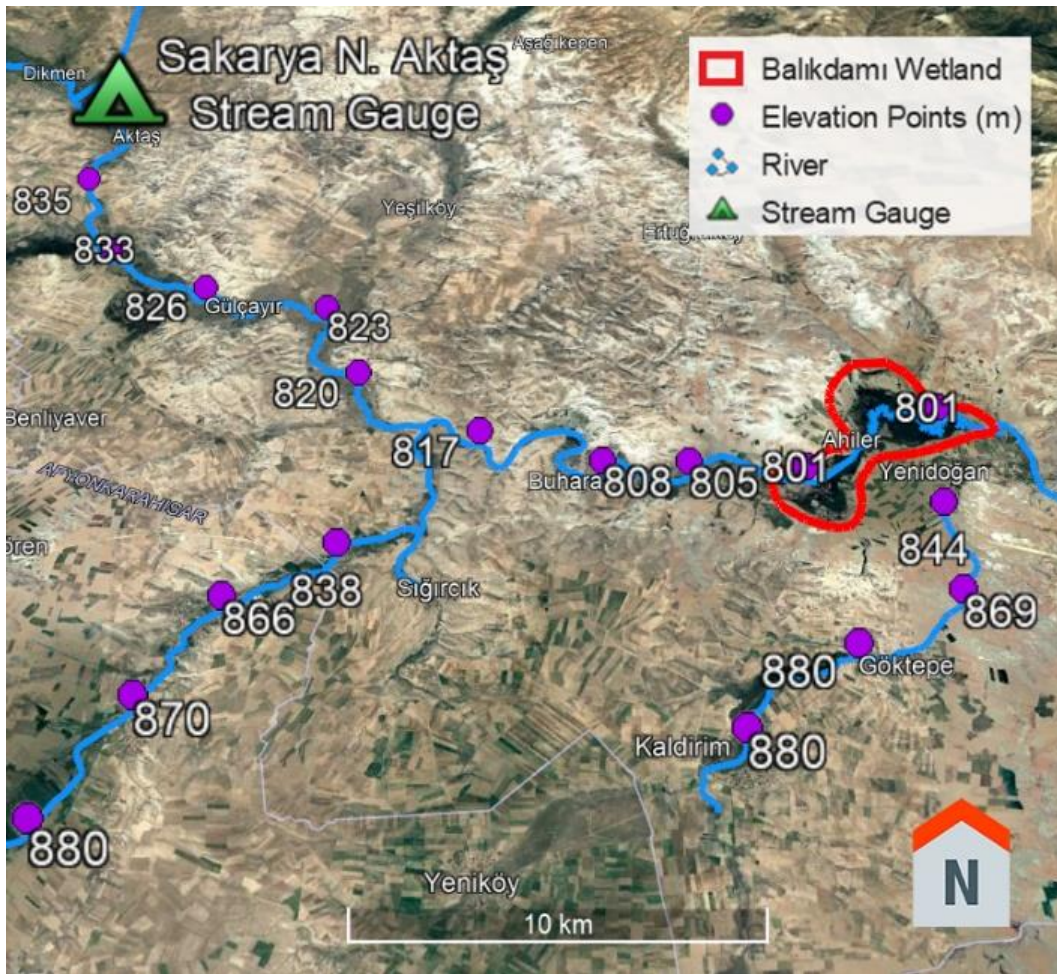


Figure 5.31 Location of Sakarya N. Aktaş stream gauge and region topography

Figure 5.26 and Figure 5.27 indicate similar outputs apart from the absolute increase in standard deviations. This is an expected situation since the reference data belong to a single season. In addition, the issue with *Ranunculus* is rationally even more severe (Figure 5.28). Except for the seasonal effect, the mobility of the class should be taken into account. Although this class is mainly observed on the surface of slow-flowing water, displacement is anticipated considering the three-month interval. In relation to the subject displacement, the river's flow rate is checked with the data provided by the nearest stream gauge (E12A024 – Sakarya N. Aktaş). It is located about 30 km northwest of the wetland, whose approximate elevation is 837 m (**Error! Reference source not found.**).

The most recent accessible data belong to the 2015 water year (General Directorate of State Hydraulic Works, 2018). The monthly average flow rates contained in the report indicate that the rate of July (5.77 m<sup>3</sup>/sec) is below the annual average (6.45 m<sup>3</sup>/sec), whereas the fastest rate is observed in April (11.20 m<sup>3</sup>/sec). Hence, it is very likely to have displaced Ranunculus formation, if any exists in April. Figure 5.32 shows the observed average flow rates. The complete station report, including daily observations, is given in Appendix D.

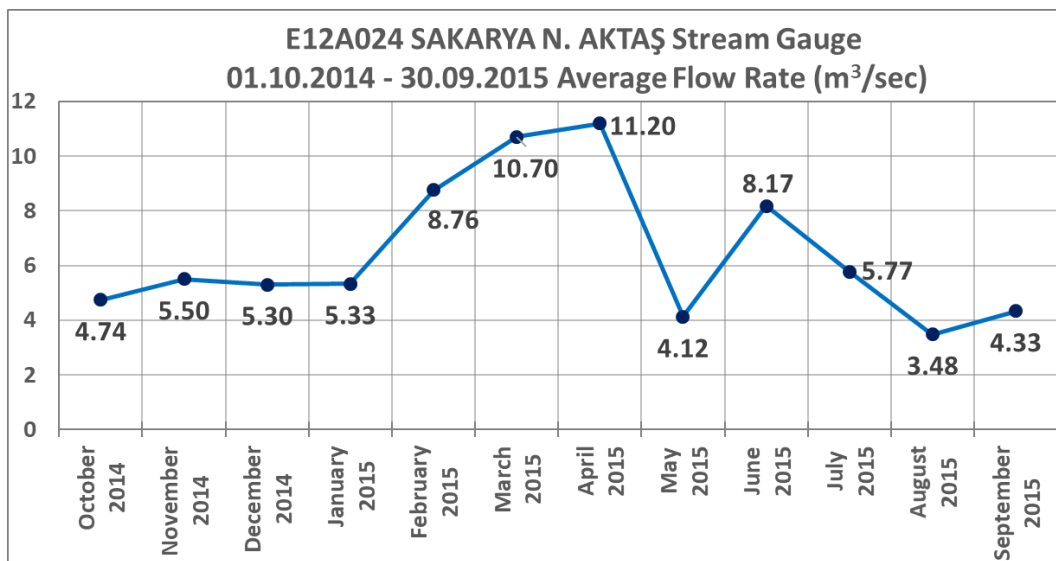


Figure 5.32 Monthly average flow rate (m<sup>3</sup>/sec) at Sakarya N. Aktaş stream gauge for 2015 water year

The assumption deduced from the mentioned flow rates is supported by the monthly precipitation totals for 2019. The statistics show that the precipitation total for July 2019 (17.4 mm) is almost half the annual average (32.8 mm), whereas the April total (43.9 mm) is two and a half times higher than that of July (Eskişehir Metropolitan Municipality, 2020).

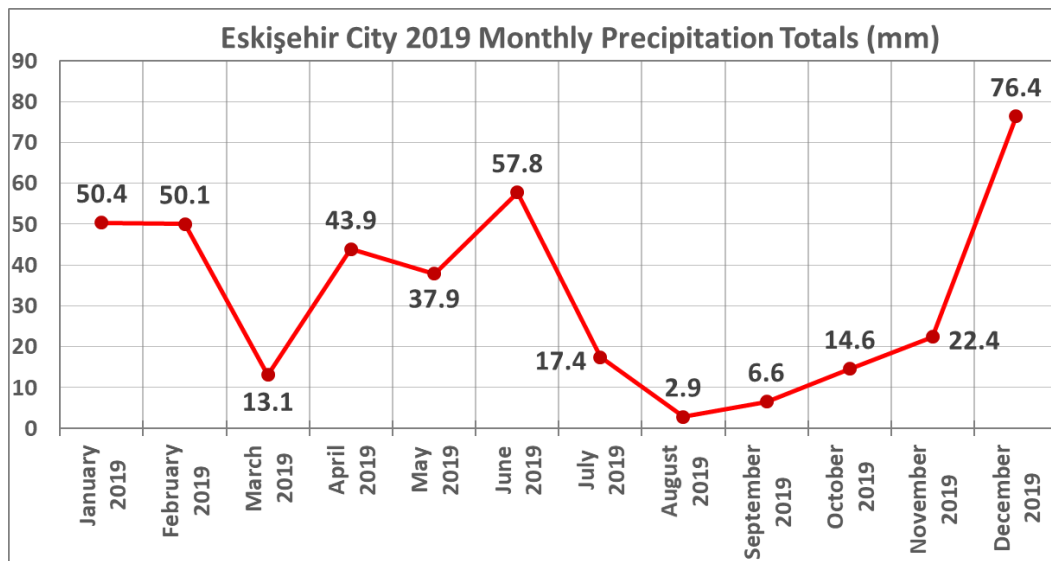


Figure 5.33 Eskişehir City 2019 monthly precipitation totals (mm)

The assumption deduced from the mentioned flow rates is supported by the monthly precipitation totals for 2019. The statistics show that the precipitation total for July 2019 (17.4 mm) is almost half the annual average (32.8 mm), whereas the April total (43.9 mm) is two and a half times higher than that of July (Eskişehir Metropolitan Municipality, 2020).

The behavior of *Ranunculus* is also checked out using the high resolution satellite imagery provided by Google Earth. In order to reveal the dynamic change and movement, the reference orthophoto (20.07.2019) and the most recent image to orthophoto existing on GE (15.09.2019) are visually compared. It is clearly seen that there is a significant amount of *Ranunculus* coverage difference between the two datasets. Considering the fact that the period between two images is shorter than two months, benefiting from multiple seasons for this class type is quite tricky. It should be emphasized that these kinds of dynamic targets require special attention and the implementation of complex approaches. Figure 5.34 shows the two images mentioned above.

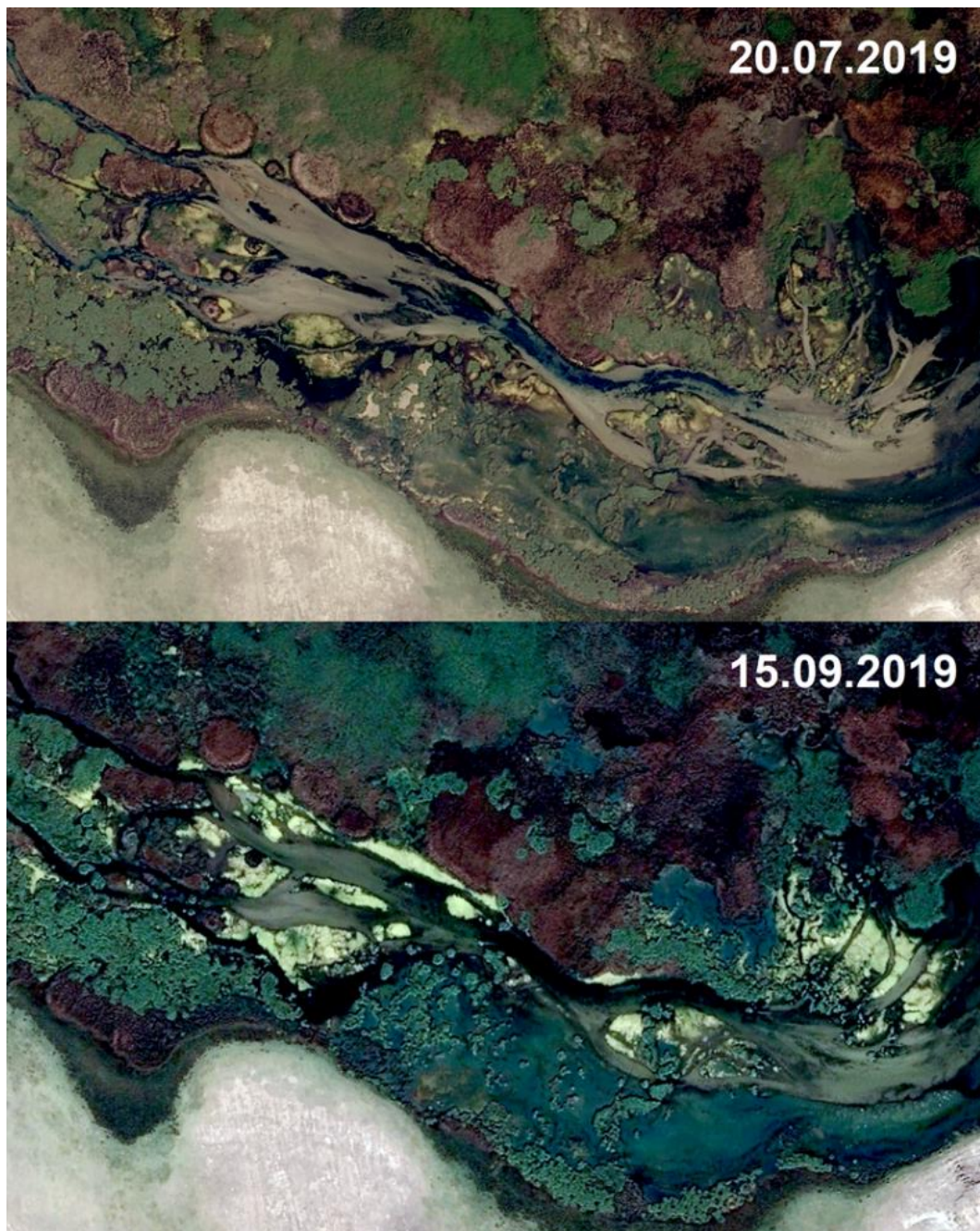


Figure 5.34 Comparison of orthophoto (above) vs. GE image (below)

The proposed abundance performance metric provides a straightforward understanding of the consistent pixel-based class distributions between the reference and estimated abundances. It is relatively easy to edit the *apm* algorithm so as to

indicate the rate of the total pixels consistent in terms of possessing two or more classes with the highest abundances within each pixel. The results for the optimized monotemporal dataset are given in Figure 5.35. As already mentioned, the *apm* points out that 72.90% of the total pixels are correctly estimated to have the same highest class proportion. Conversely, it can be interpreted as 27.10% of the reference pixels have a different highest class proportion compared to the unmixed pixels. The rate of consistent highest two classes is 27.41%. The figure also shows that the maximum number of classes in a single pixel is six since the last four *apm* values are equal, 7.57.

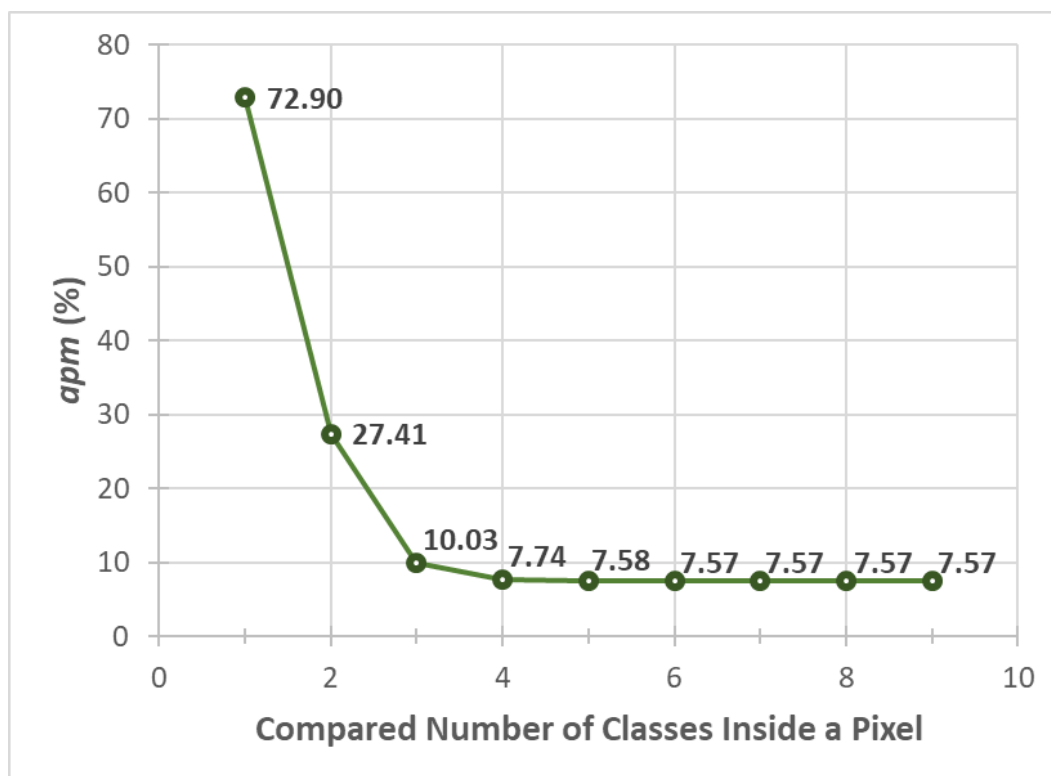


Figure 5.35 Calculated *apm* for optimized monotemporal data

The results for the optimized multitemporal dataset are given in Figure 5.36. It has similar rates as the monotemporal data apart from a slight decrease.



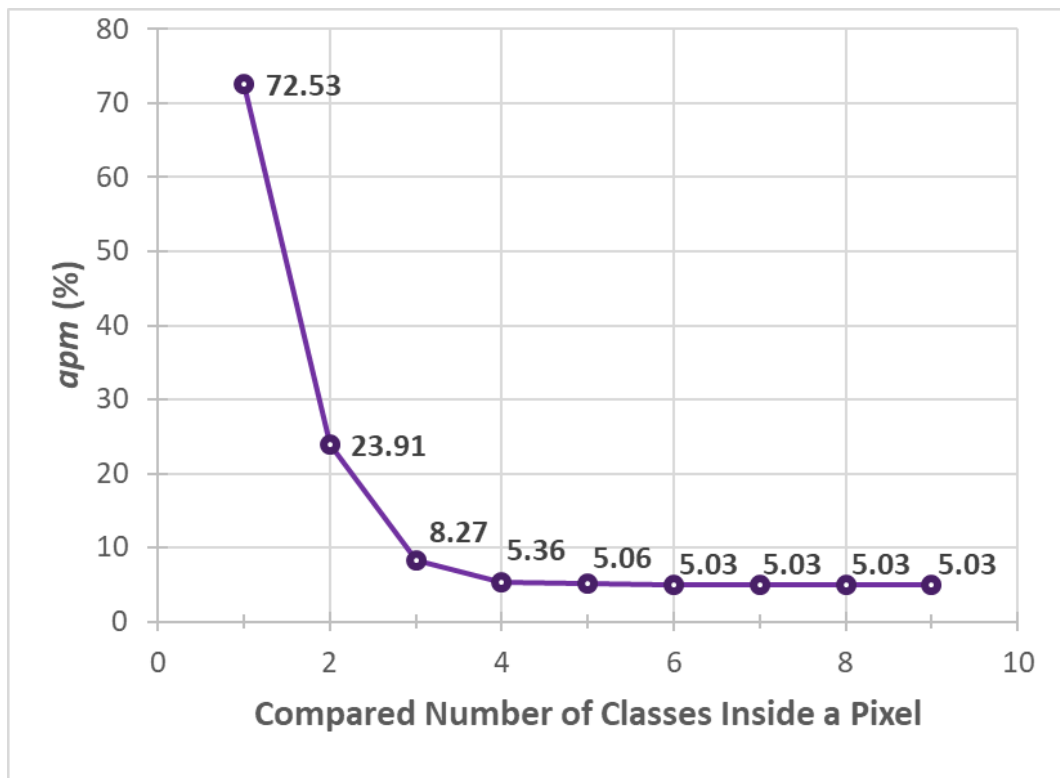


Figure 5.36 Calculated *apm* for optimized multitemporal data



## CHAPTER 6

### CONCLUSIONS AND RECOMMENDATIONS

#### 6.1 Conclusions

In this study, a framework is proposed for determining the extent of wetlands as a pre-processing step and then extracting their ground characteristics at the sub-pixel level. The study area is selected as Balıkdamı Wetland in Eskişehir. The Sentinel-2 L2A data are used in both pre-processing and unmixing phases.

The data download and preliminary geospatial investigations are conducted on the Google Earth Engine platform. Besides being a very versatile system, it is very potent in terms of processing vast amounts of remote sensing data rapidly and accurately since operations are conducted on the server-side.

To justify the necessity of co-registration, the ground truth is shifted for one pixel in the east direction since it is very likely to have an offset to such a degree in the satellite data. Then, its consistency is checked with its unshifted version through the determination of coefficient. The value of 0.72 suggests that a significant loss occurs if there is a misalignment. In this respect, four different algorithms are tested and compared. Although all methods provide similar outputs in terms of accuracy, Automated and Robust Open-Source Image Co-Registration Software (AROSICS) is primarily adopted due to its additional capabilities and practicality in working with crowded datasets.

The wetland extent is determined through the DTM and index-based stack regression. The DTM is introduced to extract the rough wetland bed. Then, stacked Sentinel-2 data are utilized in the double-sigmoid function fitting to enhance the rough wetland bed. Fine adjustments are performed via morphological operators.

The results demonstrate that the proposed method is very successful in predicting the extent with the sensitivity, specificity, precision, overall accuracy, and  $F_1$  score of 94.25%, 99.75%, 99.21%, 98.40%, and 96.67%, respectively. The algorithm does not count on high resolution DTM. The first phase is satisfactorily realized even with a rather old lower resolution surface model, the STRM.

Before moving on to the unmixing stage, the most relevant land cover types have to be chosen. The endmember selection, which might be the most crucial step of this study, is carried out with the help of a three-element ontology library. The inspection is done with respect to soil, vegetation, and water characteristics. Once the optimum number and land cover types of endmembers are determined using the ontology library, the training polygons are finalized. Since the training polygons are digitized on the high resolution orthophoto, pure pixels corresponding to the Sentinel-2 grid must be identified in order to extract the Sentinel-2 spectra of the endmembers correctly. In this regard, the spectral library is established precisely by the procedure explained in Section 4.5, which is implemented to detect pure pixels within training polygons and calculate endmember spectra.

The noise mitigation is applied to the test data by averaging available monthly images. Then, the band optimization procedure is implemented with the help of the reference data. In similar Sentinel-2 studies where a high resolution ground truth does not exist to be exploited for band optimization, the recommended band weights can be adopted as a first approximation since basic endmembers in natural habitats are likely to be similar to those in this thesis.

Subsequent to the band optimization, a fully constrained linear spectral unmixing method is performed on the monotemporal data. The  $OA$ ,  $\kappa$ ,  $R^2$ , and  $apm$  are calculated as 0.66, 0.56, 0.64, and 0.73, respectively. The noise mitigation approach supports the overall accuracy of about 3-4%, whereas optimized band weights using the overall accuracy as the cost function enhances the subject metrics in the order of 9%, 10%, 22%, and 9%, respectively.

The transition between classes follows particular patterns across the wetland. This study contributes to the determination of such patterns as well. One of the gradients observed in the study area, clearly seen in Figure 5.20, is shown schematically in Figure 6.1 as an example.

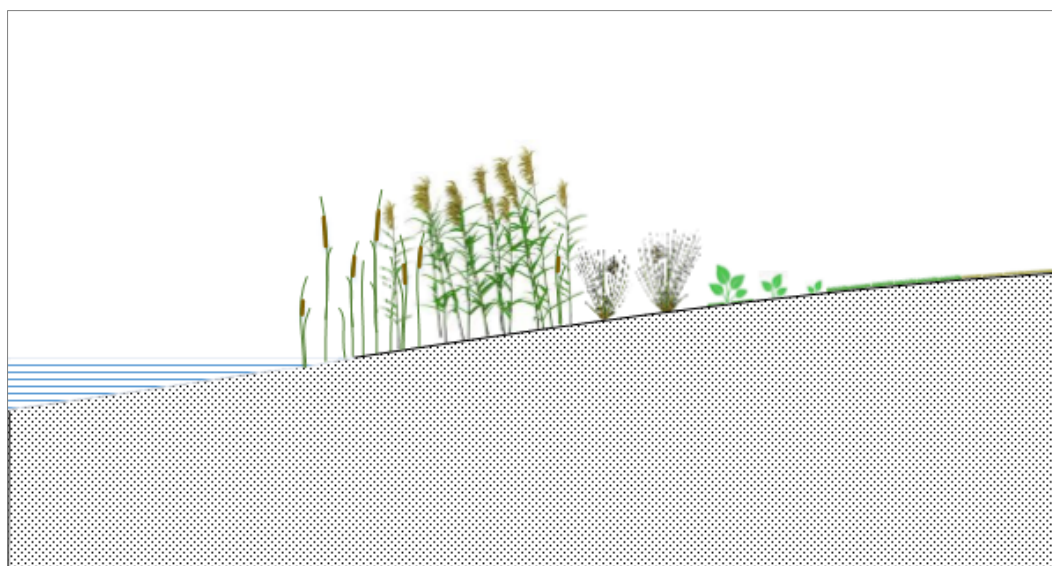


Figure 6.1 Vegetation gradient as a function of distance to lake: Typha, Phragmites, Juncus, Pasture, Steppe

For the temporal endmember case subject to spectro-temporal unmixing, the endmember optimization is proven to meet the deficit originating from seasonal anomalies. A similar degree of accuracy is achieved when applied with the aforementioned band weights. Furthermore, the trade-off between accuracy and temporality is highlighted.

One of the primary reasons for the confusion between classes is the incapability of the sensor's spectral resolution to define unique class spectra. Therefore, the use of hyperspectral data is superior at unmixing operations. Another related error source is the instrument's Point Spread Function (PSF). A significant portion of recorded radiance originates from neighboring pixels due to the PSF effect, whose adverse

effects penetrate surface information. Thus, special care should be taken to model PSF for better results. Although the overall accuracy of orthophoto classification is very high, it should be noted that absolute classification errors still exist.

The proposed Abundance Confusion Matrix (ACOMA) calculation proves its efficiency in the delicate assessment of fractional mapping. It helps researchers figure out the interactions between endmembers and interpret the phenomena that take place. The ACOMA requires a reference set to compare the estimates. This study handles the subject requirement by softening the classified high resolution orthophoto. The procedure implemented in Section 4.6 attains this aim with perfect precision.

The study provides an overall methodology for monitoring the wetlands relatively accurate using the Sentinel-2 images. In addition, the detectability of sparse cover classes is demonstrated. The proposed methodology enables the temporal analysis of wetlands to determine the effects of anthropogenic pressure and climate change on these precious ecosystems. The unmixing strategy is also applicable to other ecosystems.

## **6.2 Recommendations**

Balıkdamı can be considered a marsh-dominant, fair-sized inland wetland. In order to verify the robustness of the proposed methodology, the procedure should be tested on different types of wetlands such as swamps dominated by woody plants, bogs characterized by spongy peat deposits, acidic waters, and a thick carpet of sphagnum moss floor, and peat-forming fens nurtured by nutrients from sources other than precipitation. In addition, performance on a broader geographical extent should be investigated.

The unmixing approach is fundamentally designed for higher-dimensional data. This study utilizes open access multispectral imagery in an effort to keep the cost low;

nevertheless, experiments can be extended to include hyperspectral data to construct better endmember spectral signatures. It is worth learning the cost-performance trade-off when different data sources are introduced. An economical alternative might be the synergistic use of multispectral and open access radar data such as Sentinel-1. The positive impact of the fusing strategy on the hard classification of wetland studies is already mentioned in the introduction. Advantages of day and night capability, independency of weather conditions, and sensitivity to soil properties make the radar data appealing. On the other hand, to be able to use radar data in spectral unmixing, restraining properties based on a priori information are required to be designated.

In the case of having limited knowledge of endmembers or aiming to unmix particular endmembers, filters like Matched Filtering (MF) or Mixture-Tuned Matched Filtering (MTMF) can be applied beforehand. In case of having no endmember knowledge, either data reduction techniques can be applied, or methods like Gap Statistic, Elbow, Silhouette Coefficient, Calinski-Harabasz Index, Davies-Bouldin Index, and Bayesian Information Criterion can be adopted for approximation.

In this thesis, a consolidated spectral mixture model is implemented. As mentioned in Section 4.7, non-linear models, taking the endmember interactions into account, are worth to be tested due to their complex structure. Fan Model (Fan et al., 2009) based on the bilinear mixture approach is partially tested during the experiments. The version, including all possible cross-terms and the version narrowed down to a few apparent interactions, are introduced into the unmixing process. However, satisfactory results are not obtained. This effort should be elaborated and expanded so as to contain alternatives of the intimate mixture method.

Tracing the rise and fall of water levels has a moderate place in wetland management. Hydrodynamical, geomorphological, and ecological processes can be better understood by the characterization of wetland bathymetry. Satellite-derived

bathymetry is widely used accordingly. In this study, pseudo-bathymetric information extraction is tested using NDWI thresholding based on boxcar kernel smoothing. Figure 6.2 shows iso-NDWI polygons for the shallow water regions located in the north part. The outcomes are promising yet require further investigation and terrestrial validation.

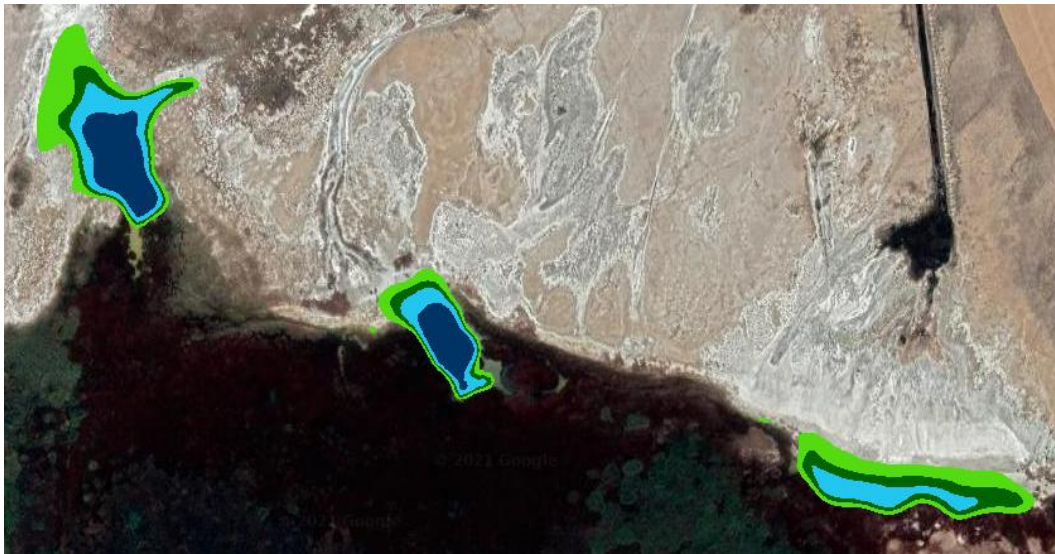


Figure 6.2 Preliminary outcomes of pseudo-bathymetric information extraction

Considering the fact that wetlands contain highly heterogeneous land cover, using the same reflectance value for four composing pixels owing to the Nearest Neighbor resampling algorithm remains incapable. Although this handicap is relieved with the help of band optimization, the pan-sharpening procedure can be applied for improved results. Due to the absence of a panchromatic band in the Sentinel-2 satellite, alternative solutions have been introduced by using or enhancing existing pan-sharpening techniques (Kaplan, 2018; Li et al., 2020; Park et al., 2017; Ronchetti and Sona, 2018; Wang et al., 2016), concluding significant improvements in comparison to the initial state. Apart from these approaches, super-resolution imaging based on neural networks has become popular to improve the imaging system resolution. The success of Sentinel-2 implementations has been demonstrated



by several studies (Brodu, 2017; Lanaras et al., 2017; Salgueiro et al., 2021). The technique proposed by Lanaras et al. (2017) is tested out on the mean monthly image used in the monotemporal unmixing stage. The result indicates that the initial overall accuracy of 57% escalates in the order of 3.5%. This increase is quite an improvement to be further investigated. The whole procedure is to be renewed in the future, including the optimization steps.

In the case of having reference abundances, from abundance to abundance estimation using Multivariate Random Forest can also be adopted rather than directly utilizing the reference data. The idea behind this approach is to estimate adjusted Sentinel-2 abundances from the reference abundance map. In order to obtain multi-output using an RF regressor, a separate RF model for each endmember is to be trained. A certain amount of the corresponding abundance values from reference data can be utilized as a training set during the model training. Then, each endmember's target abundance values for the study area are predicted using the relevant RF model on the test data. At the end of the procedure, as many single-band images as the total number of endmember are obtained, each of which has percentages of related class existence in its pixels. Finally, those individual images are combined in order to get a full map showing percentages of all class existences on each pixel. In theory, the sum of all bands for a pixel has to be one since it represents the distribution ratios of various classes. To check what happens in practice, the histogram for the summation of estimated abundances of each pixel can be plotted. Moreover, the number of trees and tree depths should be chosen small enough to prevent memorization for the Multivariate Random Forest method.

One thing is certain, which is to monitor these extraordinary habitats and take necessary precautions to prevent their degradation and destruction. Historical Google Earth images clearly show the massive degradation occurring in the past years (Figure 6.3). In order to avoid such damages, periodic checks should be realized and a robust warning mechanism should be established.



Figure 6.3 Images showing degradation of Balıkdamı at two-year intervals

## REFERENCES

- Abasolo, J.M., Machín, A.M., González, F.E., Ruiz, F.J.M., 2018. High Resolution Bathymetry of Littoral Zones Based on Very High-Resolution Worldview-2 Images.
- Agrafiotis, P., Skarlatos, D., Georgopoulos, A., Karantzalos, K., 2019. Shallow Water Bathymetry Mapping from UAV Imagery Based on Machine Learning, in: ISPRS Annals of the Photogrammetry, Remote Sensing and Spatial Information Sciences. pp. 9–16. <https://doi.org/10.5194/isprs-archives-XLII-2-W10-9-2019>
- Amani, M., Salehi, B., Mahdavi, S., Granger, J.E., Brisco, B., Hanson, A., 2017. Wetland Classification Using Multi-Source and Multi-Temporal Optical Remote Sensing Data in Newfoundland and Labrador, Canada. *Canadian Journal of Remote Sensing* 43, 360–373. <https://doi.org/10.1080/07038992.2017.1346468>
- Araya-López, R.A., Lopatin, J., Fassnacht, F.E., Hernández, H.J., 2018. Monitoring Andean high altitude wetlands in central Chile with seasonal optical data: A comparison between Worldview-2 and Sentinel-2 imagery. *ISPRS Journal of Photogrammetry and Remote Sensing* 145, 213–224. <https://doi.org/10.1016/j.isprsjprs.2018.04.001>
- Banks, S., White, L., Behnamian, A., Chen, Z., Montpetit, B., Brisco, B., Pasher, J., Duffe, J., 2019. Wetland Classification with Multi-Angle/Temporal SAR Using Random Forests. *Remote Sensing* 11, 670. <https://doi.org/10.3390/rs11060670>
- Bansal, S., Katyal, D., Garg, J.K., 2017. A novel strategy for wetland area extraction using multispectral MODIS data. *Remote Sensing of Environment* 200, 183–205. <https://doi.org/10.1016/j.rse.2017.07.034>
- Binaghi, E., Brivio, P.A., Ghezzi, P., Rampini, A., 1999. A fuzzy set-based accuracy assessment of soft classification. *Pattern Recognition Letters* 20, 935–948. [https://doi.org/10.1016/S0167-8655\(99\)00061-6](https://doi.org/10.1016/S0167-8655(99)00061-6)

- Bioucas-Dias, J.M., Figueiredo, M.A.T., 2010. Alternating direction algorithms for constrained sparse regression: Application to hyperspectral unmixing, in: 2010 2nd Workshop on Hyperspectral Image and Signal Processing: Evolution in Remote Sensing. pp. 1–4. <https://doi.org/10.1109/WHISPERS.2010.5594963>
- Brigot, G., Colin-Koeniguer, E., Plyer, A., Janez, F., 2016. Adaptation and Evaluation of an Optical Flow Method Applied to Coregistration of Forest Remote Sensing Images. *IEEE Journal of Selected Topics in Applied Earth Observations and Remote Sensing* 9, 2923–2939. <https://doi.org/10.1109/JSTARS.2016.2578362>
- Brodu, N., 2017. Super-Resolving Multiresolution Images with Band-Independent Geometry of Multispectral Pixels. *IEEE Transactions on Geoscience and Remote Sensing* 55, 4610–4617. <https://doi.org/10.1109/TGRS.2017.2694881>
- Byrd, R.H., Hribar, M.E., Nocedal, J., 1999. An Interior Point Algorithm for Large-Scale Nonlinear Programming. *SIAM J. Optim.* 9, 877–900. <https://doi.org/10.1137/S1052623497325107>
- Caballero, I., Stumpf, R.P., 2019. Retrieval of nearshore bathymetry from Sentinel-2A and 2B satellites in South Florida coastal waters. *Estuarine, Coastal and Shelf Science* 226, 106277. <https://doi.org/10.1016/j.ecss.2019.106277>
- Capital Regional District, 2008. Water in Our Community. CRD, Victoria, British Columbia.
- Casal, G., Monteys, X., Hedley, J., Harris, P., Cahalane, C., McCarthy, T., 2019. Assessment of empirical algorithms for bathymetry extraction using Sentinel-2 data. *International Journal of Remote Sensing* 40, 2855–2879. <https://doi.org/10.1080/01431161.2018.1533660>
- Chang, M., Meng, X., Sun, W., Yang, G., Peng, J., 2021. Collaborative Coupled Hyperspectral Unmixing Based Subpixel Change Detection for Analyzing Coastal Wetlands. *IEEE Journal of Selected Topics in Applied Earth Observations and Remote Sensing* 14, 8208–8224. <https://doi.org/10.1109/JSTARS.2021.3104164>

- Chang, N.-B., Bai, K., 2018. Multisensor Data Fusion and Machine Learning for Environmental Remote Sensing. <https://doi.org/10.1201/9781315154602>
- Chen, B., Chen, L., Huang, B., Michishita, R., Xu, B., 2018. Dynamic monitoring of the Poyang Lake wetland by integrating Landsat and MODIS observations. *ISPRS Journal of Photogrammetry and Remote Sensing* 139, 75–87. <https://doi.org/10.1016/j.isprsjprs.2018.02.021>
- Chen, B., Chen, L., Lu, M., Xu, B., 2017. Wetland mapping by fusing fine spatial and hyperspectral resolution images. *Ecological Modelling* 353, 95–106. <https://doi.org/10.1016/j.ecolmodel.2017.01.004>
- Daniela, R., Patrick, t.B., Andrew, F., Tomas, B., David, C., Johannes, F., Ritesh, K., Nick, D., 2013. *The Economics of Ecosystems and Biodiversity for Water and Wetlands*. Institute for European Environmental Policy, London and Brussels.
- David, L., Llinas, J., 2001. *Handbook of Multisensor Data Fusion*. CRC Press.
- Davidson, N., 2014. How much wetland has the world lost? Long-term and recent trends in global wetland area. *Marine and Freshwater Research* 65, 936–941. <https://doi.org/10.1071/MF14173>
- Ding, J., Na, X., Li, X., 2021. Wetland Classification Using Sparse Spectral Unmixing Algorithm and Landsat 8 OLI Imagery BT - *Spatial Data and Intelligence*, in: Pan, G., Lin, H., Meng, X., Gao, Y., Li, Y., Guan, Q., Ding, Z. (Eds.), . Springer International Publishing, Cham, pp. 186–194.
- Dobigeon, N., Altmann, Y., Brun, N., Moussaoui, S., 2016. Linear and Nonlinear Unmixing in Hyperspectral Imaging. *Data Handling in Science and Technology* 30, 185–224. <https://doi.org/10.1016/B978-0-444-63638-6.00006-1>
- Domínguez-Beisiegel, M., Castañeda, C., Mougnot, B., Herrero, J., 2016. Analysis and Mapping of the Spectral Characteristics of Fractional Green Cover in Saline Wetlands (NE Spain) Using Field and Remote Sensing Data. *Remote Sensing* 8, 590. <https://doi.org/10.3390/rs8070590>

- Dörnhöfer, K., Göritz, A., Gege, P., Pflug, B., Oppelt, N., 2016. Water Constituents and Water Depth Retrieval from Sentinel-2A—A First Evaluation in an Oligotrophic Lake. *Remote Sensing* 8, 941. <https://doi.org/10.3390/rs8110941>
- Doughty, C., Cavanaugh, K., 2019. Mapping Coastal Wetland Biomass from High Resolution Unmanned Aerial Vehicle (UAV) Imagery. *Remote Sensing* 11, 540. <https://doi.org/10.3390/rs11050540>
- Duplančić-Leder, T., Leder, N., Peroš, J., 2019. Satellite Derived Bathymetry Survey Method - Example of Hramina Bay. *Transactions on Maritime Science* 8, 99–108. <https://doi.org/10.7225/toms.v08.n01.010>
- Ebaid, H.M., Abdalla, D.S., Soliman, M.A., 2018. Derivation of Bathymetry Models for Shallow Water Using Multispectral Sentinel-2A Images for Delta Coast of Egypt. *Research Journal of Applied Sciences, Engineering and Technology* 15, 81–90. <https://doi.org/10.19026/rjaset.15.5418>
- Emami, H., Mojaradi, B., 2009. A New Method for Accuracy Assessment of Sub-Pixel Classification Results. *American Journal of Engineering and Applied Sciences* 2, 456–465.
- Eskişehir Metropolitan Municipality, 2020. Eskişehir İstatistikleri 2019 [Eskişehir Statistics 2019]. Eskişehir Büyükşehir Belediyesi, Eskişehir.
- Eugenio, F., Martin, J., Marcello, J., Bermejo, J.A., 2013. Worldview-2 high resolution remote sensing image processing for the monitoring of coastal areas, in: *European Signal Processing Conference*. p. 5.
- European Space Agency, 2022a. Sentinel-2 - Missions [WWW Document]. URL <https://sentinels.copernicus.eu/web/sentinel/missions/sentinel-2> (accessed 1.1.22).
- European Space Agency, 2022b. STEP – Science Toolbox Exploitation Platform [WWW Document]. URL <http://step.esa.int/main/> (accessed 1.1.22).
- European Space Agency, 2021. Sentinel-2 MSI User Guide.

- European Space Agency, 2015. ESA's Optical High-Resolution Mission for GMES Operational Services.
- Fan, W., Hu, B., Miller, J., Li, M., 2009. Comparative study between a new nonlinear model and common linear model for analysing laboratory simulated-forest hyperspectral data. *International Journal of Remote Sensing* 30, 2951–2962. <https://doi.org/10.1080/01431160802558659>
- Finlayson, C.M., Milton, G.R., Prentice, C., Davidson, N.C. (Eds.), 2018. *The Wetland Book II: Distribution, Description, and Conservation*. Springer Netherlands, Dordrecht.
- Foody, G.M., 1996. Approaches for the production and evaluation of fuzzy land cover classifications from remotely-sensed data. *International Journal of Remote Sensing* 17, 1317–1340. <https://doi.org/10.1080/01431169608948706>
- Foody, G.M., Trodd, N.M., 1993. Non-Classificatory Analysis and Representation of Heathland Vegetation from Remotely Sensed Imagery. *GeoJournal* 29, 343–350.
- Fu, B., Wang, Y., Campbell, A., Li, Y., Zhang, B., Yin, S., Xing, Z., Jin, X., 2017. Comparison of object-based and pixel-based Random Forest algorithm for wetland vegetation mapping using high spatial resolution GF-1 and SAR data. *Ecological Indicators* 73, 105–117. <https://doi.org/10.1016/j.ecolind.2016.09.029>
- Gardner, R.C., Barchiesi, S., Beltrame, C., Finlayson, C.M., Galewski, T., Harrison, I., Paganini, M., Perennou, C., Pritchard, D., Rosenqvist, A., Walpole, M., 2015. State of the World's Wetlands and Their Services to People: A Compilation of Recent Analyses. *SSRN Electronic Journal*. <https://doi.org/10.2139/ssrn.2589447>
- General Directorate of State Hydraulic Works, 2018. 2015 Akım Gözlem Yılığ [2015 Hydrological Yearbook]. DSİ, Ankara.
- Groww, 2022. Rushes (Juncus): growing, planting, caring. [WWW Document]. URL <https://www.groww.fr/en/plants/rushes> (accessed 1.1.22).

- Gumbrecht, T., Roman-Cuesta, R.M., Verchot, L., Herold, M., Wittmann, F., Householder, E., Herold, N., Murdiyarso, D., 2017. An expert system model for mapping tropical wetlands and peatlands reveals South America as the largest contributor. *Global Change Biology* 23, 3581–3599. <https://doi.org/10.1111/gcb.13689>
- Hu, S., Niu, Z., Chen, Y., Li, L., Zhang, H., 2017. Global wetlands: Potential distribution, wetland loss, and status. *Science of The Total Environment* 586, 319–327. <https://doi.org/10.1016/j.scitotenv.2017.02.001>
- Hui, F., Xu, B., Huang, H., Yu, Q., Gong, P., 2008. Modelling spatial-temporal change of Poyang Lake using multitemporal Landsat imagery. *International Journal of Remote Sensing* 29, 5767–5784. <https://doi.org/10.1080/01431160802060912>
- IDB Project, 2022. IDB - Index: Tasselled Cap - wetness [WWW Document]. Index DataBase. URL <https://www.indexdatabase.de/db/i-single.php?id=93> (accessed 1.1.22).
- Iordache, M.-D., Bioucas-Dias, J.M., Plaza, A., 2011. Sparse Unmixing of Hyperspectral Data. *IEEE Transactions on Geoscience and Remote Sensing* 49, 2014–2039. <https://doi.org/10.1109/TGRS.2010.2098413>
- Jakovljević, G., Govedarica, M., Álvarez-Taboada, F., 2019. Waterbody mapping: a comparison of remotely sensed and GIS open data sources. *International Journal of Remote Sensing* 40, 2936–2964. <https://doi.org/10.1080/01431161.2018.1538584>
- Jarchow, C.J., Sigafus, B.H., Muths, E., Hossack, B.R., 2020. Using Full and Partial Unmixing Algorithms to Estimate the Inundation Extent of Small, Isolated Stock Ponds in an Arid Landscape. *Wetlands* 40, 563–575. <https://doi.org/10.1007/s13157-019-01201-7>
- Ji, W. (Ed.), 2008. *Wetland and Water Resource Modeling and Assessment - A Watershed Perspective*, 1st Edition. CRC Press, Boca Raton. <https://doi.org/10.1201/9781420064155>



- Kakuta, S., Ariyasu, E., Takeda, T., 2018. Shallow Water Bathymetry Mapping Using Hyperspectral Data, in: IGARSS 2018 - 2018 IEEE International Geoscience and Remote Sensing Symposium. IEEE, pp. 1539–1542. <https://doi.org/10.1109/IGARSS.2018.8518386>
- Kaplan, G., 2018. Sentinel-2 Pan Sharpening - Comparative Analysis. Proceedings 2. <https://doi.org/10.3390/ecrs-2-05158>
- Kaplan, G., Avdan, U., 2019. Evaluating the utilization of the red edge and radar bands from sentinel sensors for wetland classification. *Catena* 178, 109–119. <https://doi.org/10.1016/j.catena.2019.03.011>
- Kaplan, G., Avdan, U., 2018. Sentinel-1 and Sentinel-2 data fusion for wetlands mapping: Balıkdami, Turkey, in: International Archives of the Photogrammetry, Remote Sensing and Spatial Information Sciences - ISPRS Archives. International Society for Photogrammetry and Remote Sensing, pp. 729–734. <https://doi.org/10.5194/isprs-archives-XLII-3-729-2018>
- Kaplan, G., Yigit Avdan, Z., Avdan, U., 2019. Mapping and Monitoring Wetland Dynamics Using Thermal, Optical, and SAR Remote Sensing Data, in: Gökçe, D. (Ed.), *Wetlands Management - Assessing Risk and Sustainable Solutions*. IntechOpen.
- Keddy, P.A., 2010. *Wetland ecology: principles and conservation*. Cambridge University Press.
- Khajehrayeni, F., Ghassemian, H., 2020. Hyperspectral Unmixing Using Deep Convolutional Autoencoders in a Supervised Scenario. *IEEE Journal of Selected Topics in Applied Earth Observations and Remote Sensing* 13, 567–576. <https://doi.org/10.1109/JSTARS.2020.2966512>
- Khangarot, L.S., Ghosh, S.K., Dwivedi, R.K., 2016. Assessment of accuracy for soft classification: SCAASFER as a tool, in: 2016 International Conference System Modeling & Advancement in Research Trends (SMART). pp. 90–97. <https://doi.org/10.1109/SYSMART.2016.7894497>
- Klein, L.A., 2012. *Sensor and data fusion: A tool for information assessment and decision making: Second edition*. <https://doi.org/10.1117/3.928035>

- Koch, K.R., 1999. *Parameter Estimation and Hypothesis Testing in Linear Models*. Springer.
- Koyuncu, O., Ataslar, E., Tokur, S., Erten, M.E., Ardic, M., 2008. The Flora of Balıkdamı Wetland and Its Surroundings (Sivrihisar, Eskişehir - Turkey). *Turkish Journal of Botany* 32, 227–241.
- Lanaras, C., Bioucas-Dias, J., Baltsavias, E., Schindler, K., 2017. Super-Resolution of Multispectral Multiresolution Images from a Single Sensor, in: 2017 IEEE Conference on Computer Vision and Pattern Recognition Workshops (CVPRW). pp. 1505–1513. <https://doi.org/10.1109/CVPRW.2017.194>
- Leadley, P.W., Krug, C.B., Alkemade, R., Pereira, H.M., Sumaila, U.R., Walpole, M., Marques, A., Newbold, T., Teh, L.S.L., van Kolck, J., Bellard, C., Januchowski-Hartley, S.R., Mumby, P.J., 2014. Progress towards the Aichi Biodiversity Targets: An Assessment of Biodiversity Trends, Policy Scenarios and Key Actions (No. 78), Technical Series. Secretariat of the Convention on Biological Diversity, Montreal, Canada.
- Lefebvre, G., Davranche, A., Willm, L., Campagna, J., Redmond, L., Merle, C., Guelmami, A., Poulin, B., 2019. Introducing WIW for Detecting the Presence of Water in Wetlands with Landsat and Sentinel Satellites. *Remote Sensing* 11, 2210. <https://doi.org/10.3390/rs11192210>
- Lewis, H.G., Brown, M., 2001. A generalized confusion matrix for assessing area estimates from remotely sensed data. *ISPRS J. Photogramm. Remote Sens.* 22, 3223–3235. <https://doi.org/10.1080/01431160152558332>
- Li, J., Bioucas-Dias, J.M., Plaza, A., 2012. Collaborative nonnegative matrix factorization for remotely sensed hyperspectral unmixing, in: 2012 IEEE International Geoscience and Remote Sensing Symposium. pp. 3078–3081. <https://doi.org/10.1109/IGARSS.2012.6350775>
- Li, L., Chen, Y., Xu, T., Shi, K., Liu, R., Huang, C., Lu, B., Meng, L., 2019. Remote Sensing of Wetland Flooding at a Sub-Pixel Scale Based on Random Forests and Spatial Attraction Models. *Remote Sensing* 11, 1231. <https://doi.org/10.3390/rs11101231>

- Li, Z., Zhang, H.K., Roy, D.P., Yan, L., Huang, H., 2020. Sharpening the Sentinel-2 10 and 20 m Bands to PlanetScope-0.3 m Resolution. *Remote Sensing* 12. <https://doi.org/10.3390/rs12152406>
- Lillesand, T., Kiefer, R., Chipman, J., 2015. *Remote sensing and image interpretation* Seventh Ed. John Wiley and Sons, Inc., New York 736.
- Lopez, R.D., Lyon, J.G., Lyon, L.K., Lopez, D.K., 2013. *Wetland Landscape Characterization: Practical Tools, Methods, and Approaches for Landscape Ecology*, Second Edition. CRC Press, Boca Raton. <https://doi.org/10.1201/b14057>
- López-Tapia, S., Ruiz, P., Smith, M., Matthews, J., Zercher, B., Sydorenko, L., Varia, N., Jin, Y., Wang, M., Dunn, J.B., Katsaggelos, A.K., 2021. Machine learning with high-resolution aerial imagery and data fusion to improve and automate the detection of wetlands. *International Journal of Applied Earth Observation and Geoinformation* 105, 102581. <https://doi.org/10.1016/j.jag.2021.102581>
- Ludwig, C., Walli, A., Schleicher, C., Weichselbaum, J., Riffler, M., 2019. A highly automated algorithm for wetland detection using multi-temporal optical satellite data. *Remote Sensing of Environment* 224, 333–351. <https://doi.org/10.1016/j.rse.2019.01.017>
- Lyon, J.G., 2001. *Wetland landscapes characterisation: GIS, remote sensing, and image analysis*. Ann Arbor Press, Chelsea.
- Mahdavi, S., Salehi, B., Amani, M., Granger, J., Brisco, B., Huang, W., 2019. A dynamic classification scheme for mapping spectrally similar classes: Application to wetland classification. *International Journal of Applied Earth Observation and Geoinformation* 83, 101914. <https://doi.org/10.1016/j.jag.2019.101914>
- Mallick, J., Talukdar, S., Shahfahad, Pal, S., Rahman, A., 2021. A novel classifier for improving wetland mapping by integrating image fusion techniques and ensemble machine learning classifiers. *Ecological Informatics* 65, 101426. <https://doi.org/10.1016/j.ecoinf.2021.101426>

- Ministry of Agriculture and Forestry of Republic of Turkey, 2022. Sulak Alanlar [Wetlands] [WWW Document]. T.C. Tarım ve Orman Bakanlığı. URL <https://www.tarimorman.gov.tr/DKMP/Menu/31/Sulak-Alanlar> (accessed 1.1.22).
- Mishra, B., Shahi, T.B., 2021. Deep learning-based framework for spatiotemporal data fusion: an instance of Landsat 8 and Sentinel 2 NDVI. *Journal of Applied Remote Sensing* 15, 1–13. <https://doi.org/10.1117/1.JRS.15.034520>
- Mitchell, H.B., 2012. Data fusion: Concepts and ideas, *Data Fusion: Concepts and Ideas*. Springer Berlin Heidelberg. <https://doi.org/10.1007/978-3-642-27222-6>
- Mitsch, W., Gosselink, J., 2015. *Wetlands*, 5th edition.
- Montgomery, J., Brisco, B., Chasmer, L., Devito, K., Cobbaert, D., Hopkinson, C., 2019. SAR and lidar temporal data fusion approaches to boreal wetland ecosystem monitoring. *Remote Sensing* 11, 161. <https://doi.org/10.3390/rs11020161>
- Mooney, H.A., Cropper, A., Leemans, R., Arico, S., Bridgewater, P., Peterson, G., Revenga, C., Rivera, M., Peter, A.W., 2005. *Ecosystems and Human Well-being: Wetlands and Water Synthesis*. World Resources Institute, Washington DC.
- Moore, P.D., Garratt, R., 2006. *Wetlands (Biomes of the Earth)*. Chelsea House.
- Moré, J.J., Sorensen, D.C., 1983. Computing a Trust Region Step. *SIAM J. Sci. and Stat. Comput.* 4, 553–572. <https://doi.org/10.1137/0904038>
- Myre, J.M., Frahm, E., Lilja, D.J., Saar, M.O., 2017. TNT-NN: A Fast Active Set Method for Solving Large Non-Negative Least Squares Problems. *Procedia Computer Science* 108, 755–764. <https://doi.org/10.1016/j.procs.2017.05.194>
- Na, X., Li, X., Li, W., Wu, C., 2021. Wetland Mapping Using HJ-1A/B Hyperspectral Images and an Adaptive Sparse Constrained Least Squares Linear Spectral Mixture Model. *Remote Sensing* 13. <https://doi.org/10.3390/rs13040751>

- Nocedal, J., Wright, S., 2006. Numerical Optimization, Springer Series in Operations Research and Financial Engineering. Springer New York.
- Ordoyne, C., Friedl, M.A., 2008. Using MODIS data to characterize seasonal inundation patterns in the Florida Everglades. *Remote Sensing of Environment* 112, 4107–4119. <https://doi.org/10.1016/j.rse.2007.08.027>
- Özdemir, A., Leloğlu, U.M., 2014. Bathymetry and water quality measurement of shallow waters using hyperion: Serçin lake, in: 2014 22nd Signal Processing and Communications Applications Conference (SIU). pp. 2023–2026. <https://doi.org/10.1109/SIU.2014.6830656>
- Ozkazanc, N., Ozay, E., Ozcan, A., 2019. Ornithofauna of Balıkdamı Wildlife Development Area. *Turkish Journal of Forestry* 20, 341–351. <https://doi.org/10.18182/tjf.570107>
- Park, H., Choi, J., Park, N., Choi, S., 2017. Sharpening the VNIR and SWIR Bands of Sentinel-2A Imagery through Modified Selected and Synthesized Band Schemes. *Remote Sensing* 9. <https://doi.org/10.3390/rs9101080>
- Poursanidis, D., Traganos, D., Reinartz, P., Chrysoulakis, N., 2019. On the use of Sentinel-2 for coastal habitat mapping and satellite-derived bathymetry estimation using downscaled coastal aerosol band. *International Journal of Applied Earth Observation and Geoinformation* 80, 58–70. <https://doi.org/10.1016/j.jag.2019.03.012>
- Rafferty, J., 2011. The Living Earth: Lakes and Wetlands. Britannica Educational Pub. in association with Rosen Educational Services.
- Ramsar Convention Secretariat, 2022. Homepage | Ramsar [WWW Document]. Ramsar. URL <https://www.ramsar.org/> (accessed 1.1.22).
- Ramsar Convention Secretariat, 2017. Wetlands, Discover an ecosystem important for life. *Wetlands Guidebook* 9–9.
- Ramsar Convention Secretariat, 2013. The Ramsar Convention Manual, 6th edition. The Ramsar Convention Manual: a guide to the Convention on Wetlands (Ramsar, Iran, 1971) 109–109.

- Ramsar Convention Secretariat, 2010. Wetlands: A global disappearing act 2–2.
- Rapinel, S., Fabre, E., Dufour, S., Arvor, D., Mony, C., Hubert-Moy, L., 2019. Mapping potential, existing and efficient wetlands using free remote sensing data. *Journal of Environmental Management* 247, 829–839. <https://doi.org/10.1016/j.jenvman.2019.06.098>
- Reddy, K.R., DeLaune, R.D., 2008. Biogeochemistry of wetlands: science and applications. CRC Press.
- Ronchetti, G., Sona, G., 2018. Pan-sharpening methods applied on Sentinel-2 imagery for mapping inland water bodies, in: EGU2018. Vienna, Austria, p. p.7760.
- Russo, R.E. (Ed.), 2008. Wetlands: Ecology, Conservation and Restoration. Nova Science Publishers, New York.
- Salehi, B., Mahdianpari, M., Amani, M., M. Manesh, F., Granger, J., Mahdavi, S., Brisco, B., 2019. A Collection of Novel Algorithms for Wetland Classification with SAR and Optical Data, in: Gökçe, D. (Ed.), Wetlands Management - Assessing Risk and Sustainable Solutions. IntechOpen.
- Salgueiro, L., Marcello, J., Vilaplana, V., 2021. Single-Image Super-Resolution of Sentinel-2 Low Resolution Bands with Residual Dense Convolutional Neural Networks. *Remote Sensing* 13. <https://doi.org/10.3390/rs13245007>
- Scheffler, D., Hollstein, A., Diedrich, H., Segl, K., Hostert, P., 2017. AROSICS: An Automated and Robust Open-Source Image Co-Registration Software for Multi-Sensor Satellite Data. *Remote Sensing* 9. <https://doi.org/10.3390/rs9070676>
- Scholz, M., 2016. Wetlands for Water Pollution Control. Elsevier. <https://doi.org/10.1016/c2015-0-00156-3>
- Shen, X., Liu, B., Xue, Z., Jiang, M., Lu, X., Zhang, Q., 2019. Spatiotemporal variation in vegetation spring phenology and its response to climate change in freshwater marshes of Northeast China. *Science of The Total Environment* 666, 1169–1177. <https://doi.org/10.1016/j.scitotenv.2019.02.265>

- Silván-Cárdenas, J.L., Wang, L., 2008. Sub-pixel confusion-uncertainty matrix for assessing soft classifications. *Remote Sensing of Environment* 112, 1081–1095. <https://doi.org/10.1016/j.rse.2007.07.017>
- Stehman, S.V., Arora, M.K., Kasetkasem, T., Varshney, P.K., 2007. Estimation of fuzzy error matrix accuracy measures under stratified random sampling. *Photogrammetric Engineering and Remote Sensing* 73, 165–173. <https://doi.org/10.14358/PERS.73.2.165>
- Stratoulías, D., Balzter, H., Zlinszky, A., Tóth, V.R., 2018. A comparison of airborne hyperspectral-based classifications of emergent wetland vegetation at Lake Balaton, Hungary. *International Journal of Remote Sensing* 39, 5689–5715. <https://doi.org/10.1080/01431161.2018.1466081>
- Sun, N., Zhu, W., Cheng, Q., 2018. GF-1 and Landsat observed a 40-year wetland spatiotemporal variation and its coupled environmental factors in Yangtze River estuary. *Estuarine, Coastal and Shelf Science* 207, 30–39. <https://doi.org/10.1016/j.ecss.2018.03.022>
- Tiner, R.W., Lang, M.W., Klemas, V. V (Eds.), 2015. *Remote Sensing of Wetlands - Applications and Advances*, 1st Edition. ed. CRC Press, Boca Raton.
- Traganos, D., Poursanidis, D., Aggarwal, B., Chrysoulakis, N., Reinartz, P., 2018. Estimating Satellite-Derived Bathymetry (SDB) with the Google Earth Engine and Sentinel-2. *Remote Sensing* 10, 859. <https://doi.org/10.3390/rs10060859>
- Vanderhoof, M.K., Alexander, L.C., Todd, M.J., 2016. Temporal and spatial patterns of wetland extent influence variability of surface water connectivity in the Prairie Pothole Region, United States. *Landscape Ecology* 31, 805–824. <https://doi.org/10.1007/s10980-015-0290-5>
- Verhoeven, J.T.A., Beltman, B., Bobbink, R., Whigham, D.F., 2006. *Wetlands and Natural Resource Management*, Journal of Chemical Information and Modeling, Ecological Studies. Springer Berlin Heidelberg, Berlin, Heidelberg. <https://doi.org/10.1007/978-3-540-33187-2>

- Vilar, P., Moura, A., Guerreiro, R., Lamas, L., Pinto, J.P., 2018. Coastal water bathymetry retrieval using high-resolution remote sensing data, in: Bostater, C.R., Mertikas, S.P., Neyt, X. (Eds.), *Remote Sensing of the Ocean, Sea Ice, Coastal Waters, and Large Water Regions* 2018. SPIE, p. 7. <https://doi.org/10.1117/12.2324466>
- Wang, F., 1990. Improving remote sensing image analysis through fuzzy information representation. *Photogrammetric Engineering & Remote Sensing* 56, 1163–1168.
- Wang, Q., Shi, W., Li, Z., Atkinson, P.M., 2016. Fusion of Sentinel-2 images. *Remote Sensing of Environment* 187, 241–252. <https://doi.org/10.1016/j.rse.2016.10.030>
- Wang, X., Zhang, F., Kung, H., Johnson, V.C., 2018. New methods for improving the remote sensing estimation of soil organic matter content (SOMC) in the Ebinur Lake Wetland National Nature Reserve (ELWNNR) in northwest China. *Remote Sensing of Environment* 218, 104–118. <https://doi.org/10.1016/j.rse.2018.09.020>
- Whyte, A., Ferentinos, K.P., Petropoulos, G.P., 2018. A new synergistic approach for monitoring wetlands using Sentinels -1 and 2 data with object-based machine learning algorithms. *Environmental Modelling & Software* 104, 40–54. <https://doi.org/10.1016/j.envsoft.2018.01.023>
- Wikipedia Contributors, 2022. Wikipedia [WWW Document]. Wikipedia, the free encyclopedia. URL <https://en.wikipedia.org/> (accessed 1.1.22).
- Xiaoping, W., Fei, Z., Hsiang-te, K., Haiyang, Y., 2017. Spectral response characteristics and identification of typical plant species in Ebinur lake wetland national nature reserve (ELWNNR) under a water and salinity gradient. *Ecological Indicators* 81, 222–234. <https://doi.org/10.1016/j.ecolind.2017.05.071>
- Yan, G., Li, L., Coy, A., Mu, X., Chen, S., Xie, D., Zhang, W., Shen, Q., Zhou, H., 2019. Improving the estimation of fractional vegetation cover from UAV RGB imagery by colour unmixing. *ISPRS Journal of Photogrammetry and Remote Sensing* 158, 23–34. <https://doi.org/10.1016/j.isprsjprs.2019.09.017>



- Yang, R.-M., Guo, W.-W., Zheng, J.-B., 2019. Soil prediction for coastal wetlands following *Spartina alterniflora* invasion using Sentinel-1 imagery and structural equation modeling. *Catena* 173, 465–470. <https://doi.org/10.1016/j.catena.2018.10.045>
- Yunus, A.P., Jie, D., Song, X., Avtar, R., 2019. High Resolution Sentinel-2 Images for Improved Bathymetric Mapping of Coastal and Lake Environments. *Earth Sciences*.
- Zhu, X., Helmer, E.H., Gao, F., Liu, D., Chen, J., Lefsky, M.A., 2016. A flexible spatiotemporal method for fusing satellite images with different resolutions. *Remote Sensing of Environment*. <https://doi.org/10.1016/j.rse.2015.11.016>
- Zhu, X., Hou, Y., Weng, Q., Chen, L., 2019. Integrating UAV optical imagery and LiDAR data for assessing the spatial relationship between mangrove and inundation across a subtropical estuarine wetland. *ISPRS Journal of Photogrammetry and Remote Sensing* 149, 146–156. <https://doi.org/10.1016/j.isprsjprs.2019.01.021>



## APPENDICES

### A. Site Visit Observations

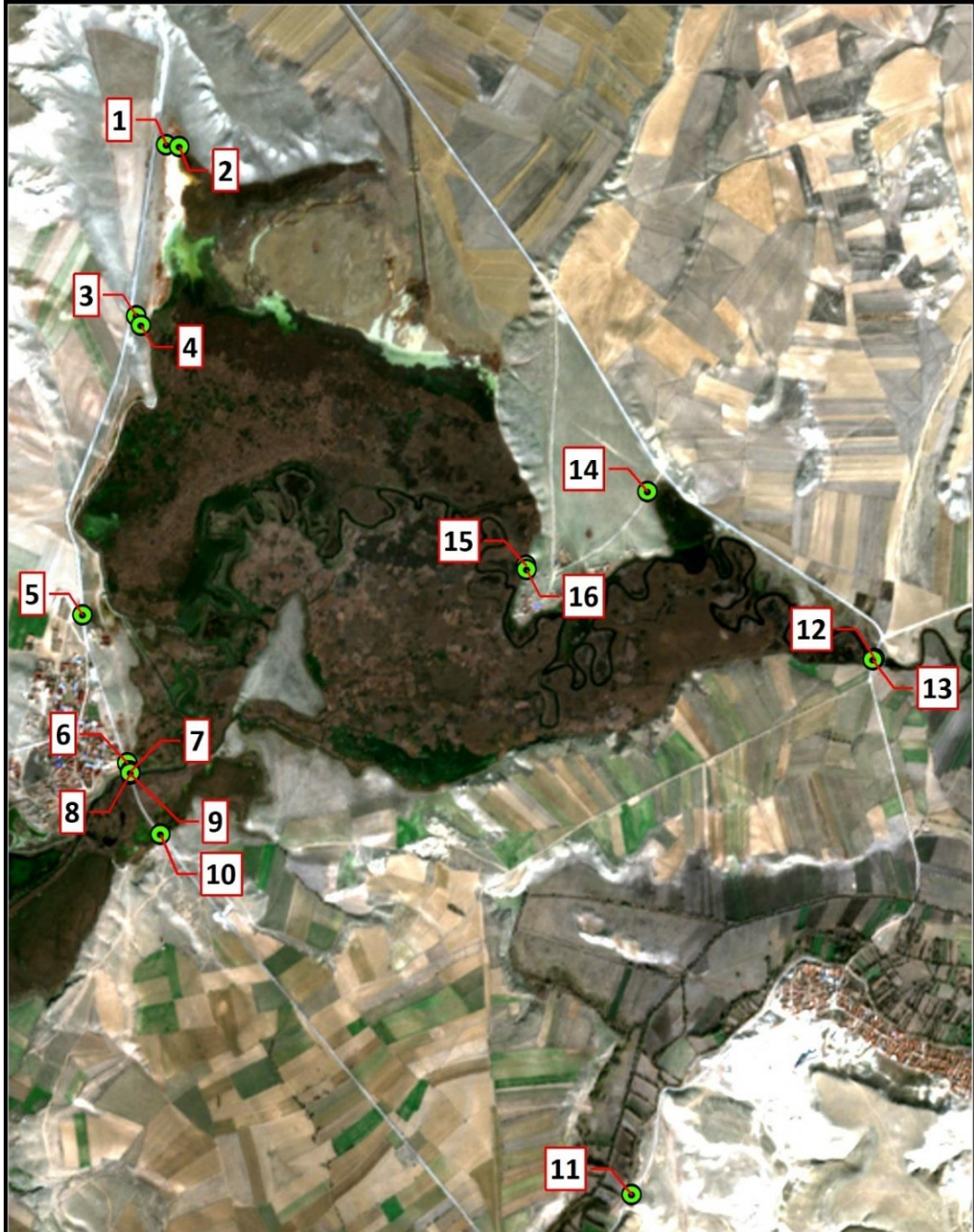


Figure A.1 Location of the photos taken on 19.12.2019 (date of base map is 03.12.2019)

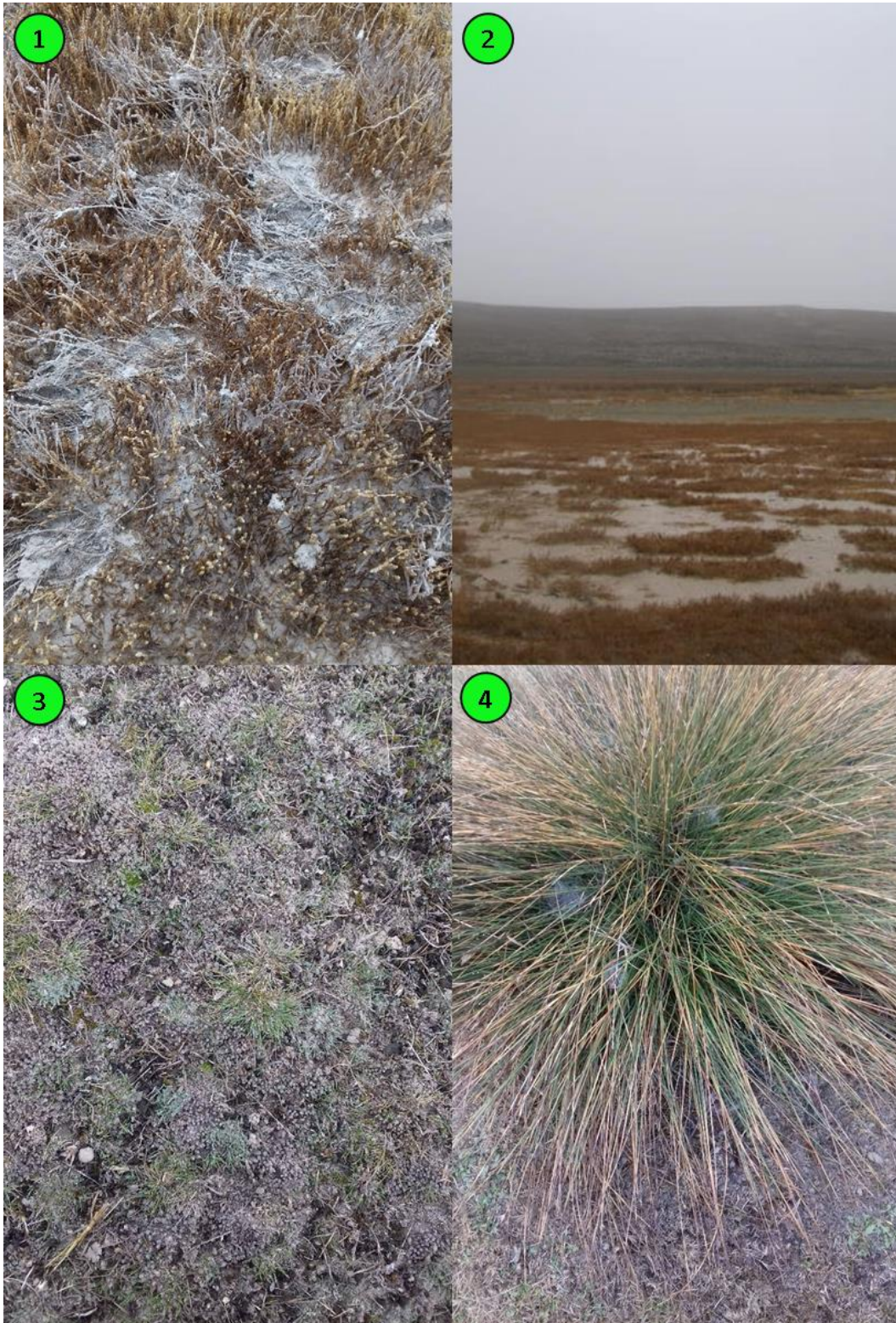


Figure A.2 ① Dry Salicornia on wet Gypsum ② General view of Gypsum area  
③ Pasture ④ Juncus



Figure A.3 (5) Tuft of Juncus (6), (7) Flood area (8) Submerged plants



Figure A.4 ⑨ Dense Typha ⑩ Trees ⑪ Limestone ⑫ East side of bridge located at easternmost boundary

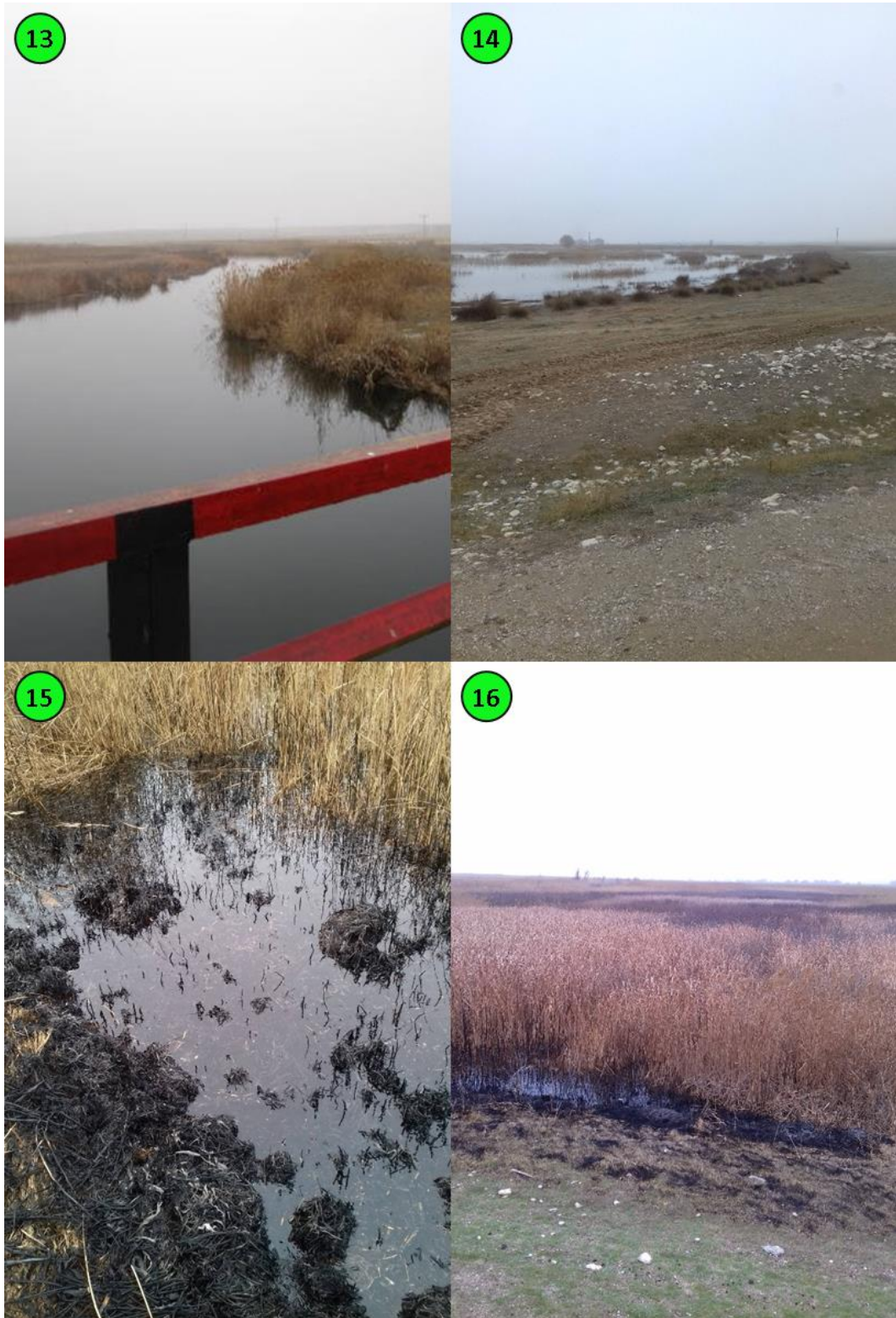


Figure A.5 (13) West side of bridge located at easternmost boundary (14) Tufts of Juncus (15), (16) Burned Typha

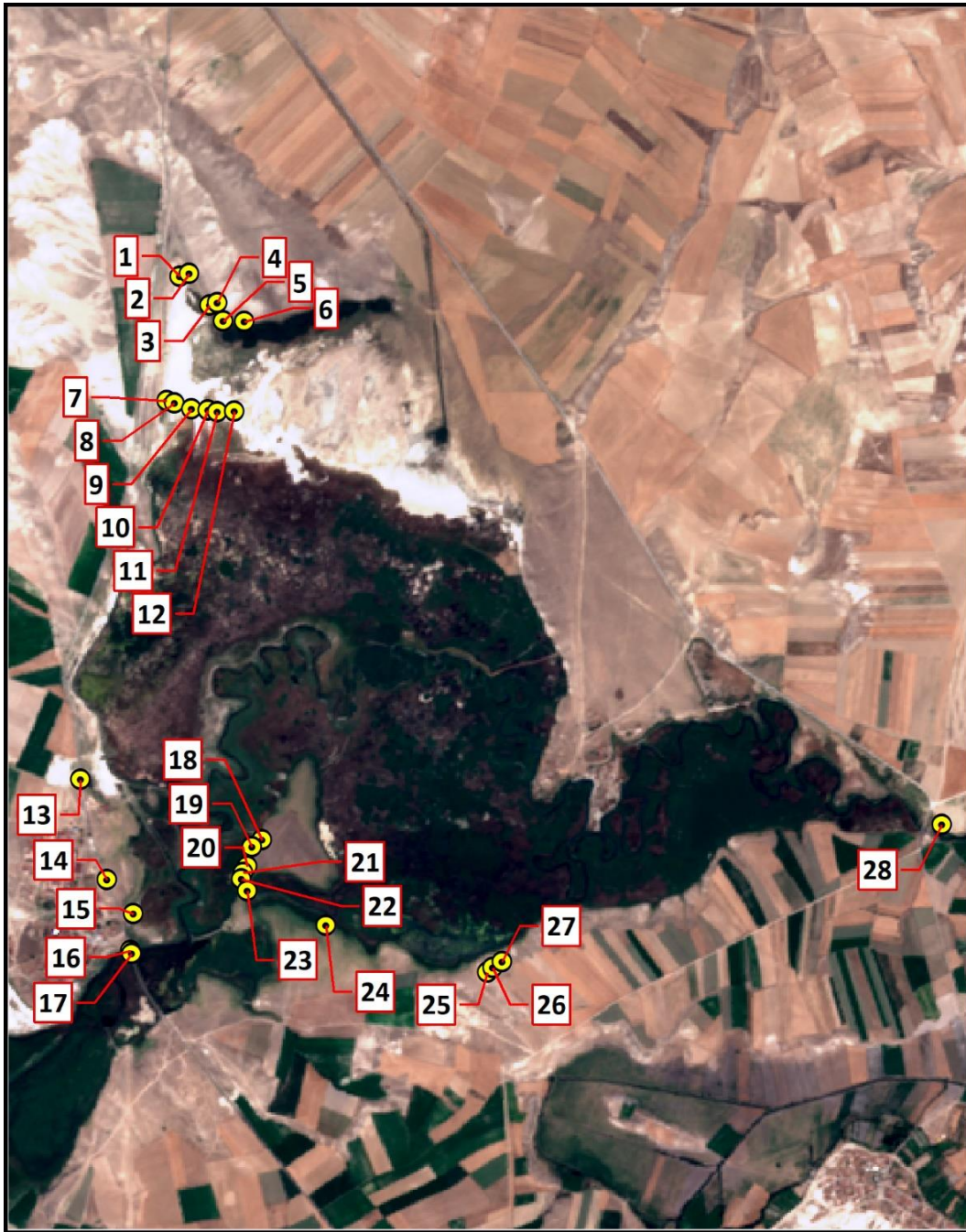


Figure A.6 Location of the photos taken on 19.08.2020 (date of base map is 19.08.2020)



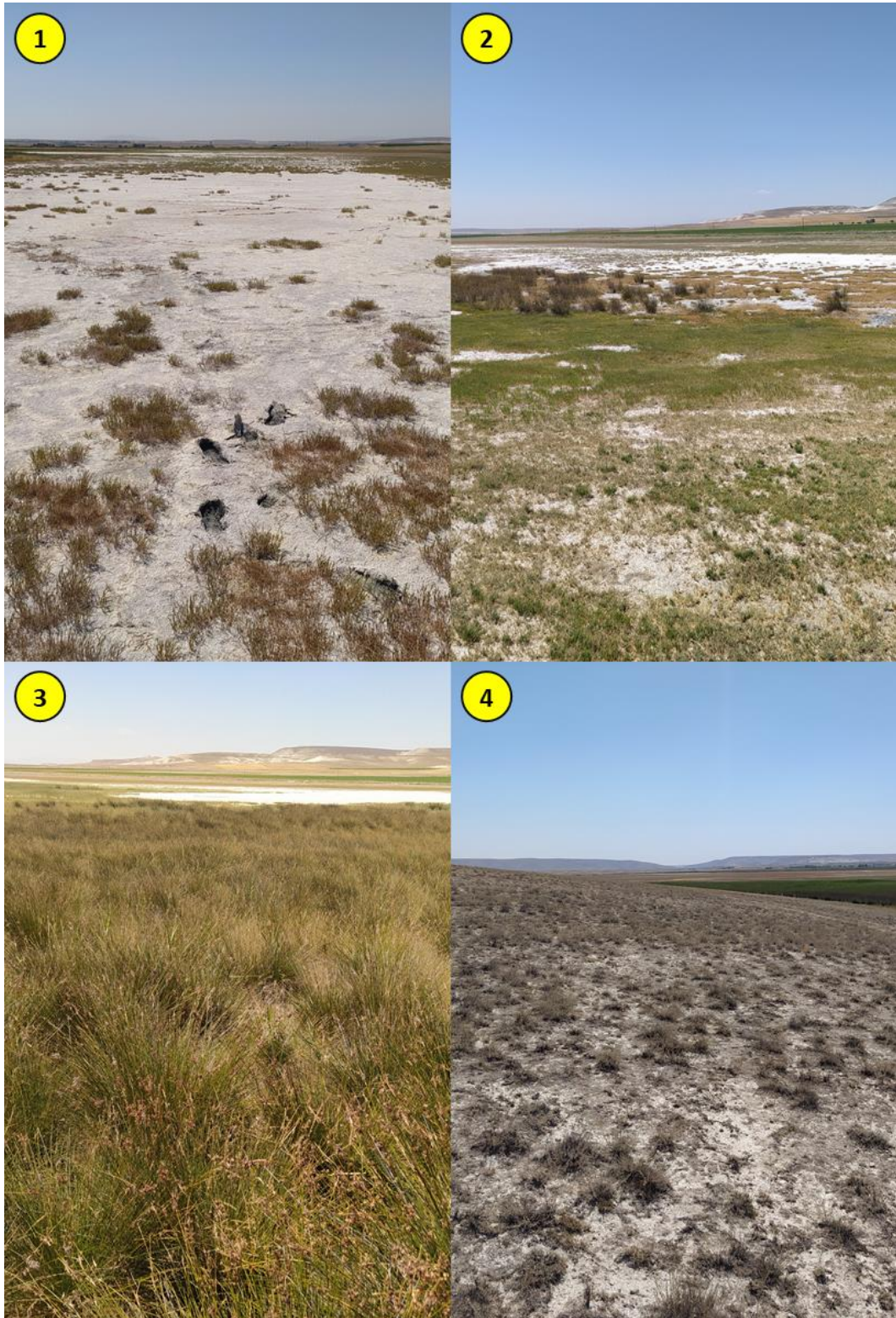


Figure A.7 ① Partial *Salicornia* on Gypsum ② Vegetated Gypsum ③ *Juncus*  
④ North side of wetland

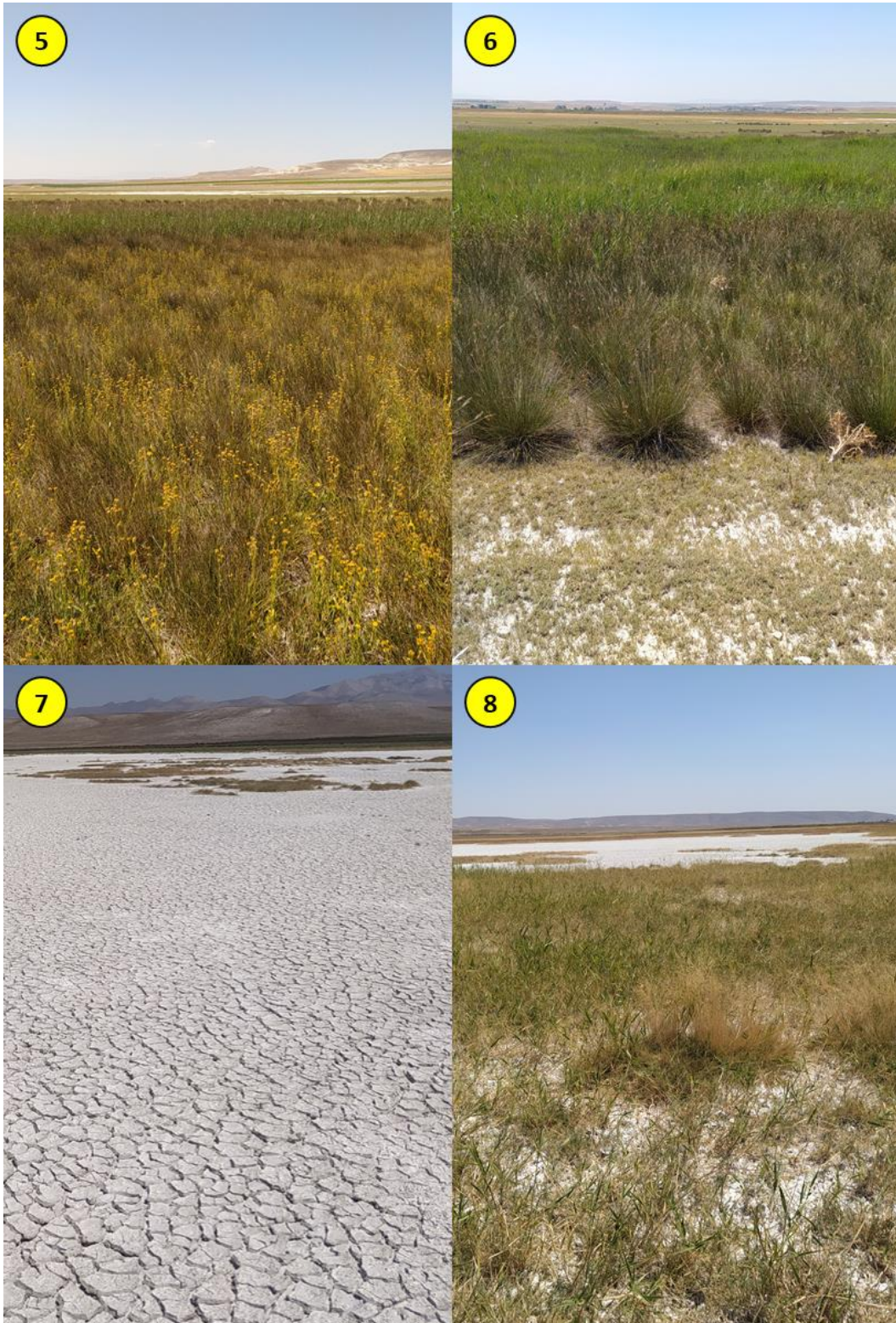


Figure A.8 ⑤ Juncus dominated mixed vegetation ⑥ Adjacent Pasture, Juncus and Phragmites clusters ⑦ Cracked Gypsum ⑧ Distichlis spicata on Gypsum

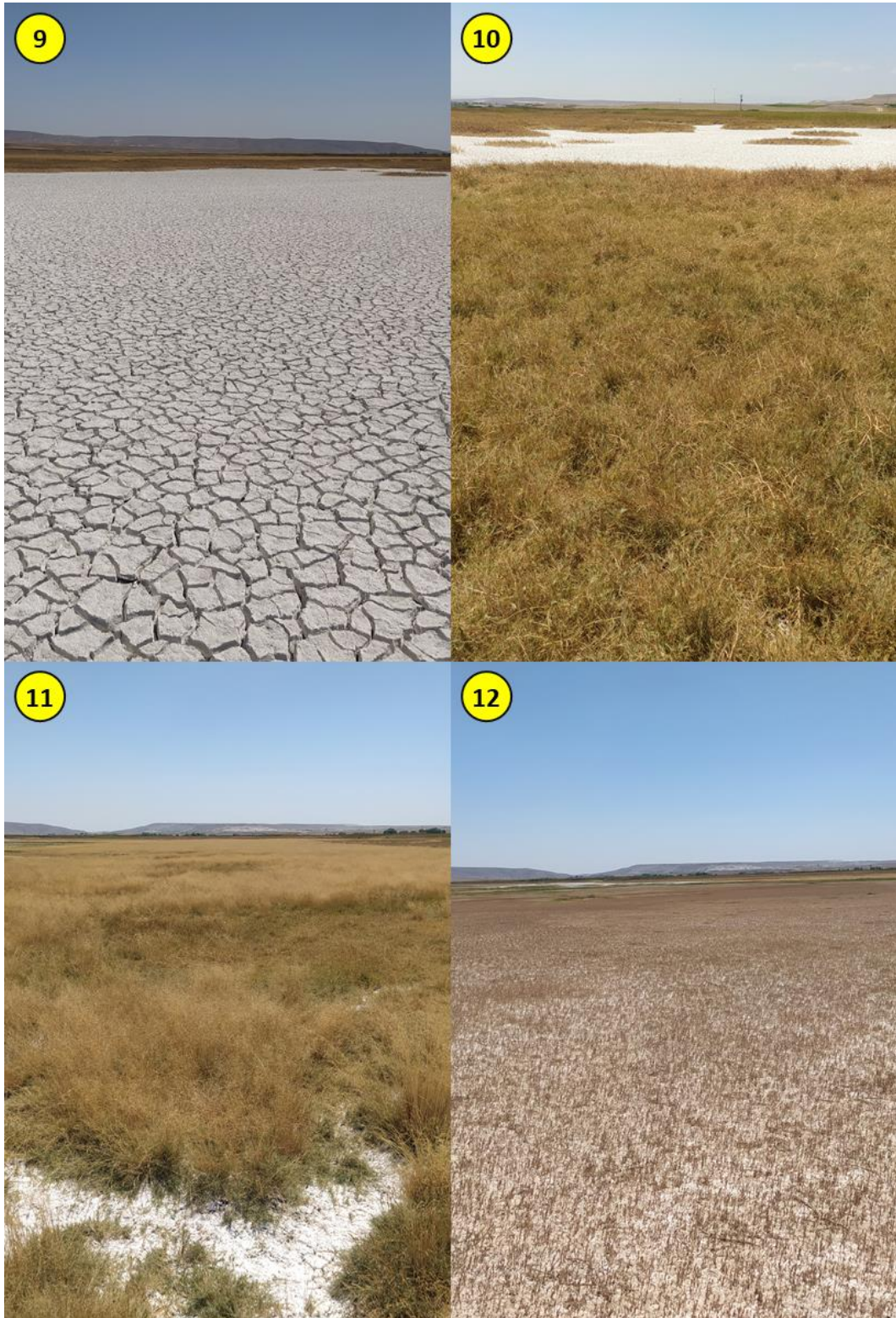


Figure A.9 ⑨ Cracked Gypsum ⑩, ⑪ *Distichlis spicata* ⑫ Dry *Salicornia* on Gypsum

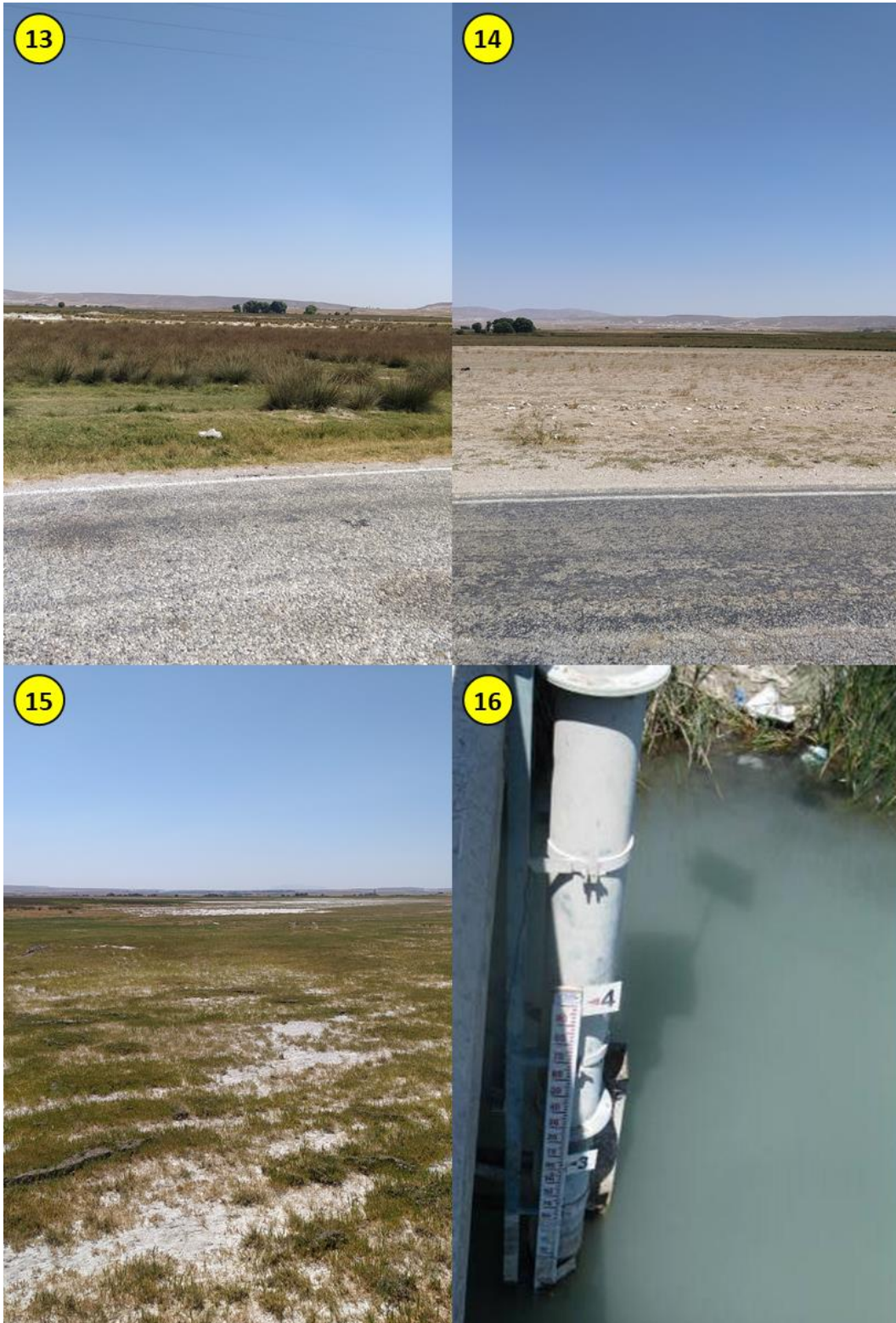


Figure A.10 ⑬ Juncus ⑭ Steppe ⑮ Vegetated Gypsum ⑯ Gauge plate on center bridge pillar



Figure A.11 ⑰ Dense Typha next to river ⑱ Pond inside dense Typha ⑲, ⑳ Pasture to Phragmites and Typha Transition

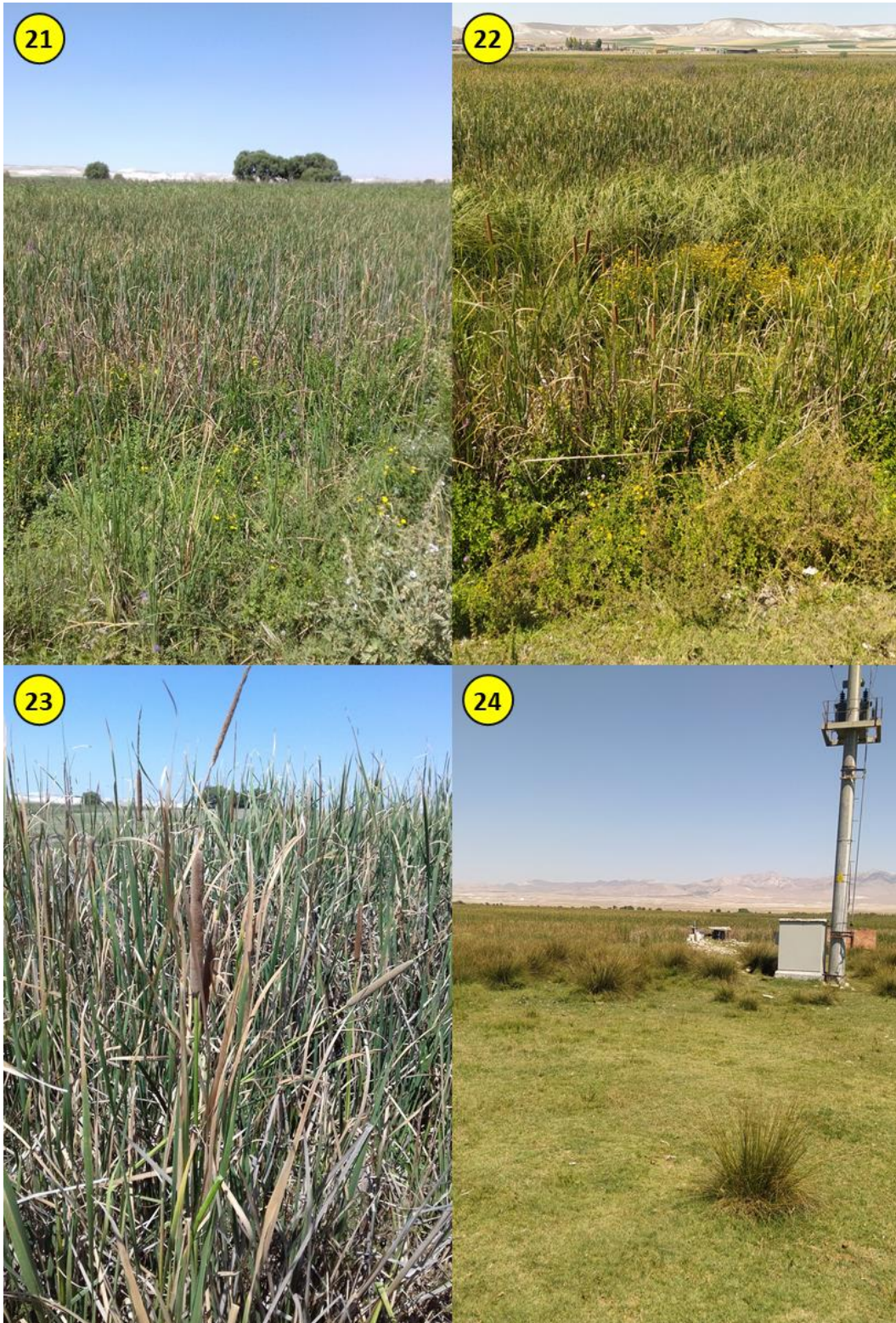


Figure A.12 (21), (22), (23) Typha and Phragmites dominated mixed vegetation (24) Tufts of Juncus

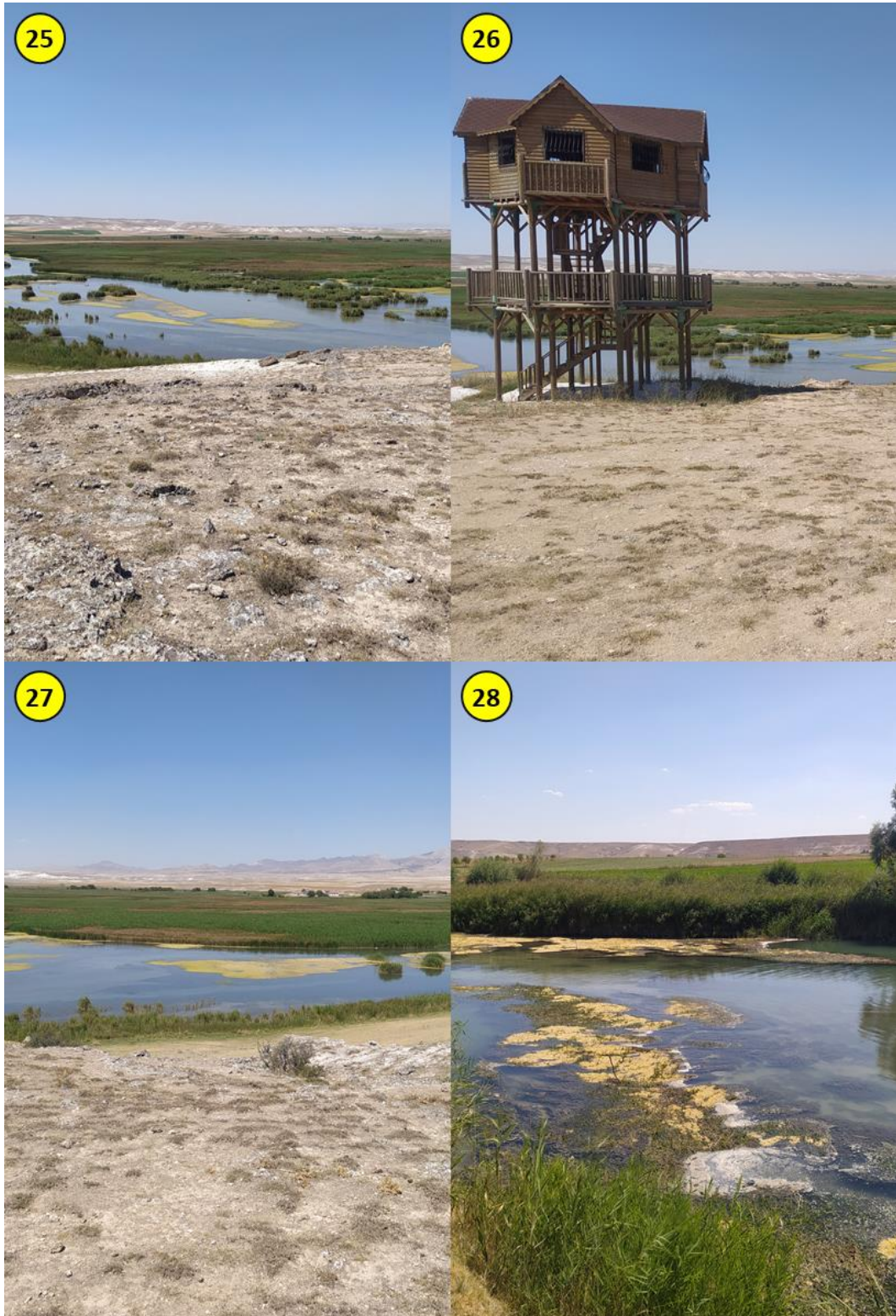


Figure A.13 ②⑤ Tufts of *Ranunculus* on river basin ②⑥ Bird watching tower ②⑦ Tufts of *Ranunculus* on river basin ②⑧ Tufts of *Ranunculus* on easternmost boundary



Figure A.14 Location of the photos taken on 02.09.2021 (date of base map is 08.09.2021)





Figure A.15 ① *Salicornia* on Gypsum ② Mud beneath Gypsum ③ *Juncus* and *Distichlis spicata* border ④ *Juncus* and *Phragmites* mixture



Figure A.16 ⑤ Gauge plate on center bridge pillar ⑥ Phragmites and Ranunculus  
⑦ Phragmites dominated mixed vegetation ⑧ Pond inside Phragmites and Typha



Figure A.17 ⑨ Steppe ⑩ Pasture ⑪ Pasture and Juncus transition ⑫ Tufts of Ranunculus on easternmost boundary

## B. Analysis Results for Samples Taken from Balıkdamı Wetland

Table B.1 Evaluation of soil sample-1


Sample Identity	Sample Photo			Sample Coordinates (Lat/Lon)	
Gypsum (surface)				39° 13' 25.91" N 31° 37' 25.33" E	
Parameters	Methods	Result	Unit	Evaluation	References
Power of Hydrogen (Electrometric)	ISO 10390	8.82	-	Strong alkali	TOVEP, 1991; Eyüpoğlu, 1999
Electrical Conductivity (Electrometric)	Internal method (Anonymous, 2009)	29.50	dS/m	Very salty	USDA, 1954 Agriculture Handbook No:60 Saline and Alkaline Soils
Lime (Calcimetric)	Internal method (Calcimetric method / Çağlar, 1949; Tüzüner, 1990)	9.05	%	Limy	Kacar, 2012
Organic Matter (Titrimetric)	Internal method (Walkley-Black, 1934)	2.91	%	Medium	TOVEP, 1991
Texture	Bouyoucos	Sand: - Silt: - Clay: -	%	No results	Bouyoucos, 1951; Millar and Turk, 1954
	Manual determination	-	-	Silty loam	Millar and Turk, 1954

Table B.2 Evaluation of soil sample-2



Sample Identity	Sample Photo			Sample Coordinates (Lat/Lon)	
Gypsum (underlayer)				39° 13' 25.91" N 31° 37' 25.33" E	
Parameters	Methods	Result	Unit	Evaluation	References
Power of Hydrogen (Electrometric)	ISO 10390	8.64	-	Strong alkali	TOVEP, 1991; Eyüpoğlu, 1999
Electrical Conductivity (Electrometric)	Internal method (Anonymous, 2009)	16.70	dS/m	Very salty	USDA, 1954 Agriculture Handbook No:60 Saline and Alkaline Soils
Lime (Calcimetric)	Internal method (Calcimetric method / Çağlar, 1949; Tüzüner, 1990)	41.51	%	Very limy	Kacar, 2012
Organic Matter (Titrimetric)	Internal method (Walkley-Black, 1934)	4.40	%	High	TOVEP, 1991
Texture	Bouyoucos	Sand: - Silt: - Clay: -	%	No results	Bouyoucos, 1951; Millar and Turk, 1954
	Manual determination	-	-	Clay	Millar and Turk, 1954

Table B.3 Evaluation of soil sample-3

Sample Identity	Sample Photo	Sample Coordinates (Lat/Lon)			
Steppe		39° 11' 54.79" N 31° 37' 41.36" E			
Parameters	Methods	Result	Unit	Evaluation	References
Power of Hydrogen (Electrometric)	ISO 10390	8.40	-	Weak alkali	TOVEP, 1991; Eyüpoğlu, 1999
Electrical Conductivity (Electrometric)	Internal method (Anonymous, 2009)	0.38	dS/m	Not salty	USDA, 1954 Agriculture Handbook No:60 Saline and Alkaline Soils
Lime (Calcimetric)	Internal method (Calcimetric method / Çağlar, 1949; Tüzüner, 1990)	24.22	%	Very limy	Kacar, 2012
Organic Matter (Titrimetric)	Internal method (Walkley-Black, 1934)	9.48	%	High	TOVEP, 1991
Texture	Bouyoucos	Sand: - Silt: - Clay: -	%	No results	Bouyoucos, 1951; Millar and Turk, 1954
	Manual determination	-	-	Silty clay loam	Millar and Turk, 1954

## C. Stream Gauge Observations for 2015 Water Year

12. Sakarya Havzası												
E12A024 SAKARYA N. AKTAŞ												
YERİ	: ESKİŞEHİR İLİ ÇİFTELER İLÇESİNİN 25 KM. GÜNEYDOĞUSUNDA AKTAŞ KÖYÜ YAKININDADIR (PAFTA J26-B4) 31° 20' 11" Doğu - 39° 19' 18" Kuzey											
YAĞIŞ ALANI	: 4342,20 km <sup>2</sup>						YAKLAŞIK KOT : 837 m					
GÖZLEM SÜRESİ	: 01.10.1952 - 30.09.2015											
ORTALAMA AKIMLAR	: Gözlem süresinde 6.785 m <sup>3</sup> /sn. (51 Yıllık ) 2015 Su yılında 6.415 m <sup>3</sup> /sn.											
ANLIK EN ÇOK VE EN AZ AKIMLAR:	2015 Su yılında anlık ençok akım : 16.700 m <sup>3</sup> /sn 05.07.2015											
	2015 Su yılında anlık enaz akım : 1.230 m <sup>3</sup> /sn 11.10.2014											
	Gözlem süresinde anlık ençok akım : 81.700 m <sup>3</sup> /sn 19.04.1984											
	Gözlem süresinde anlık enaz akım : 0.247 m <sup>3</sup> /sn 13.07.2014											
10. Anahtar Eğrisi (Seviyeler cm olarak)												
	Seviye	Akım	Seviye	Akım	Seviye	Akım	Seviye	Akım	Seviye	Akım	Seviye	Akım
	65	0.270	140	14.7	240	45.5	310	70.3				
	75	0.940	160	20.4	260	52.4	320	74.0				
	85	2.1	180	26.4	280	59.4	330	77.8				
	100	4.7	200	32.4	290	63.0	340	81.6				
	120	9.4	220	38.7	300	66.6	350	85.4				
Akımlar 01 Ekim 2014 'den 30 Eylül 2015' a kadar m <sup>3</sup> /sn olarak												
Gün	Ekim	Kasım	Aralık	Ocak	Şubat	Mart	Nisan	Mayıs	Haziran	Temmuz	Ağustos	Eylül
01	5.62	7.48	5.16	5.16	5.62	13.4	12.3	5.16	5.16	15.5	1.68	4.51
02	5.62	7.00	5.62	5.16	5.62	13.6	12.5	5.16	5.16	16.1	1.96	4.33
03	5.62	6.54	5.62	5.16	5.62	13.6	12.5	4.93	5.16	16.4	1.96	4.33
04	5.62	5.85	5.85	5.16	5.39	13.1	12.5	4.93	7.24	16.4	1.68	4.14
05	5.62	5.39	5.85	5.39	5.16	12.8	12.0	4.70	8.20	16.4	1.81	4.14
06	5.62	5.39	5.62	5.39	5.16	12.5	11.7	4.70	8.44	13.6	1.68	4.14
07	5.16	4.93	5.62	5.39	5.16	12.3	11.5	4.51	8.68	10.4	1.81	4.14
08	4.93	4.70	5.62	5.16	5.16	11.7	10.7	5.39	8.68	7.00	1.81	4.33
09	3.96	4.70	5.62	5.16	4.93	11.2	9.16	5.62	8.20	6.31	2.22	4.14
10	2.06	4.70	5.62	5.16	6.08	11.0	10.2	5.39	8.44	5.85	2.53	3.58
11	1.23	4.93	5.62	5.16	8.44	11.0	12.0	5.39	7.96	5.16	3.40	3.03
12	1.23	4.93	4.93	5.16	9.16	11.0	13.1	5.62	8.20	4.33	3.58	2.84
13	1.23	4.93	4.93	5.39	9.66	11.0	13.4	5.85	8.92	3.58	3.40	2.84
14	2.37	4.51	4.93	5.39	9.92	11.0	14.2	5.16	8.68	3.40	3.77	2.84
15	3.77	4.33	4.93	5.39	11.0	11.2	14.2	4.70	8.44	3.03	4.14	3.21
16	3.96	4.33	4.93	5.39	11.2	11.0	12.8	4.14	7.00	2.84	4.33	3.03
17	3.96	4.33	5.16	5.39	11.5	10.2	12.5	3.40	5.16	3.21	4.70	3.03
18	3.96	5.16	5.39	5.39	11.2	9.92	12.5	3.03	5.39	3.21	5.16	3.03
19	3.96	6.54	5.39	5.39	11.2	9.40	15.3	2.68	6.54	2.84	7.24	3.96
20	3.96	7.24	5.16	5.39	11.2	9.16	15.0	2.68	7.48	2.53	7.00	4.51
21	3.96	6.54	5.16	5.16	11.0	8.92	14.4	2.68	10.7	2.53	4.51	4.51
22	3.96	5.85	5.16	5.16	11.0	9.16	13.1	2.84	10.7	2.22	3.77	4.70
23	3.96	5.85	5.16	5.16	9.92	8.92	12.3	2.68	9.40	1.93	3.77	4.93
24	4.33	5.85	5.16	5.39	9.66	8.68	11.2	2.37	9.40	1.81	3.77	7.00
25	7.72	5.62	5.16	5.39	10.2	8.44	9.92	2.37	8.68	1.93	3.58	7.24
26	7.24	5.39	5.16	5.39	10.7	8.44	4.93	2.53	8.44	1.93	3.58	6.77
27	7.00	5.39	5.16	5.39	11.2	8.20	4.33	3.03	9.16	1.81	3.58	6.54
28	7.24	5.39	5.16	5.39	13.1	8.92	4.14	3.58	9.40	1.93	3.58	6.08
29	7.48	5.62	5.16	5.62	-----	9.16	5.16	3.77	9.16	1.68	3.58	4.33
30	7.24	5.62	5.16	5.85	-----	9.92	5.16	4.14	12.8	1.56	4.33	3.77
31	7.24	-----	5.16	5.62	-----	11.7	-----	4.70	-----	1.56	4.70	-----
Maks.	9.16	7.48	5.85	5.85	13.6	13.9	15.5	5.85	15.0	16.7	7.96	7.48
Min.	1.23	4.33	4.51	4.70	4.51	8.20	3.21	2.37	5.16	1.43	1.43	2.68
Ortalama	4.74	5.50	5.30	5.33	8.76	10.7	11.2	4.12	8.17	5.77	3.48	4.33
LfY/SN/Hm <sup>2</sup>	1.09	1.27	1.22	1.23	2.02	2.46	2.57	0.950	1.88	1.33	0.801	0.998
AKIM mm.	2.92	3.28	3.27	3.29	4.88	6.58	6.66	2.54	4.87	3.56	2.15	2.59
MİL. M3	12.7	14.3	14.2	14.3	21.2	28.6	28.9	11.0	21.2	15.5	9.31	11.2
SU YILI ( 2015 ) YILLIK TOPLAM AKIM 202.41 MİLYON M3 47 MM. 1.5 LFY/SN/Hm <sup>2</sup>												

Figure C.1 Flow data of Sakarya N. Aktaş Station (General Directorate of State Hydraulic Works, 2018)





## CURRICULUM VITAE

Surname, Name: Özer, Erdem

### EDUCATION

<b>Degree</b>	<b>Institution</b>	<b>Year of Graduation</b>
MS	University of Nottingham Institute of Engineering Surveying and Space Geodesy	2009
BS	Istanbul Technical University Department of Geodesy and Photogrammetry Engineering	2007
High School	Antalya Anatolian High School	2002

### FOREIGN LANGUAGES

English, German